ICFO – THE INSTITUTE OF PHOTONICS SCIENCES
&
UPC – UNIVERSITAT POLITÈCNICA DE CATALUNYA

Nanoscale Spatial Control of Light in Optical Antennas

Giorgio Volpe

Advisor: Dr. Romain Quidant
PhD Thesis – 2012

To Anna, Giovanni and Jenny

Abstract

The dynamic and deterministic control of light over space and time on the subwavelength scale is a key requirement in order to extend concepts and functionalities of macro-optics down to the nanometer scale. An increased level of control will also have fundamental implications in our understanding of nanoscale phenomena. One of the main problems nano-optics is aiming to tackle, therefore, is how and how well we can dynamically control the spatial distribution of light on such a length scale. Unfortunately, a fundamental limit of physics – the limit of diffraction of light – hampers our ability to selectively optically address nanoscale features separated by less than half the wavelength of light.

The field of *plasmonics* offers a unique opportunity for bridging the gap between the limit of diffraction and the nanometer scale. Plasmonic metallic nanoantennas can efficiently couple to propagating light and concentrate it into nanometer volumes, and vice versa. Additionally, these nanoantennas hold promise for enhancing the efficiency, to name but a few, of photodetection, light emission, sensing, heat transfer, and spectroscopy on the nanometer scale.

Learning how to accurately control the optical response of these nanoantennas represents a very promising approach to the control of the distribution of light fields over space and time on the nanometer scale. Traditionally, two main complementary approaches have been followed in order to control the optical response of plasmonic nanoantennas: the first, *static approach* aims at optimizing the design of the nanoantenna as a function of its specific application, while the second, *dynamic approach* aims at reversibly tuning the optical near-field response of a given nanostructure by engineering its excitation light over time and space.

The work reported in this Thesis expands on the state of the art of these two approaches, and develops new tools, both experimental and theoretical, to extend the level of control we have over the spatial distribution of light on the subwavelength scale.

After presenting an overview of the basic principle of nano-optics and surface plasmon optics, **Chapter 1** reviews the advances in the control of the optical response of metal nanostructures – either by a static or a dynamic approach – at the time this research work was initiated.

Tailoring the shape and the dimensions of metal nanoparticles is still a fundamental ingredient in order to tune plasmonic resonances and to control light fields on the nanoscale. As novel examples of static control, therefore, **Chapters 2 and 3** study new designs of plasmonic nanostructures with previously unexplored capabilities of molding light field on the nanoscale, such as a fractal design and a unidirectional Yagi-Uda nanoantenna.

Chapters 4 and 5 describe a new theoretical and experimental tool for the dynamic and deterministic control of the optical response of nanoantennas based on a spatial phase shaping of the excitation light: the optical near-field distribution resulting from the interaction between light and plasmonic nanostructures is typically determined by the geometry of the metal system and the properties of the incident light, such as its wavelength and its polarization; nonetheless, the accurate and dynamic control of the optical near field at the subwavelength scale – independently of the geometry of the

nanostructure -- is also an important ingredient for the development of future nano-optical devices and to extend concepts and functionalities of macroscopic optics down to the nanometer scale.

Finally, the **Conclusion** summarizes the results of this work and gives an overview of some parallel studies to this thesis. Some of the final remarks afford a glimpse into future perspectives and strategies to complement static and dynamic approaches in one powerful tool, which would enormously advance our ability to control the optical response of nanoantennas in space and time on a subdiffraction scale.

Resumen

El control dinámico y determinístico de la luz en una escala espacial por debajo de la longitud de onda es un requisito clave para ampliar los conceptos y las funcionalidades de óptica de la macro-óptica hasta la escala nanométrica. Un mayor nivel de control también tendrá implicaciones importantes en nuestra comprensión de los fenómenos ópticos en la nanoescala. Uno de los principales problemas en nano-óptica tiene como objetivo describir cómo y con qué precisión es posible controlar la distribución espacial de la luz de forma dinámica en la nanoescala. Desafortunadamente, un límite fundamental de la física – el límite de difracción de la luz – afecta nuestra capacidad de seleccionar ópticamente puntos separados por menos de media longitud de onda de la luz.

El campo de la *plasmónica* ofrece una oportunidad única para cerrar la brecha entre el límite de difracción y la escala nanométrica. Nanoantenas metálicas pueden acoplarse eficientemente a luz propagante y focalizarla en volúmenes nanométricos, y viceversa. Además, estas nanoantenas prometen mejorar significativamente la eficiencia de procesos como le fotodetección, la emisión de luz, sensores, transferencia de calor, y espectroscopía a la escala nanométrica.

Aprender a controlar de forma precisa la respuesta óptica de estas nanoantenas representa un enfoque muy prometedor para controlar la distribución espacial y temporal de la luz a la escala nanométrica. Tradicionalmente, se han desarrollado dos principales estrategias para el control de la respuesta óptica de nanoantenas plasmónicas: la primer estrategia (*estrategia estática*) tiene como objetivo la optimización del diseño geométrico de las nanoantenas acorde a su aplicación, mientras que la segunda estrategia (*estrategia dinámica*) tiene como objetivo la modulación reversible del campo cercano de una nanoestructura dada a través de la manipulación de la luz de excitación en el tiempo y el espacio.

El trabajo presentado en esta Tesis extiende el estado del arte de estas dos estrategias, y desarrolla nuevas herramientas, tanto experimentales como teóricas, para ampliar el nivel de control que tenemos sobre la distribución espacial de la luz debajo del límite de difracción.

Después de presentar una visión general de los principios básicos de nano-óptica y de la óptica de lo plasmones de superficie, el **Capítulo 1** repasa los avances en el control de la respuesta óptica de nanoestructuras metálicas – sea por una estrategia estática o dinámica – en el momento en que se inició este trabajo de investigación.

La modificación de la geometría y las dimensiones de las nanpartículas metálicas sigue siendo un ingrediente fundamental para controlar las resonancias plasmónicas y los campos de luz a la escala nanométrica. Como ejemplos novedosos de control estático, por lo tanto, los **Capítulos 2 y 3** estudian nuevos diseños de estructuras plasmónicas con capacidades sin precedentes de modelar campos de luz a la escala nanométrica, en particular un diseño fractal y una nanoantena unidireccional tipo Yagi-Uda.

Los **Capítuols 4 y 5** describen una nueva herramienta teórica y experimental para el control dinámico y determinístico de la respuesta óptica de nanoantenas basada en la modulación espacial de la fase de la luz de excitación: el campo óptico cercano, que resulta de la interacción entre la luz y las nanoestructuras plasmónicas, es normalmente

determinado por la geometría del sistema metálico y las propiedades de la luz incidente, como su longitud de onda y su polarización; sin embargo, el control exacto y dinámico del campo óptico cercano debajo de límite de difracción de la luz – independientemente de la geometría de la nanoestructura – es también un ingrediente importante para el desarrollo de futuros dispositivos nano-ópticos y para ampliar los conceptos y las funcionalidades de la óptica macroscópica a la escala nanométrica.

Finalmente, la **Conclusión** resume los resultados de este trabajo y ofrece una visión general de algunos estudios paralelos a esta tesis. Algunas de las observaciones finales permiten echar un vistazo a las perspectivas y estrategias futuras para complementar el control estático y el control dinámico en una única herramienta, que podría avanzar enormemente nuestra capacidad de controlar la respuesta óptica de nanoantennas debajo del límite de difracción.

Acknowledgments

At times exciting and rewarding, at times challenging and frustrating, this Thesis is the culmination of my research, to which I have devoted the last four years, and that would have not been possible without the help, contribution and support of many people.

First on the list, I would like to thank Romain, my Thesis advisor, for being a source of inspiration throughout this period. Since the beginning, he has been very supportive and understanding of all my crazy ideas in and out of science. I am particularly thankful to him for guiding me through the good and bad moments of a PhD student's life, and for providing advice both in science and life matters.

I am really thankful to Lluis Torner, ICFO director: he has always been encouraging to me, and made all of my team's projects happen. He showed his support on more than one occasion. His advices, leadership and friendly attitude have always been an important driving motor behind all of our projects.

I am particularly grateful for all the guidance I received froom my "scientific mentors" over the Master's and PhD's years: Giovanni, Dmitri, Romain, Petru, Sudhir, Maria, Lukas, and Hayk. Not only have I learnt a lot from them, but they provided inspiration throughout my studies.

I would like to thank the people of my group for the good times inside and outside the laboratory, for the fruitful scientific discussion, and for all the knowledge they transferred to me: Petru, Sudhir, Maria, Mark, Srdjan, Jan R, Maurizio, Guillaume, Simó, Sukanya, Jan G, Mathieu, Jon, Michael, Maria Ale, Valeria, Esteban, Chris, Sebastian, Ignacio, Monika, Johann, and Tieh-Ming.

I also thank the people of my adoptive group in Rochester for making my American experience unique at a scientific and personal level, and really worthwhile: Lukas, Barbara, Hayk, Zack, Palash, Sergio, Brad, Ryan, Shawn, Aleks, and Anirban.

My scientific knowledge and perspective have been greatly enhanced by all the collaborations: Gabriel Molina-Terriza, Alberto G. Curto, Tim H. Taminiau, Niek F. van Hulst at ICFO; Lukas Novotny and Hayk Harutyunyan in Rochester; and my brother Giovanni, of course. Thanks to all the people of my group I had the chance to work with directly: Sudhir, Mark, Simó, Srdjan, Esteban, and Chris. I am particularly in debt to Roser and Monika. I regard myself very lucky for having had the pleasure and honor of working with them all.

I must also thank the Student Chapter in ICFO. In particular: Giovanni, Armand, Osamu, Xu, Manoj, Lars, Petru, Jan, Michael, Marina, Rafa and again our Student Advisors Valerio, Romain, Jens and Lluis.

Another big thank you goes to the manager of ICFO, Dolors, and the KTT director, Silvia, for all their support for our craziest ideas.

I wish to acknowledge the Scholarship from the Spanish Ministry of Science and Education that supported me for the last four years.

Finally, I wish to thank my real and adoptive family. Thank you to my brother Giovanni for so many things I do not even know where to start from. Thank you to my mother Anna and my father Giuseppe: together with my brother, they have provided support, love and care through out my life. Thank you to Andrea for being a caring and supportive friend, a wonderful flatmate, and for laughing at my jokes. Thank you to my

lovely Jenny: you cope with me and the bluest of my moods; you bring the sunshine in the blackest of my days; and you definitely bring magic to my scientist's life.

Castelldefels, 13 January 2012.

Contents

Introduction

In the 20th century, the advent of electronics marked the beginning of a new era in human science and technology: information technologies based on microelectronics, such as computers, the Internet and mobile phones, have deeply impacted the way we communicate, conduct business, and do science [Razavi (2008)].

The development of microelectronics has progressively increased the scientific interest for nanoscience and nanotechnology: nowadays, in fact, research in these fields, which was originally driven by the computer industry, is attracting increasing fundamental interest by itself. A great deal of attention is devoted to advancing the field of optics on the nanometer scale, or *nano-optics*, mainly because the energy of light lies in the range of the electronic and vibrational transitions in matter [Novotny & Hecht (2006)].

Controlling the distribution of light over space and time on the subwavelength scale has fundamental implications in our understanding of the physics underlying the nanoworld phenomena. Our increased level of control will be also useful, in terms of applications, in order to extend concepts and functionalities of macro-optics down to the nanometer scale. One of the main problems nano-optics is aiming to tackle, therefore, is how and how well we can dynamically control the spatial distribution of light on such a length scale. Unfortunately, a fundamental limit of physics – the limit of diffraction of light – hampers our ability to selectively optically address nanoscale features separated by less than half the wavelength of light.

The field of *plasmonics* offers a unique opportunity for bridging the gap between the limit of diffraction and the nanometer scale [Brongersma & Shalaev (2010); Schuller *et al*. (2010)]. Plasmonic metallic nanoantennas can efficiently couple to propagating light and concentrate it into nanometer volumes, and vice versa. Additionally, these nanoantennas hold promise for enhancing the efficiency, to name but a few, of photodetection, light emission, sensing, heat transfer, and spectroscopy on the nanometer scale [Novotny & van Hulst (2011)].

Learning how to accurately control the optical response of these nanoantennas, therefore, represents a very promising approach to the control of the distribution of light fields over space and time on the nanometer scale. Traditionally, two main complementary approaches have been followed in order to control the optical response of plasmonic nanoantennas: the first, *static approach* aims at optimizing the design of the nanoantenna as a function of its specific application, while the second, *dynamic approach* aims at reversibly tuning the optical near-field response of a given nanostructure by engineering its excitation light over time and space.

This thesis expands on the state of the art of these two approaches, and develops new devices and tools – both experimental and theoretical – that extend the level of control we have over the optical response of plasmonic nanoantennas.

After presenting an overview of the basic principle of nano-optics and surface plasmon optics, **Chapter 1** reviews the advances in the control of the optical response of metal nanostructures – either by a static or a dynamic approach – at the time this research work was initiated.

Tailoring the shape and the dimensions of metal nanoparticles is still a fundamental ingredient in order to tune plasmonic resonances and to control light fields on the nanoscale. As novel examples of static control, therefore, **Chapters 2 and 3** study new designs of plasmonic nanostructures with previously unexplored capabilities of molding light field on the nanoscale, such as a fractal design and a unidirectional Yagi-Uda nanoantenna.

Chapter 2 proposes the use of fractal nanostructures to extend the degrees of freedom and the parameters available for the design of plasmonic structures [Volpe *et al.* (2011)]. In particular, the focus is on a paradigmatic fractal geometry, namely the Sierpinski carpet, and on the possibility of using it to achieve a controlled broadband spectral response by controlling the degree of its fractal complexity. Furthermore, some other arising properties, such as subdiffraction focusing and its potential use for optical trapping of nano-objects, are investigated. An attractive advantage of the focusing over more standard geometries, such as gap antennas, is that it occurs away from the metal surface ($\approx 80\,nm$), leaving an open space accessible to objects for enhanced light-matter interactions.

Chapter 3 presents the design and fabrication of an optical Yagi-Uda antenna [Curto *et al.* (2010)]. In order to prove the unidirectional emission pattern of the antenna, a quantum dot is placed in its near-field to drive the resonant feed element of the antenna. The resulting quantum-dot luminescence is strongly polarized and highly directed into a narrow forward angular cone. The directionality of the quantum dot can be controlled by tuning the antenna dimensions. These results show the potential of optical antennas to communicate energy to, from, and between nano-emitters.

Chapters 4 and 5 describe a new theoretical and experimental tool for the dynamic and deterministic control of the optical response of nanoantennas based on a spatial phase shaping of the excitation light. The optical near-field distribution resulting from the interaction between light and plasmonic nanostructures is typically determined by the geometry of the metal system and the properties of the incident light, such as its wavelength and its polarization. Nonetheless, the accurate and dynamic control of the optical near field at the subwavelength scale – independently of the geometry of the nanostructure -- is also an important ingredient for the development of future nano-optical devices and to extend concepts and functionalities of macroscopic optics down to the nanometer scale.

As a first intuitive experimental verification of this idea, **Chapter 4** shows the possibility of reconfiguring the optical near-field distribution near plasmonic nanoantennas based on sub-wavelength spatial phase variations at the focus of high-order beams [Volpe *et al.* (2009)]. The first results show how the introduction of phase jumps in the incident field driving a gap nanoantenna strongly affects its near-field response. Moreover, the feasibility of exploiting this approach to selectively switch on and off hot spots within more complex antenna architectures is also demonstrated.

Chapter 5, in order to extend the previous intuitive demonstration to any plasmonic design, proposes a novel deterministic protocol, based on continuous light flow, which enables us to control the concentration of light in generic plasmonic nanostructures [Volpe *et al.* (2010)]. Based on an exact inversion of the response tensor of the

nanosystem, the so called Deterministic Optical Inversion Protocol (DOPTI) provides a physical solution for the incident field that leads to a desired near-field pattern, expressed in the form of a coherent superposition of high-order beams. The high degree of control achieved on complex plasmonic architectures is demonstrated and the protocol's efficiency and accuracy is also quantified.

The **Conclusion** summarizes the results of this work and gives an overview of some parallel studies to this thesis. Some of the final remarks afford a glimpse into future perspectives and strategies to complement static and dynamic approaches in one powerful tool, which would enormously advance our ability to control the optical response of nanoantennas in space and time on a subdiffraction scale.

Chapter 1

Plasmonics: Controlling Light on the Nanoscale

The dynamic control of the spatial distribution of light at subwavelength scales is important in order to extend concepts and functionalities of macro-optics down to the nanometer scale. A priori, optical control on this length scale goes against the law of diffraction of light, which prevents us from independently optically addressing two points separated by a distance shorter than roughly half the wavelength of light.

Fortunately, the optical properties of some materials allow us to overcome this fundamental limit: plasmonic metallic nanoantennas, for example, can efficiently couple to propagating light and concentrate it into nanometer volumes. Learning how to accurately control the optical response of these nanoantennas, therefore, represents a very promising approach to the dynamic control of the spatial distribution of light fields on the nanometer scale.

After giving an overview of the basic principles of nano-optics and Surface Plasmon optics, this chapter presents a review of the state of the art in the two main approaches – *static* and *dynamic* – that can be adopted to tune the optical response of similar nano-systems.

1.1 Nano-Optics: Extending Optics to the Nanoscale

In the last twenty years, the need for ever smaller and faster devices have made miniaturization and integration two of the fundamental paradigms in electronics, and considerably increased the fundamental interest in nanoscience and nanotechnology, thus setting the basis for some of the new technological and scientific trends of the 21st century. Laser technology, electron microscopy, and nanofabrication facilities, to name but a few, have enhanced our ability to fabricate, measure and manipulate matter on the nanoscale or below, down to the level of a single atom [Novotny & Hecht (2006)]. As we move towards smaller and smaller length scales, new physical effects, such as quantum effects, become prominent and pave the way for a whole new range of future technological applications that may well complement, or even replace, standard technologies, such as microelectronics [Scarani & Thew (2006)].

In this general trend towards nanoscience and nanotechnology, great effort is devoted to advancing the field of optics on the nanometer scale, or *nano-optics*, mainly because the energy of light lies in the range of the electronic and vibrational transitions in matter. Therefore, the interaction between light and matter offers a unique possibility not only to extract information about the structural and dynamical properties of matter [Moerner & Kador (1989); Chen *et al.* (2010)], but also to control and manipulate the aforementioned properties, for example, for the implementation of optical circuits [Almeida *et al.* (2004)] and sensors [Kreuzer *et al.* (2006)], as well as for applications in data storage [Zijlstra *et al.* (2009)], optical trapping [Juan *et al.* (2011)] and super-resolution microscopy [Hell (2007)]. Moreover, the implementation of photonic devices at the nanoscale could offer a faster alternative to electronics both in terms of computation and communication speed (Figure 1.1 (b)).

In order to be beneficial for these and many other applications and to extend concepts and functionalities of macro-optics down to the nanoscale, current nano-optics is facing one of its main challenges: how and how well can we control the distribution of light over space and time on this length scale?

1.1.1 The limit of diffraction of light

Traditionally, our ability to selectively optically address nanoscale features has been limited by a fundamental law of physics – namely the limit of diffraction – that prevents us from focusing propagating light to dimensions smaller than roughly half its wavelength, typically a few hundred nanometers at visible frequencies. In a typical nano-optical problem (Figure 1.1 (a)), the area of interest in which we would like to control light is typically much smaller than this size.

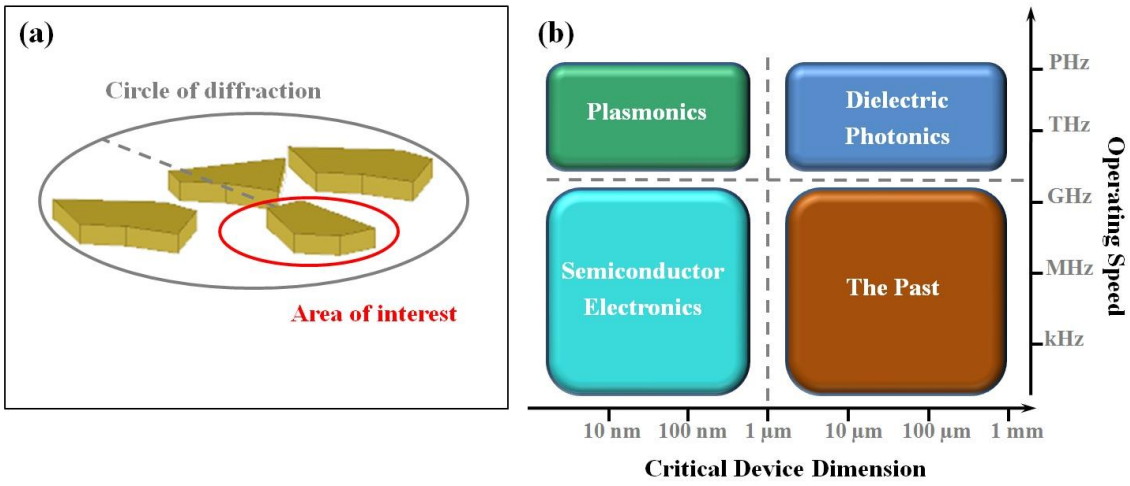

Figure 1.1: Plasmonics: overcoming the limit of diffraction. (a) *In a typical nano-optical system, the area of interest (red circle) is much smaller than the wavelength of light. Unfortunately, the limit of diffraction has hampered our ability to selectively optically address nanoscale features to roughly half the wavelength of light (grey circle);* (b) *plasmonic structures can serve as a bridge between photonics and nanoelectronics by focusing light to subwavelength volumes. The different domains in terms of operating speed and device sizes rely on the unique material properties of semiconductors (electronics), insulators (photonics), and metals (plasmonics). The dashed lines indicate physical limitations of different technologies: semiconductor electronics is limited in speed by heat generation and interconnect delay time issues to about 10 GHz; dielectric photonics is limited in size by the fundamental laws of diffraction. Figure adapted from [Brongersma & Shalaev (2010)].*

Generally speaking, the reason behind this fundamental limit can be understood in terms of Fourier mathematics [Novotny & Hecht (2006)]: Fourier considerations lead, in fact, to an expression that connects the minimum distinguishable separation distance Δx between two point sources to the bandwidth of the spatial frequencies Δk_x that can

be collected by the optical system along the same spatial direction. The resulting expression reads as:

$$\Delta x \geq \frac{1}{\Delta k_x}. \tag{1.1}$$

According to Equation (1.1), the minimum separation distance along one direction x is, therefore, inversely proportional to the spread in the magnitude of the wave vector components in the respective spatial direction: in far-field optics, where the spatial frequencies associated with evanescent wave components can be discarded, the maximum possible value for Δk_x is given by the total length of the free-space wave vector

$$k = \sqrt{k_x^2 + k_y^2 + k_z^2} = \frac{2\pi}{\lambda}. \tag{1.2}$$

This leads to the final expression

$$\Delta x \geq \frac{\lambda}{2\pi}, \tag{1.3}$$

which then sets a lower limit for Δx [Vigoureux & Courjon (1992); Novotny & Hecht (2006)]. In a real system, however, this expression must be corrected by the numerical aperture NA of the focusing lens, which accounts for the limited collection cone and the refractive index of the medium.

The figure set by Equation (1.3) is a best case scenario. According to the Rayleigh criterion instead, the radius of the smallest spot, to which a collimated beam of light can be focused, is given by [Born & Wolf (2002); Hell (2007)]

$$\Delta x \approx 0.61 \frac{\lambda}{NA}, \tag{1.4}$$

which also gives the distance between two object points that can just be resolved, and therefore addressed independently. This limit is approximately a factor 2 worse than the criterion of Equation (1.3). For a high-resolution immersion oil lens ($NA = 1.45$), this value is, for example, about $170\,nm$ for the shortest wavelength of visible light ($\lambda \approx 400\,nm$).

1.1.2 Beyond the limit of diffraction

Fortunately, it is still possible to increase the spatial confinement of light along one component of the wave vector beyond the limit of Equation (1.3) at the expense of the other components that become purely imaginary. In fact, from Equation (1.2) and (1.3),

$\Delta x < \frac{\lambda}{2\pi}$ implies that $k_x^2 > \frac{2\pi}{\lambda}$, and, therefore, to satisfy Equation (1.3), k_y^2 and k_z^2 must be negative that is, k_y and k_z, being purely imaginary, and thus associated to evanescent fields [Novotny & Hecht 2006]. In this case then, the Rayleigh limit for the confinement of light no longer holds, and in principle infinite confinement of light becomes, at least theoretically, possible. For example, the utilization of photonic crystals [Noda *et al.* (2000)] or left-handed metamaterials [Pendry (2000); Fang *et al.* (2005)] are among the main approaches for focusing light to subwavelength volumes.

The field of plasmonics also offers a powerful alternative and unique opportunity for bridging the gap between optical wavelength and nanometer sizes [Schuller *et al.* (2010)], as shown in Figure 1.1 (b). In particular, plasmonics combines the size of nanolectronics and the speed of dielectric photonics, enabling devices that might naturally interface with similar-speed photonics devices and with similar-sized electronic components, thus enhancing the synergy between these two technologies [Brongersma & Shalaev (2010)]. However, before this scenario can be realized, some open challenges need to be fully addressed, such as how to compensate resistive heating losses in plasmonic systems or – the topic of this thesis – how to effectively control their optical response in space and time on a nanometer scale.

1.2 Surface Plasmon Optics

The phenomenon of Surface Plasmons (SPs) is one of the many physical phenomena arising from the interaction between light and matter. Its origin stems from the unique properties of metals at optical frequencies: at these frequencies, metals, especially noble metals such as gold and silver, have a large negative real part along with a small imaginary part of the dielectric constant. A similar phenomenon, therefore, cannot be reproduced in other spectral ranges, where metals behave as perfect conductors, by simply using the scale invariance of Maxwell's equations.

This Section, after reviewing the optical properties of noble metals, introduces some fundamental concepts about surface-plasmon optics. Depending on the geometry of the metal structure, in particular, two distinct types of SPs can be identified (Figure 1.2): Surface Plasmon Polaritons (SPPs) [Raether (1988)] and Localized Surface Plasmons (LSPs) [Kreibig & Vollmer (1993)]. SPPs, sustained at a metal-dielectric interface, are propagating electromagnetic surface waves associated to collective oscillation of the free electrons of the metal due to an incident electromagnetic field (Figure 1.2 (a)) [Barnes *et al.* (2003)]. In contrast, LSPs, which this Thesis mainly deals with, are associated with bound electron clouds in nano-voids or particles with dimensions much smaller than the wavelength of the incident light (Figure 1.2 (b)) [Schuller *et al.* (2010)]. While for SPPs propagating on plane interfaces the electromagnetic field is strongly localized just in the dimension perpendicular to the interface, LSPs are able to confine the field in two or three dimensions, thus offering higher control over light fields on a subdiffraction scale.

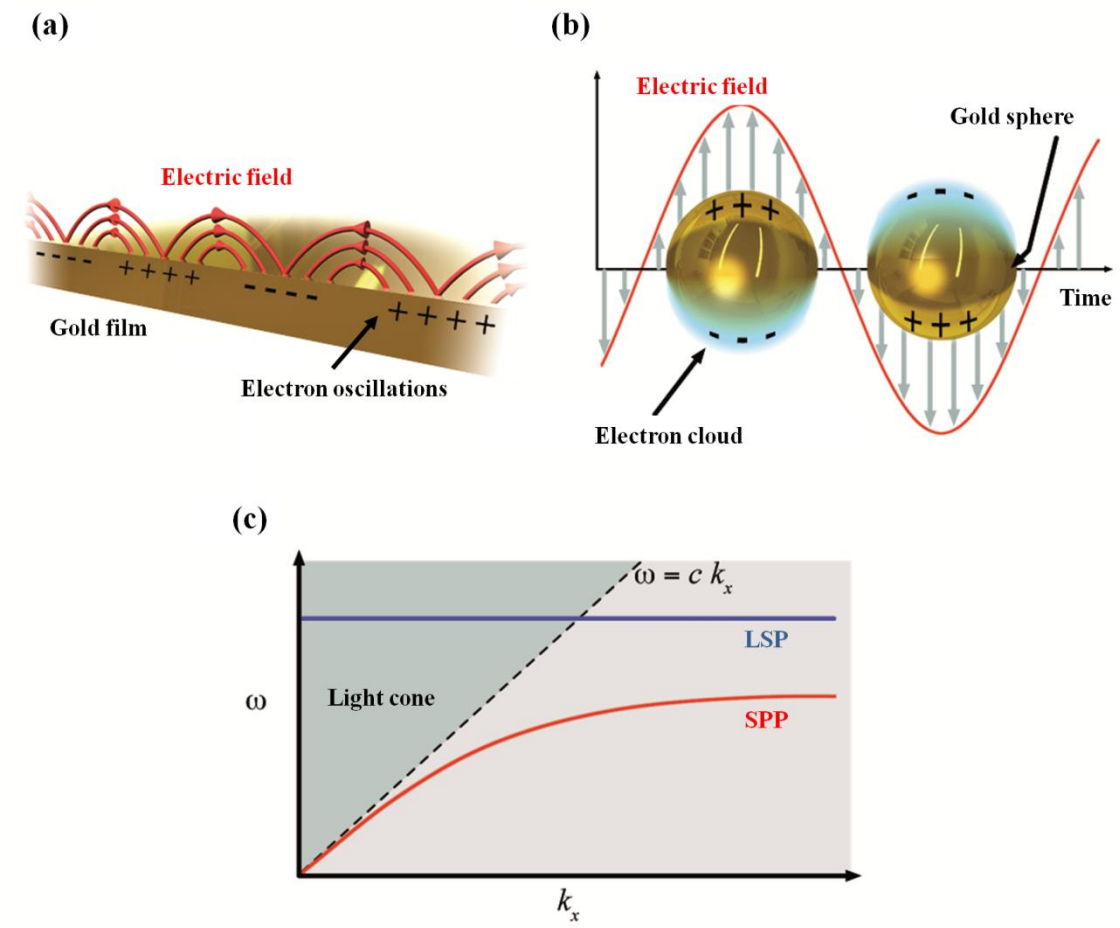

Figure 1.2: Surface Plasmon Polaritons vs. Localized Surface Plasmons. (a) *SPPs at the interface between a metal and a dielectric material are propagating electromagnetic surface waves associated to collective oscillations of the free electrons of the metal driven by the incident electromagnetic field.* (b) *In contrast, LSPs are associated with bound electron clouds in nano-voids or particles; these electron clouds oscillate in phase with the incident electric field when the particle's dimension is much smaller than the wavelength of light.* (c) *The dispersion curve for a SPP (red line) typically lies to the right of the light cone (delimited by the dashed black line) and spreads over a wide range of frequencies: the SPP momentum is therefore greater than the momentum of a free space photon of the same frequency. The LSP dispersion curve (blue line) exists only over a narrow frequency range and it intersects the light cone: in contrast to SPPs, therefore, LSPs can be directly coupled with propagating light.*

1.2.1 The dielectric function of noble metals

The optical properties of metals can be described by their complex dielectric constant $\varepsilon_m(\omega)$ that depends on the frequency of light [Novotny & Hecht (2006); Maier (2007)]. Assuming that the conduction electrons can move freely within the bulk of the material, the Drude-Sommerfeld model for the free electron gas, in particular, leads to this expression for the dielectric constant of a real metal:

$$\varepsilon_m(\omega) = \varepsilon_\infty - \frac{\omega_p^2}{\omega^2 + i\gamma\omega}, \tag{1.5}$$

where ω_p is the volume plasma frequency of the free electron gas, γ is a damping term due to scattering events between electrons, and ε_∞ is a fitting constant parameter greater than, or equal to, one.

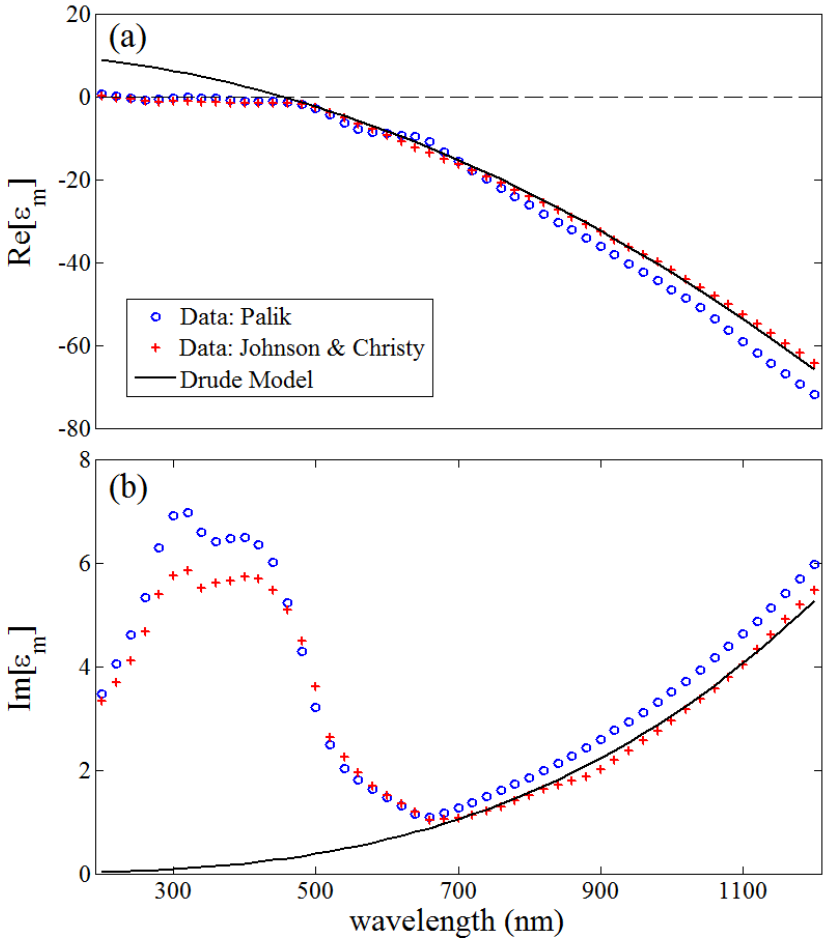

Figure 1.3: Dielectric function of gold. *Real part* (a) *and imaginary part* (b) *of the dielectric function of gold. The blue circles and the red crosses represent experimental values taken respectively from [Palik (1985)] and [Johnson & Christy (1972)]; in the two sets of data, despite some discrepancy, the real part of the dielectric constant is negative over the extended visible range. The black continuous line represents the fitting of Equation (1.5) to Johnson & Christy's data. The model accurately describes the experimental optical properties of the metal in the infrared regime, while in the visible ($\lambda < 700\ nm$) it needs to be supplemented with additional terms to take into account the response of bound electrons.*

Figure 1.3 is a plot of the experimental values of the dielectric constant for gold (real and imaginary part) according to [Palik (1985)] – blue circles – and [Johnson & Christy (1972)] – red crosses: in both cases, the real part of the dielectric constant is

negative over the extended visible range. The imaginary part of the dielectric constant, instead, describes the dissipation of energy associated with the motion of the electrons in the metal [Novotny & Hecht (2006)]. Differently from other frequency ranges, where metals behave as perfect conductors, one consequence of the negative real part of the dielectric constant is the fact that light can penetrate into the metal, albeit only to a very small extent. The black continuous line in Figure 1.3 fits the Drude-Sommerfeld model to Johnson & Christy's data using $\omega_p = 13.8 \cdot 10^{15} s^{-1}$ and $\gamma = 1.075 \cdot 10^{14} s^{-1}$, which are the values for gold reported in [Okamoto (2001)]: in the infrared regime for wavelength above $650\,nm$, the optical properties of the metal can be accurately described by the Drude-Sommerfeld model; in the visible, the model needs to be supplemented to take into account the response of bound electrons [Novotny & Hecht (2006)]. For gold, for example, at a wavelength shorter than approximately $550\,nm$, the measured imaginary part of the dielectric function increases much more strongly, as predicted by the model, mainly because higher energy photons can promote electrons of lower-lying bands into the conduction band.

1.2.2 Surface Plasmon Polaritons (SPPs)

As already introduced, SPPs are surface light waves that occur at the interface between a conductor and a dielectric as the result of the interaction of an incident electromagnetic field with the free electrons of the conductor [Barnes *et al.* (2003)]. In this interaction, the free electrons respond collectively by oscillating in resonance with the incident field, thus generating light waves trapped at the interface between the conductor and the dielectric (Figure 1.2 (a)).

Mathematically, these localized modes can be found as a solution of the electromagnetic wave equation when the dielectric constants – $\varepsilon_1$and ε_2 – of the media at both sides of the interface satisfy the following conditions [Novotny & Hecht (2006); Maier (2007)]:

$$\begin{cases} \varepsilon_1 \cdot \varepsilon_2 < 0 \\ \varepsilon_1 + \varepsilon_2 < 0' \end{cases} \tag{1.6}$$

which means that the real part of one of the dielectric functions must be negative with an absolute value exceeding that of the other. Therefore, SPPs can exist at the interface between a noble metal and a dielectric, but not between two dielectrics.

In contrast to the propagating nature of SPPs in the surface plane, the field perpendicular to the propagation direction decays exponentially with distance from the surface. Moreover, as a consequence of the interaction between surface charge density and the incident electromagnetic field, the momentum of SPPs is greater than that of a free-space photon of the same frequency [Barnes *et al.* (2003)], as show in Figure 1.2 (c) where the SPP dispersion curve lies at the right of the light cone. SPPs, therefore, do not couple directly to light propagating in free space, and their excitation requires special configurations either relying on coupling via evanescent waves, such as the

Kretschmann configuration [Kretschmann & Raether (1968)] and the Otto configuration [Otto (1968)], or on gratings and defects at the surface [Lopez-Tejeira *et al.* (2007); Renger *et al.* (2007)] in order to compensate for this momentum mismatch between the SPP and the incident radiation. Recently, the direct excitation of SPPs on a metal surface was demonstrated by nonlinear mixing of free-propagating photons [Renger *et al.* (2009)].

1.2.3 Optical properties of resonant metal nanoparticles (LSPs)

As shown in Figure 1.2 (b), LSPs, unlike SPPs on flat and extended metal surfaces, comes into play when the metal dimensions are much smaller than the wavelength of the incident light [Schuller *et al.* (2010)]. Whilst SPPs have a continuous dispersion relation and, thus, exist over a wide range of frequencies, LSP resonances only exist over a narrow frequency range due to additional constraints imposed by their finite dimensions. Moreover, also in contrast to SPPs, LSPs can be directly coupled with propagating light (Figure 1.2 (c)): in fact, their enhanced scattering cross-section at resonance makes of them very efficient antennas.

The physical origin behind LSP resonances can be better understood by means of a simple model structure, such as a sphere. The scattering of a sphere can be evaluated analytically by calculating its electric polarizability α [Kreibig & Vollmer (1993)], as long as the particle is much smaller than the wavelength of the incident light λ – quasi-static approximation:

$$\alpha(\omega) = \varepsilon_0 V \frac{\varepsilon_m(\omega) - \varepsilon}{\varepsilon_m(\omega) + 2\varepsilon}, \tag{1.7}$$

where V is the volume of the sphere, ε_m and ε the respective dielectric constants of the metal and of the surrounding medium. Looking at the denominator of Equation (1.7), when the real part of the dielectric function of the metal is negative and matches 2ε, the polarizability experiences a resonance, which is responsible for an enhancement in the scattering and absorption cross-sections of the sphere [Kreibig & Vollmer (1993)].

The spectral position of this resonance and, therefore, the optical properties of single plasmonic nanoparticles can be controlled by tailoring the particles' size and shape, as well as the dielectric functions of the metal and the surrounding media. By extending Equation (1.7) to non-spherical geometries, such as an ellipsoid, the spectral position of the polarizability resonance becomes directly dependant on the particle geometrical parameters. In the quasi-static approximation, the electric polarizability α_i along one of the principal axis of an ellipsoid ($i = a, b, c$) can be derived analytically [[Kreibig & Vollmer (1993)]]:

$$\alpha_i(\omega) = \varepsilon_0 V \frac{\varepsilon_m(\omega) - \varepsilon}{\varepsilon + L_i(\varepsilon_m(\omega) - \varepsilon)}, \tag{1.8}$$

where V is the volume of the ellipsoid, and L_i is a purely geometric factor that, for spheroids, is a complex function of their eccentricity e. For the specific case of a prolate spheroid ($a > b = c$),

$$L_a = \frac{1-e^2}{e^2}\left[\frac{1}{2e}\ln\frac{1+e}{1-e} - 1\right], \tag{1.9}$$

while the remaining factors L_b and L_c are fixed by the relation $\sum L_i = 1$. Now therefore, the zero of the denominator in the Equation (1.8) determines the wavelength of the ellipsoid's optical resonance also as a function of its geometry.

From the expression of the polarizabilty $\alpha(\omega)$, the absorption cross-section C_{abs} and the scattering cross-section C_{sca} of the spheroid can now be calculated [Kreibig & Vollmer (1993)], by using:

$$\begin{cases} C_{abs} \sim \frac{2\pi}{\lambda}\mathrm{Im}[\alpha] \\ C_{sca} \sim \frac{1}{6\pi}\left(\frac{2\pi}{\lambda}\right)^4 |\alpha|^2 \end{cases}. \tag{1.10}$$

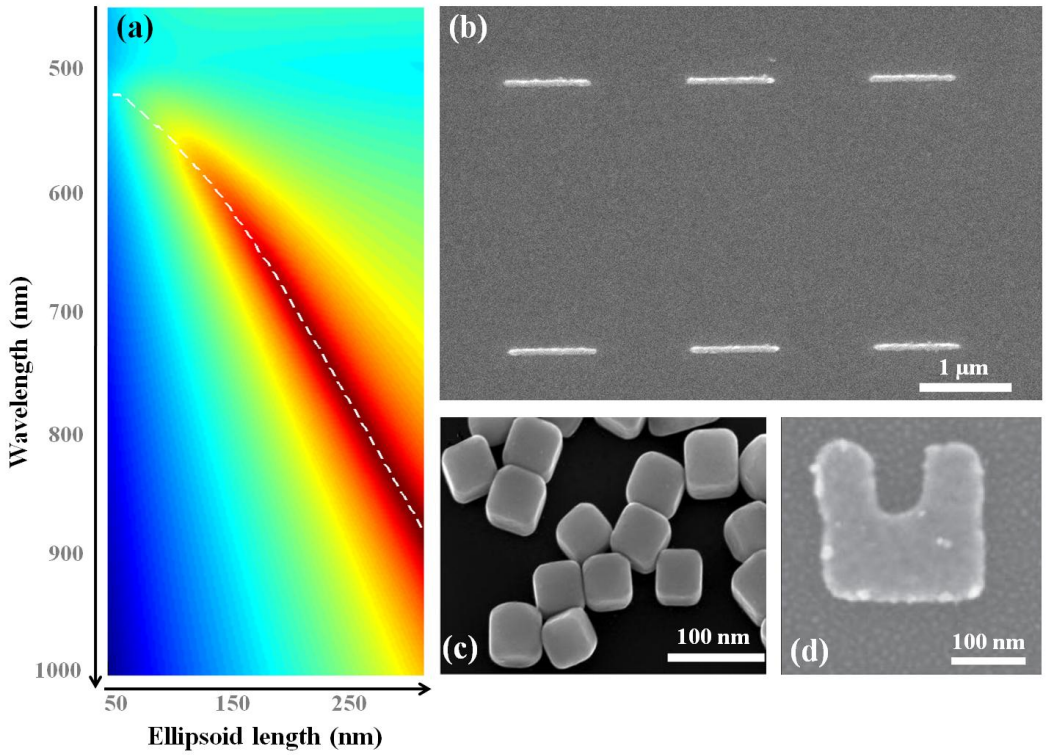

Figure 1.4: Optical properties of single nanoparticles. (a) *Analytical scattering cross-section of a gold prolate spheroid ($a > b = c = 40$ nm) as a function of the length of its long axis and the wavelength of the incident light (ε_{gold} is taken from [Johnson & Christy (1972)] and $\varepsilon_{air} = 1$): the dashed white line highlights the red-shift of the resonance as the lengths of the ellipsoid's long axis increases;* (b-d) *various examples*

of plasmonic nanostructures: (b) *gold nanorods fabricated by e-beam lithography,* (c) *chemically synthesized, truncated silver cubes [Sun & Xia (2002)], and a split-ring resonator also fabricated by e-beam lithography [Husnik et al. (2008)].*

Figure 1.4 (a) represents the logarithm of the scattering cross-section of a gold spheroid in air (ε_{gold} is taken from [Johnson & Christy (1972)] and $\varepsilon_{air} = 1$) as a function of its eccentricity and the wavelength of the incident light; the dashed white line, in particular, highlights how the resonance of the scattering cross-section shifts with the increasing eccentricity of the spheroid: the more eccentric – hence, the more prolate – the spheroid, the more red-shifted is its resonance. The same qualitative trend can be observed experimentally on ellipsoids [Grand *et al.* (2006)] and rods [Link *et al.* (1999)], in spite of the intrinsic limitations of this simple model, which become more prominent when the structures stop to be much smaller than the wavelength of light. In this case, full 3D solvers of the Maxwell equations can give more reliable results and fit better the resonances of real structures [Grand *et al.* (2006); Link *et al.* (1999)].

The same capability of tuning the optical properties, as a function of the wavelength and the polarization of the incident light, has also been shown in very differently shaped nanostructures, such as in polyhedral particles [Noguez (2007)], nanocups and nanoshells [Knight & Halas (2008)], or nanostars [Nehl *et al.* (2006)]. Figure 1.4 (b-d) show a few different geometries of possible nanostructures, fabricated either with *bottom-up* or *top-down* approaches.

1.2.4 The emerging concept of optical antennas

In the past decades, the concept of nanoantennas has emerged in nano-optics as an enabling technology for controlling the spatial distribution of light at subwavelength scales [Bharadwaj *et al.* (2009); Novotny & van Hulst (2011)]. Great effort, in particular, has been devoted to scaling antenna concepts, operating at radiowaves and microwaves, down to the optical regime, where the antenna's otherwise poor performance can be substantially enhanced by LSP resonances.

The objective of optical antenna design is equivalent to that of classical antenna design: to optimize and control the energy transfer between a localized source or receiver and free radiation (Figure 1.5). In standard antenna theory, where metals are perfect conductors, the characteristic length L of an antenna is directly related to the wavelength λ of the incoming – or outgoing – radiation [Balanis (2005)]:

$$L = const\ \lambda, \tag{1.11}$$

where $const$ is a design constant, for example $const = 1/2$ for an ideal half-wave dipole antenna. The behavior of the antenna, therefore, is completely governed by its geometry.

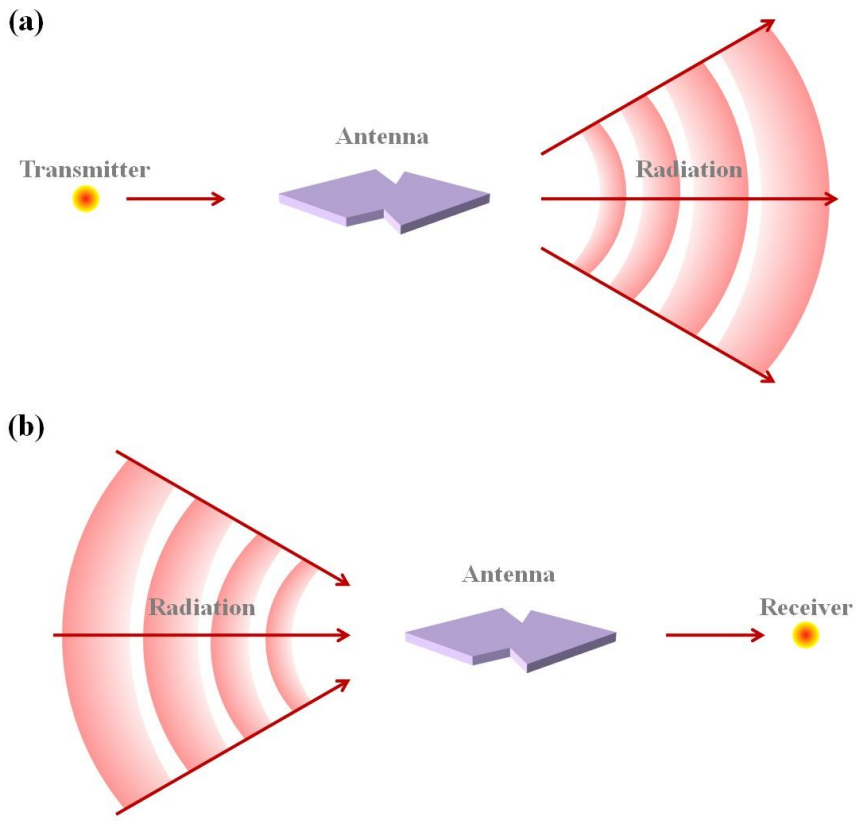

Figure 1.5: Design of a nanoantenna. (a) *Emitting antennas and* (b) *receiving antennas are designed to optimize the transfer of propagating radiation respectively, from a localized source or to a receiver. The arrows indicate the direction in which the energy flows. Figure adapted from [Novotny & van Hulst (2011)]*.

At optical frequencies, however, where metals behave as strongly coupled plasma, what turns metallic nanoparticle into very efficient antennas is mainly the possibility of exploiting their plasmonic resonant behavior. In this frequency regime, in fact, the mere wavelength scaling breaks down because the incident radiation is no longer perfectly reflected from the surface of the metal. The antenna, therefore, no longer responds to the incident wavelength in vacuum, but to a shorter effective wavelength λ_{eff}, which is controlled not only by the shape of the nanoantenna but also by intrinsic plasmonic effects related to the dielectric properties of the metal structure and its surroundings [Novotny (2007)]. Using a model based on a metal cylindrical waveguide, the effective wavelength in optical antennas, therefore, can be expressed as:

$$\lambda_{eff} = n_1 + n_2 \frac{\lambda}{\lambda_p}, \tag{1.12}$$

where λ_p is the plasma wavelength of the metal, and n_1 and n_2 are coefficients that depend on the geometry of the antennas and the dielectric properties of the system materials. We can, therefore, rewrite Equation (1.11) by replacing λ with λ_{eff}: for metal

nanorods described as Fabry-Pérot cavities, for example, the relation between characteristic length L and effective wavelength λ_{eff} reads as [Giannini *et al.* (2011)]:

$$L = \frac{n}{2}\lambda_{eff}, \tag{1.13}$$

where n is an integer number. This equation forces the effective wavelength of the LSP resonance to fit exactly a half-integer number of times into the nanoparticle length.

Moreover, despite the widespread use of radiowave and microwave antennas, their optical analogues still raise technological challenges connected to their fabrication: as shown in Equation (1.12) and (1.13), the characteristic dimensions of an antenna are smaller than the radiation wavelength, and for optical antennas this requires fabrication accuracies at least in the order of a few tens of nanometers. Recently, however, prototype optical antennas have been devised using *top-down* or *bottom-up* nanofabrication tools [Mühlschlegel *et al.* (2005); Ghenuche *et al.* (2008); Kalkbrenner *et al.* (2005)].

1.3 Static Control of the Response of Nanoantennas

Tailoring the shape and the dimensions of metal nanoparticles is a fundamental ingredient in order to tune plasmonic resonances and to control light fields on the nanoscale [Schuller *et al.* (2010); Giannini *et al.* (2011)]. This concept is well known in standard antenna theory, where an antenna of a specific length is at resonance with a certain wavelength of light, as seen in Equation (1.11). Even though the spectral properties of a metallic nanoparticle are governed not only by its size and shape but also by the dielectric functions of both metal and surrounding media, the most straightforward way to tune its resonance to a different wavelength would still be to physically change the dimensions of the antenna.

In the past decade, the emergence of efficient nanofabrication techniques has made possible to engineer the electromagnetic response of metal nanostructures with an unprecedented accuracy and selectivity as a function of the wavelength and polarization of light. Some of these techniques are based on chemical synthesis [Jin *et al.* (2001), Sun & Xia (2002)], others rely on nanofabrication tools, such as electron-beam lithography [Craighead & Niklasson (1984); Krenn *at al.* (2000)], electron-beam induced deposition [Graells *et al.* (2007)], nano-imprint lithography [Fernandez-Cuesta *et al.* (2007)], or focused ion-beam milling [Ebbesen *et al.* (1998)]. Only recently, approaches that combine top-down and bottom-up techniques have made their appearance on the scientific scene [Huang *et al.* (2011)].

1.3.1 Engineering of single nanoparticles and nanowires

As seen in Section 1.2.3, the optical properties of single metallic nanoparticles, as a function of the wavelength and the polarization of the incident light, can be controlled

by tailoring their shape and dimensions as well as the dielectric functions of both the constitutive metal and the surrounding media. Nanoparticles and nanorods similar to those of Figure 1.4 (b) are among the simplest geometries of plasmonic antennas used for focusing free-space propagating light on the nanoscale.

Alternatively, nanofocusing of light can be achieved by the compression of SPPs propagating along tapered metallic nanowires [Novotny & Hafner (1994); Stockman (2004); Schnell *et al.* (2011)] or slot waveguides [Pile & Gramotnev (2006); Choi *et al.* (2009); Vedantam *et al.* (2009)], at whose apexes very strong charge gradients can be generated. In this case, rather than a free-space propagating wave, a propagating surface wave is focused. In these structures, the SPP excitation and the focus at the taper apex are spatially separated, thus offering an improved signal-to-noise ratio for some applications to near-field microscopy.

Finally, the geometry of a nanostructure can be further engineered in order to obtain an optimal electromagnetic response for a given application: the split ring resonators of Figure 1.4 (d), for example, are designed to have a strong magnetic response in the optical regime [Husnik *et al.* (2008)].

1.3.2 Engineering of ensembles of coupled nanoparticles

In many applications involving metal nanoparticles, an important role is played by ensembles. Nowadays, it is clear that the plasmonic properties of a nanosystem strongly depend on the interplay between its constituting particles [Su *et al*. (2003); Prodan *et al*. (2003)]: in fact, coupled plasmonic oscillations take place whenever the near-field of a particle interacts with that of an adjacent particle [Kreibig & Vollmer (1993)]. The resonance of the coupled system occurs at a wavelength that is red-shifted from the resonance of an isolated particle, and the magnitude of this shift depends on the strength of the coupling between particles, which, in turn, depends on their proximity [Su *et al*. (2003)]; interestingly, even though the absolute plasmon shift depends on many factors, such as the size and shape of the particles, the type of metal, and the surrounding medium, an independent universal scaling trend of the fractional shift of the wavelength $\Delta\lambda/\lambda_0$ can be observed when the distance s between two particles is scaled by their characteristic dimension D [Jain *et al.* (2007); Jain & El-Sayed (2008)]:

$$\frac{\Delta\lambda}{\lambda_0} = \frac{\lambda_1 - \lambda_0}{\lambda_0} \sim k e^{-\frac{s}{\tau D}}, \tag{1.14}$$

where λ_1 and λ_0 are the resonances of the coupled system and of the isolated particle respectively, k is a fitting constant, and $\tau \approx 0.2$ for gold particles [Jain & El-Sayed (2008)]. A more recent study offer an alternative theoretical approach to determine the optical properties of nanoparticle dimers when connected by conductive gap linkers [Pérez-González *et al.* (2011)].

Near-field coupling between adjacent plasmonic particles can also lead to strong surface charge gradients in the separation gap between adjacent particles, thus

dramatically enhancing the intensity of the incident light by many orders of magnitude. This effect, for example, was theoretically studied on a system of coupled gold nanorods in 2005 [Aizupurua *et al.* (2005)]. That same year, nanofabricated resonant optical antennas were experimentally demonstrated [Mühlschlegel *et al.* (2005]: a strong field enhancement was observed in the gap of gold dipole nanoantennas that had been designed and fabricated to be resonant at optical frequencies. Later in 2008, more quantitative data were acquired that, as shown in Figure 1.6, compared clearly the optical near-field of a single gold nanorod to that emitted by two coupled nanorods of the same length [Ghenuche at al. (2008)].

Alternatively, other coupled geometries of two or more particles have also been proposed for purposes of field enhancement and light confinement on the nanoscale, such as bowtie antennas [Schuck *et al.* (2005)], self-similar chains [Li *et al.* (2003)], and periodic one-dimensional arrangements of metal nanoparticles [Ghenuche *et al.* (2007)].

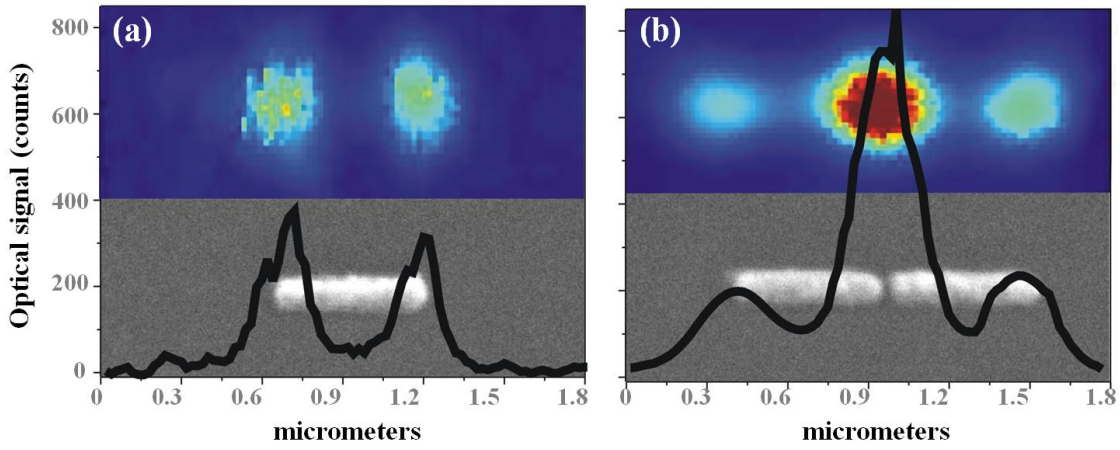

Figure 1.6: Field enhancement in the gap of two coupled nanorods. *Optical signal and respective SEM micrographs of (a) a single gold nanorod and* (b) *two coupled gold nanorods. The coupled system shows a much higher field enhancement than the single rod because of a strong charge gradient at the gap. Each rod is 500 nanometers long. Picture adapted from [Ghenuche et al. (2008)]*.

1.4 Dynamic Control of the Response of Nanoantennas

Recent progresses in numerical modeling, together with the spreading of nanofabrication techniques, have enabled researchers to accurately engineer the optical properties of plasmonic nanostructures for specific applications. For instance, engineered plasmonic nano-objects are being used for data storage [Zijilstra *et al.* (2009)], microscopy [Yano *et al.* (2009)], solar cells [Atwater & Polmann (2010)], optical trapping [Juan *et al.* (2011)], molecular sensors [Acimovic *et al.* (2009)], as well as for tailoring the emission pattern of single-photon emitters [Ringler *et al.* (2008)].

In all these cases, the optical near-field distribution resulting from the interaction between light and plasmonic nanostructures is mostly determined by the geometry of the metal system and the properties of the incident light, such as its wavelength and its polarization. In the past decade, in particular, one of the biggest achievements in plasmonics was the possibility of creating intense fields on the nanometer scale [Schuller *et al.* (2010)] – the so called *hot spots*.

While a modification of the wavelength or the polarization of the incident light can induce substantial changes in the near-field distribution [de Waele *et al.* (2007); Hrelescu *et al.* (2011)], it does not enable controlling the location of these *hot-spots* at any desired position of a generic nanostructure. Nonetheless, the accurate and dynamic control of the optical near field at the subwavelength scale is required for the development of future nano-optical devices and to extend concepts and functionalities of macroscopic optics down to the nanometer scale [Stockman *et al.* (2002)].

Such control cannot be managed by simply focusing light from the far-field because of the limit of diffraction (Section 1.1). Two different main strategies have been proposed in order to overcome this fundamental limitation: the first aims to generate coherent interference of surface plasmons over time and space, while the second aims to induce a different optical response of a nanosystem by dynamically tuning its physical properties, such as the refractive index of the surrounding. Alternatively, scanning probe techniques have also been proposed to launch surface plasmons at freely chosen positions by scanning subdiffraction excitation sources in the near-field, for example by placing a single-photon emitter on a dielectric tip [Cuche *et al.* (2010)], by exploiting the field enhancement of a nanoantenna [Riedel *et al.* (2010)] or by tunneling low-energy electrons [Bharadwaj *et al.* (2011)].

1.4.2 Coherent control

Shaping the amplitude and phase of femtosecond light pulses is a useful tool to dynamically generate waveforms that are modulated both in frequency and space and that can be focused onto microscopic time domains on a femtosecond time scale [Wefers & Nelson (1993); Feurer *et al.* (2003)]. This shaping offers a unique opportunity to coherently control ultrafast phenomena on the nanoscale, where the phase and the polarization of the excitation pulse provide additional degrees of freedom to perform such a control.

In 2002, Stockman and colleagues postulated the possibility of concentrating local fields in plasmonic nanostructures at a desired location in time and space with a femtosecond and nanometric accuracy, by suggesting the phase modulation of the excitation pulse of light [Stockman *et al.* (2002); Stockman *et al.* (2004); Durach *et al.* (2007)]. This effect is based on the interference between the different components of the incident radiation: the excitation field takes energy away from those parts of the nanosystem whose oscillations are out of phase with the driving pulse, and moves it to those parts whose oscillations are in phase [Stockman *et al.* (2002)]. The femtosecond evolution of this interference phenomenon was observed on a corrugated silver film by

means of a pump-probe experiment combined to photoelectron emission microscopy [Kubo *et al.* (2005)].

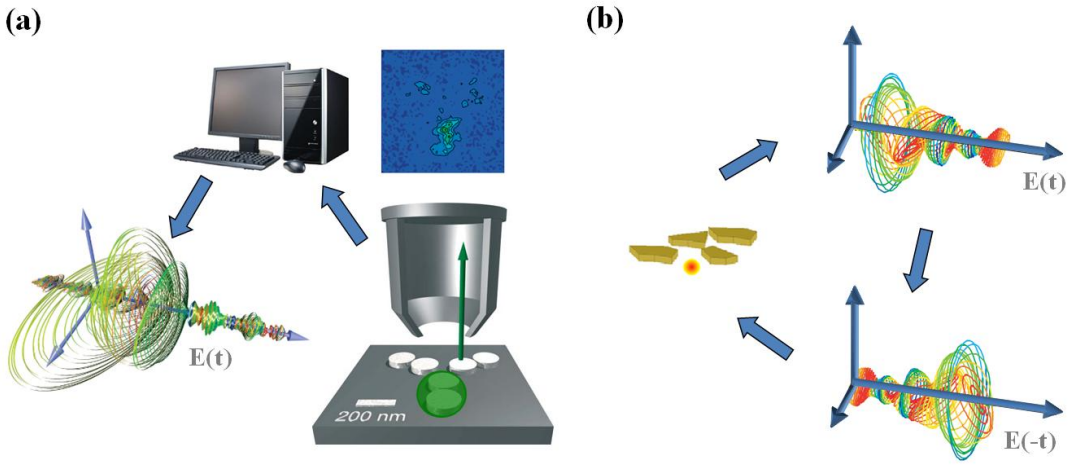

Figure 1.7: Examples of coherent control. (a) *Adaptive control: the optical near-field response of a silver nanostructure is dynamically tailored through the adaptive polarization shaping of a series of femtosecond laser pulses This approach requires the combination of a multiparameter pulse shaper with a learning algorithm.* (b) *Time reversal: a femtosecond optical nanosource is locally coupled to the plasmonic oscillations of a complex nanostructure, which in change radiates in the far-field. Reversing this radiation in time and feeding it back to the system is enough to localize its energy at the nanosource's initial position. Pictures respectively adapted from [Aesclimann et al. (2007)] and [Li & Stockman (2008)]*.

A few years later, the adaptive shaping of the phase and amplitude of femtosecond laser pulses was proposed as an efficient tool for the direct manipulation of interference phenomena in plasmonic systems [Brixner *et al.* (2005); Brixner *et al.* (2006)]. A first experimental implementation of this idea came across in 2007, when Aeschlimann and colleagues were able to dynamically tailor the optical near-field response of a silver nanostructure through the adaptive polarization shaping of femtosecond laser pulses [Aeschlimann *et al.* (2007)].

Finally, in 2008 the idea of time reversal was also theoretically proposed in order to dynamically control the optical near-field response of plasmonic structures [Li & Stockman (2008)]. In this approach, a femtosecond optical nanosource, such as a single-photon emitter, is locally coupled to the plasmonic oscillations of a complex system, which in change radiates in the far-field. Reversing this radiation in time – and feeding it back to the original system as an excitation wave – recreates the right illumination conditions to concentrate light at the initial position of the local nanosource.

1.4.2 Alternatives to coherent control

Alternative strategies to coherent control mainly aim to tune the optical response of a plasmonic nanosystem by dynamically changing either its geometry or the refractive index of the background media: for example, reversible electrochemical and molecular switches were successfully employed to tune the spectral resonance of an ensemble of nanoparticles [Leroux *et al.* (2005); Zheng *et al.* (2009)]. In contrast to coherent control, however, these approaches typically produce a more limited amount of control, since the optical response of the nanosystem can be switched only between a few allowed states.

Nematic liquid crystals, whose optical properties can be tuned electrically, have been vastly employed to induce reversible local changes in the refractive index of the medium surrounding a metal nanostructure [Müller *et al.* (2002); Park & Stroud (2004); Chu *et al.* (2006); Evans *et al.* (2007); Dickson *et al.* (2008); Berthelot *et al.* (2009)].

In the case of pairs of antennas, their near-field coupling can be precisely controlled mechanically [Olk *et al.* (2008); Merlein *et al.* (2008)] or photochemically [Härtling *et al.* (2008)].

Finally, in the field of metamaterials, the optical response of large otherwise passive arrays of nanoparticles can be rendered active by integrating dynamic components into the design with similar strategies to the one discussed above. At the resonant wavelength, for example, the amplitude of the response of optical metamaterials can be modulated via electrical carrier injection in semiconductor substrates [Chen *et al.* (2006)] or mechanical reorientation of the resonant nanostructures using microelectrochemical systems [Tao *et al.* (2009)]. Frequency modulation has also been demonstrate by changing the dielectric environment around the nanostructures with phase-transition materials [Dicken *et al.* (2009); Samson *et al.* (2010)], liquid crystals [Xiao *et al.* (2009)], and optical pumping of the substrate [Chen *et al.* (2008)]. Alternatively, exploiting the elasticity of a complaint substrate, the resonant frequency of a metamaterial can be tuned by changing the distance, and thus the coupling strength, between pairs of nanostructures [Pryce *et al.* (2010)].

Chapter 2

Fractal Plasmonics

The previous chapter reviewed the advances in the control of the optical response of plasmonic nanostructures – either by a static or by a dynamic approach – at the time the research work of this thesis was initiated.

Tailoring the shape and the dimensions of metal nanoparticles comes across as a fundamental ingredient in order to engineer both spectral and spatial features of plasmonic light fields on the nanoscale: the response, upon illumination at a given wavelength and polarization, is ultimately governed by the characteristic lengths associated to the shape and size of the nanostructure under study. As an example of novel static control, this chapter introduces the use of fractal geometries in the design of engineered plasmonic structures as a promising way to increase the number of characteristic lengths within the nanostructures, thus extending the degrees of freedom and the parameters available for their design [Volpe *et al.* (2011)].

Here, the focus is on a paradigmatic fractal geometry, namely the Sierpinski carpet, and on the possibility of using it to achieve a controlled broadband spectral response by controlling the degree of its fractal complexity. Furthermore, some other arising properties, such as subdiffraction limited focusing and its potential use for optical trapping of nano-objects, are also discussed. An especially attractive advantage of the focusing over more standard geometries, such as gap antennas, is that it occurs away from the metal surface, leaving an open space accessible to objects for enhanced light-matter interaction.

2.1 Fractals and Nano-Optics

The term *fractal* was first coined by French-American mathematician Benoît Mandelbrot in 1975, and it was derived from the Latin word *fractus* meaning *broken* or *fractured*. Strictly speaking, a fractal is a rough or fragmented geometric shape that can be split into parts, each of which is, at least approximately, a reduced-size copy of the whole [Mandelbrot (1982)]. A fractal is, therefore, a geometrical shape whose parts resemble, at least statistically, the whole. This often makes fractals *self-similar*, i.e. parts look like each other and like the whole object. From the mathematical point of view, a fractal is based on an equation that undergoes iteration.

Since the publication of Mandelbrot's book *The Fractal Geometry of Nature* in 1982 [Mandelbrot (1982)], multiple-scale properties of fractal geometries have proven useful in studying phenomena with recurring features at progressively smaller scales, from eroded coastlines to snowflakes and from Internet networks to galaxy formation [Peitgen *et al.* (1992)]. In particular, the design of fractal geometries has been employed in the development of multiband compact fractal antennas for mobile telecommunication devices and radio-frequency (RF) infrastructures [Werner & Ganguly (2003)].

2.1.1 The Sierpinski carpet

The Sierpinski carpet is one of the most studied fractal geometries. It is named after Polish mathematician Waclaw Sierpinski who first described it in 1916 [Sierpinski (1916)]. In this chapter, this paradigmatic fractal also serves as test geometry to show the far-reaching properties of the combination between plasmonics and engineered fractal designs.

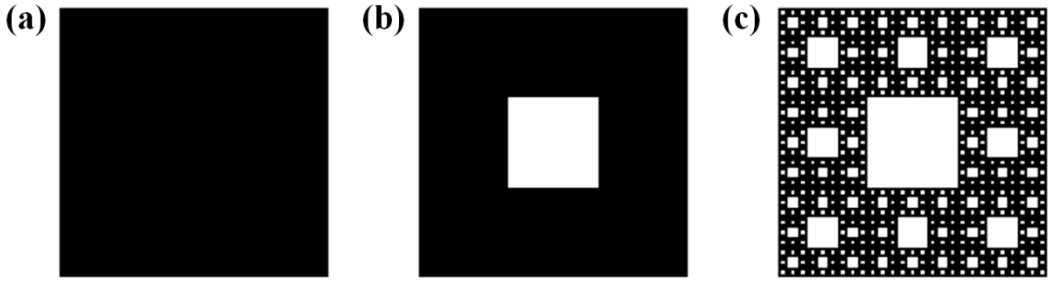

Figure 2.1: Construction of the Sierpinski carpet. (a) *First,* (b) *second, and* (c) *fourth step of the construction process of the fractal. At any iteration, new length scales are added to the resulting figure.*

Figure 2.1 shows the construction procedure of the Sierpinski carpet, procedure that will be useful later in this chapter. The construction starts with a square of side length l – the zeroth fractal order (Figure 2.1 (a)). This square is then divided into a grid of $3x3$ $l/3$-sided squares and the central sub-square is removed – the first fractal order (Figure 2.1 (b)). The same procedure is then recursively applied to the remaining 8 squares, in principle *ad infinitum*. The result of the first four iterations – the third fractal order – is shown in Figure 2.1 (c). A very important characteristic of this process is that, at any iteration, new length scales are added to the resulting figure: the length scale of the original square is only l, while at any of the n-th order the length scale $l/3^n$ is also added.

2.1.2 Fractals in plasmonics: state of the art

Prior to the work presented in this thesis, studies of fractal geometries in plasmonics have mainly focused on self-organized metal clusters, while the design of *engineered* plasmonic fractal geometries still remains a largely unexplored territory that has just started to show its real potential. On the one hand, the optical properties of fractal self-organized metal clusters similar to the cluster shown in Figure 2.2 (a), in terms of spectral broadening, light confinement, and enhancement on the nanometer scale, have been studied in detail both theoretically [Shalaev & Stockman (1998); Shalaev (2002)] and experimentally [Tsai *et al.* (1994); Bozhevolnyi *et al.* (1998)]. Recently, for example, it has been shown how the statistical distribution of the local density of optical

states on disordered semi-continuous metal films exhibits a maximum in a regime where fractal clusters dominate the film surface [Krachmalnicoff *et al.* (2010)]. Because of the same random nature of the cluster formation process, however, these previous approaches suffer from poor control over the accurate positioning of the fractal nanostructures as well as over their fractal degree of complexity.

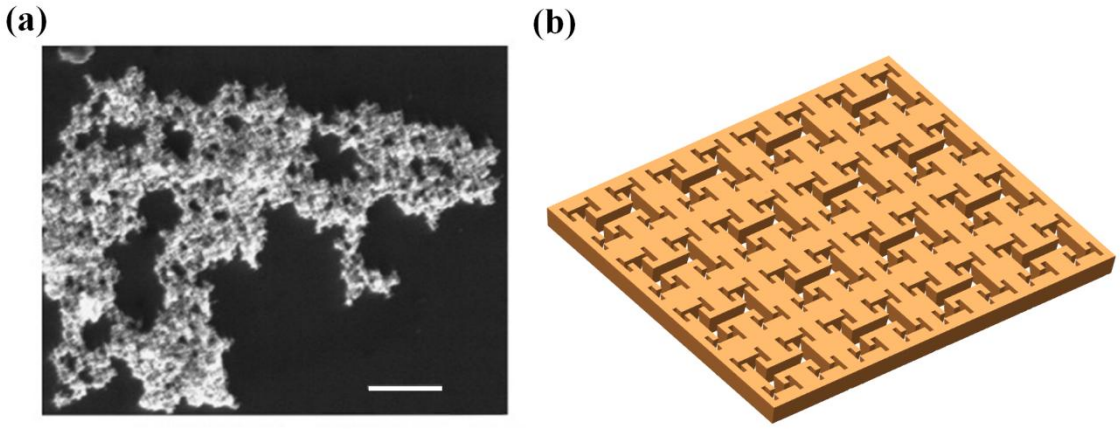

Figure 2.2: Examples of fractal geometries in optics. (a) *A SEM micrograph of a cluster of silver nanoparticles (the white scale bar represents 1 μm): the optical properties of similar random aggregation of metal nanoparticles, in terms of spectral broadening, light confinement, and field enhancement on the nanoscale, have been studied in details both theoretically and experimentally.* (b) *H-shaped metal patterns periodically milled in a metal film: in the microwave, mid- and far-infrared regime, metallic metamaterials, obtained by cutting fractal slits into metal films, have been able to rescale the concepts behind radiofrequency fractal antennas down to shorter wavelengths. Pictures respectively adapted from [Bozhevolnyi et al. (1998)] and [Huang et al. (2010)]*.

On the other hand, a few other studies have employed engineered metallic materials mainly to rescale the concepts behind radiofrequency fractal antennas down to shorter wavelengths [Werner & Ganguly (2003)]. In the microwave, mid- and far-infrared regime, metallic metamaterials, obtained by milling fractal slits into metal films, have shown to resonate at multiple self-similar wavelengths [Zhou *et al.* (2002); Wen *et al.* (2003); Bao *et al.* (2007)] or to be able of confining waves below the limit of diffraction [Miyamaru *et al.* (2008); Huang *et al.* (2010)]. In the visible, nonlinear light propagation has also been demonstrated in fractal waveguide arrays [Jia & Fleischer (2010)].

2.2 Optical Properties of a Sierpinski Nanocarpet

The combination between plasmonics and engineered fractal geometries has far-reaching properties that go beyond rescaling the concepts behind RF fractal antennas

down to shorter wavelengths, such as the possibility of supporting multiple resonances [Bao *et al.* (2007)].

In the following section, by numerically studying a specific plasmonic nanostructure based on the fractal geometry known as the Sierpinski carpet, examples of such a potential are presented. In particular, some of the structure's interesting emerging features at visible wavelengths, namely its broad spectral response and subdiffraction focusing, are highlighted. These properties are mainly due to an accurate control of the degree of the structure's fractal complexity. The application of the subdiffraction focus to optical manipulation is also briefly discussed.

The simulations were performed using the Green dyadic method [Appendix A]. In its discretized form, this formalism allows us to calculate the electric field scattered by a nanoparticle upon a given illumination at any position in space, both as a near-field intensity distribution and as a far-field scattering spectrum. All the calculated spectra are normalized to the volume of the gold of the structure under study, so that they are on a comparable scale.

Ideally the self-similarity of the plasmonic structure should be iterated *ad infinitum*; practically, however, here it was stopped at the third fractal order because of computational limits in the allocated computer memory. Moreover, the minimum characteristic lengths of the fractal were limited to the minimum feature size feasible with state-of-the-art fabrication techniques, i.e. about 20 nm for the minimum structure size and a few nanometers for the gaps between adjacent structures [Appendix B].

2.2.1 Broadband spectral response

As shown in Figure 2.3, the proposed Sierpinski carpet-like geometry features a broadband far-field spectrum, which may prove useful to enhance the coupling to a broadband light source, for solar cell applications for example [Atwater & Polman (2010)].

In order to construct the Sierpinski nanocarpet, we can follow a bottom-up approach, starting with a $50x50x25\ nm^3$ gold pad as basic element (pink structure in Figure 2.3 (a)) lying on a glass substrate (ε_{gold} is taken from [Palik (1985)], $\varepsilon_{glass} = 2.3$ and $\varepsilon_{air} = 1$). Its resonance upon plane-wave illumination with linear polarization along the x-axis is centered at $532\ nm$ with $59\ nm$ full width at half maximum (FWHM) (pink curve in Figure 2.3 (b)).

The first fractal order can be obtained arranging eight of these nanopads on a square frame grid leaving a separation of $5\ nm$ between them (red structure in Figure 2.3 (a)). It is resonant at $680\ nm$ with $56\ nm$ FWHM (red curve in Figure 2.3 (b)). Even though the FWHM slightly decreases, the red-shift of the central resonance wavelength is indicative of a strong near-field coupling of the nanopads forming the first fractal level.

The second fractal level is composed by a frame of the first-order fractals separated by $15\ nm$ gap (blue structure in Figure 2.3 (a)). It resonates at $760\ nm$ with $140\ nm$ FWHM (blue curve in Figure 2.3 (b)).

Finally, the third fractal level is built applying the same rule to the second-order fractals separated this time by 45 *nm* gap (black structure in Figure 2.3 (a)). Its resonance is centered at 720 *nm* with 295 *nm* FWHM (black curve in Figure 2.3 (b)), thus overlapping the solar radiation reaching the surface of the Earth [Atwater & Polman (2010)].

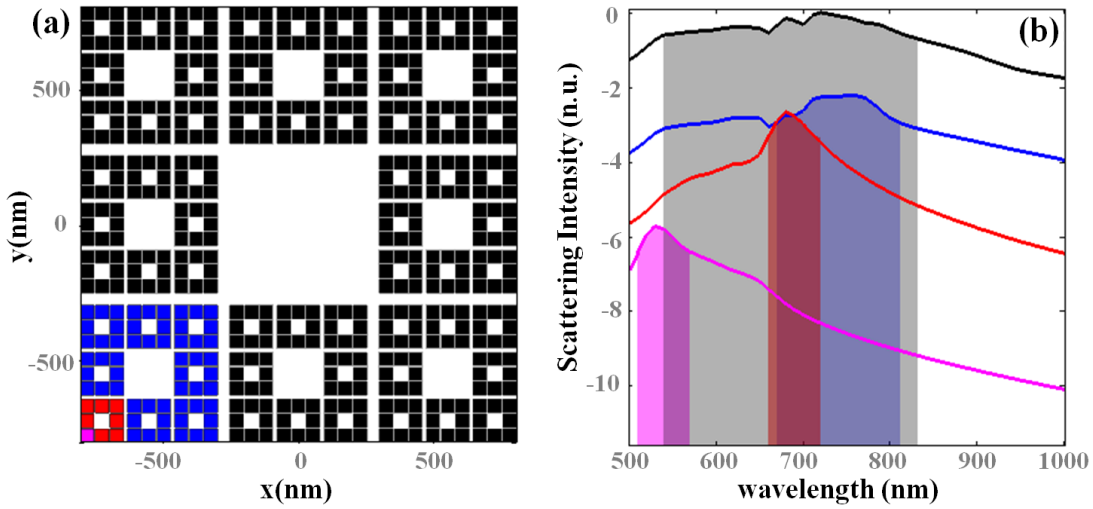

Figure 2.3: Broadening of the resonance in a plasmonic Sierpinski nanocarpet. (a) *First three fractal orders of the nanostructure, respectively in red, blue and black, and* (b) *relative far-field scattering spectra upon plane-wave excitation polarized along the x-axis. In pink, far-field spectrum of the basic building block of the fractal, a* $50x50x25\ nm^3$ *gold pad. For every spectrum, its FWHM is represented by the area of the same color. All the spectra are in a logarithmic scale and normalized to the volume of the gold of the respective substructures.*

For better comparison, the numerical values for the peak resonant wavelength and the FWHM of the different fractal orders are also reported in Table 2.1. Interestingly, while increasing the fractal complexity of the structure, the central wavelength of the resonance tends to red-shift. This is true at least up to the second fractal order, whose overall size is still comparable with the wavelength of light, thus allowing the near-field coupling of all the elements forming the different fractal levels.

Fractal Order	Zeroth	First	Second	Third
Peak Wavelength	532 *nm*	680 *nm*	760 *nm*	720 *nm*
FWHM	59 *nm*	56 *nm*	140 *nm*	295 *nm*

Table 2.1: Spectral properties of the plasmonic Sierpinski nanocarpet as a function of its fractal order. *Numerical values of the peak resonant wavelength and the FWHM of the spectra associated to the zeroth, first, second, and third fractal order of the Sierpinski*

nanocarpet (cf. Figure 2.3): w*hile increasing the complexity of the fractal structure, the wavelength of the resonance tends to red-shift and the spectrum to broaden.*

Finally, as for standard plasmonic nanostructures, the spectral properties of the Sierpinski nanocarpet can also be tuned as a function of the size of its fundamental building block. Table 2.2, for examples, reports the peak resonant wavelength and the FWHM for the zeroth, first, and second fractal order of a Sierpinski nanocarpet based on three different size of its fundamental building block: on the one hand, keeping this size constant, the peak wavelength of the resonance tends to red-shift and the spectrum to broaden, while increasing the complexity of the fractal structure; on the other hand, keeping the fractal order constant, the peak wavelength tends to red-shift when increasing the size of the fundamental building block.

Order \ *Size*	$40x40x20\ nm^3$	$50x50x25\ nm^3$	$60x60x30\ nm^3$
Zeroth	$\lambda = 530\ nm$	$\lambda = 532\ nm$	$\lambda = 536\ nm$
	$FWHM = 58\ nm$	$FWHM = 59\ nm$	$FWHM = 63\ nm$
First	$\lambda = 660\ nm$	$\lambda = 680\ nm$	$\lambda = 712\ nm$
	$FWHM = 65\ nm$	$FWHM = 56\ nm$	$FWHM = 103\ nm$
Second	$\lambda = 686\ nm$	$\lambda = 760\ nm$	$\lambda = 872\ nm$
	$FWHM = 71\ nm$	$FWHM = 140\ nm$	$FWHM = 191\ nm$

Table 2.2: Spectral tunability of the plasmonic Sierpinski nanocarpet. *For a constant size of the fundamental building block, the peak wavelength of the resonance tends to red-shift and the spectrum to broaden, while increasing the complexity of the fractal structure; for a constant fractal order instead, the peak wavelength tends to red-shift, when increasing the size of the fundamental building block.*

2.2.2 Subdiffraction focusing

Beyond broadband operation, the Sierpinski nanocarpet is also capable of focusing light beyond the diffraction limit, as shown in Figure 2.4, and might, therefore, prove beneficial for applications that require a tight light spot, such as subdiffraction imaging. Alternatively, subdiffraction focusing can be achieved by employing left-handed metamaterials [Grbic & Eleftheriades (2004)]; however, such technologies are still challenging at optical frequencies because of the diminished magnetic permeability of metals in this regime of frequencies [Fang *et al.* (2005)].

Figure 2.4 (a) shows the intensity of the electric near-field associated to the second fractal level of the structure of Figure 2.3 (a) (in blue) illuminated at its resonance, namely $\lambda = 760\,nm$. The evanescent waves induced by the gold nanopads interfere constructively at the center of the fractal and induce a subdiffraction focus, whose size is about $\lambda/8$; for comparison, the focus of a Gaussian beam (NA = 1.25, $\lambda = 760\,nm$) is plotted in Figure 2.4 (b) [Leutenegger *et al.* (2006)].

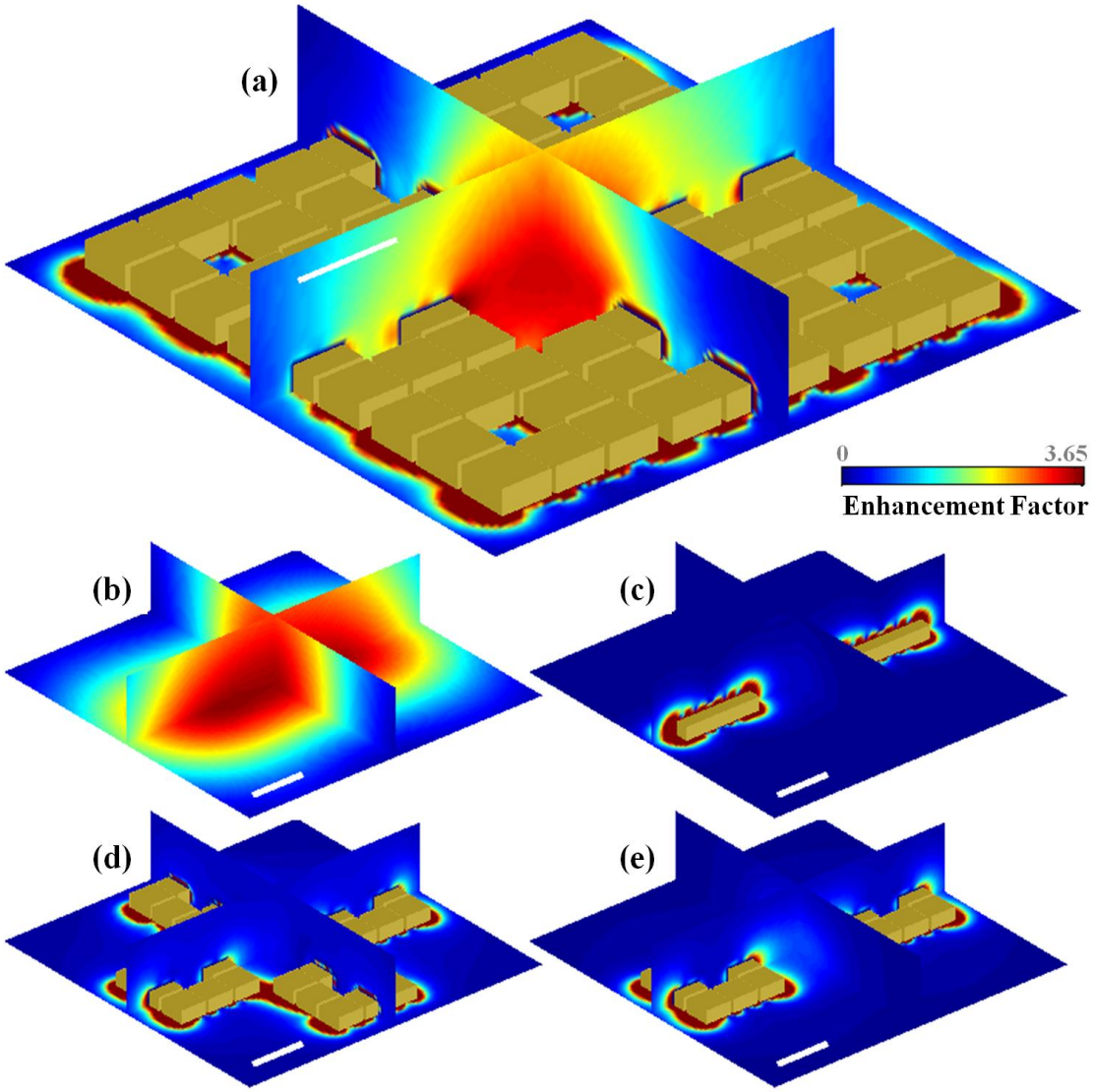

Figure 2.4: Subdiffraction focusing by a plasmonic Sierpinski nanocarpet. (a) *Normalized intensity of the electric near-field generated by the second fractal level of the Sierpinski nanocarpet (blue structure in Figure 2.3 (a)) upon plane-wave illumination at* $760\,nm$. (b) *Intensity at the focus of a Gaussian beam (*$NA = 1.25$, $\lambda = 760\,nm$ *).* (c) *Normalized intensity in a gap antenna geometry with the same separation as the open region in the fractal geometry.* (d-e) *Normalized intensities of the electric near-field of two symmetric non-fractal nanostructures obtained by removing elements from the structure in* (a). *The intensities presented in* (a), (c), (d) *and*

(e) *are normalized to the intensity of the incident field (enhancement factor). The intensity presented in* (b) *is given in arbitrary units on a different color scale. The white scale bar represents* $100\ nm$ *and is in the direction of the polarization of the incident field.*

Various plasmonic nanostructures have been employed to concentrate light into a subdiffraction spot, such as gap antennas [Mühlschlegel *et al.* (2005); Ghenuche *et al.* (2008)] or bow-tie nanoantennas [Schuck *et al.* (2005)]; however, such spot systematically lies in very close proximity to the metal. Interestingly, in the case of the Sierpinski nanocarpet the center of the focus is $\approx 80\ nm$ away from the metal surface and, due to the symmetry of the nanostructure, this result is nearly independent from the polarization of the incident plane wave. This provides an open region accessible to objects for enhanced light-matter interaction, which is not available in existing standard geometries. For example, gap antennas can focus light in the gap area between their two arms below the limit of diffraction [Mühlschlegel *et al.* (2005); Ghenuche *et al.* (2008)], but, if the two arms are separated by the same distance of the fractal case ($160\ nm$), there is no significant interaction between the two arms and consequently no hot spot is observed (Figure 2.4 (c)). Moreover, the formation of the hot spot in the gap is limited only to an incident illumination polarized along the longitudinal axis of the gap antenna.

The superfocusing properties of the plasmonic Sierpinski nanocarpet can be attributed to the fractal nature of the interference more than to the symmetry of the system: the evanescent waves generated at the metal surface constructively interfere at the center of the nanostructure, thus forming a focus. As counter tests, in Figure 2.4 (d) and (e), two different cases of symmetric non-fractal structures, obtained by removing elements from the Sierpinski carpet are presented. In both these cases, in fact, no high-intensity spot is formed at the center of the structure, far from the metal. In all these structures, however, because of the evanescent nature of the electric near-field, the highest field intensity is always at the metal surface. In the case of the plasmonic Sierpinski nanocarpet, this fact also determines the relatively poor value (3.65) of the enhancement factor obtained at the central focus, especially when compared to other geometries such as gap antennas [Ghenuche *et al.* (2008)].

2.2.3 Optical trapping potential

One possible use of the superfocusing properties of the Sierpinski nanocarpet is in optical trapping near surfaces. Even though optical forces arising from surface plasmons and plasmonic optical manipulation have already been demonstrated [Volpe *et al.* (2006); Righini *et al.* (2007); Righini *et al.* (2008)], some limitations arise because the trapping spots, which are near the maxima of the electromagnetic field intensity, are typically at the surface and in the proximity of the metallic nanostructures. However, it would be beneficial for many applications, such as single emitter manipulation, to have a subwavelength focus moved away from the surface and relatively far from the metallic nanostructures.

The focus produced by the plasmonic Sierpinski carpet (Figure 2.4 (a)) has these desirable features. The resulting optical forces [38] are shown in Figure 2.5 (a) for an incident power on the structure of $10^{12}\,W/m^2$ and a particle of $40\,nm$ ($\varepsilon_{particle} = 2.5$), which is notoriously difficult to trap with such low power. The equilibrium position of the force field is $\approx 15\,nm$ above the dielectric surface of the substrate. The resulting optical potential well (black line in Figure 2.5 (b)) is several times deeper than the thermal energy k_BT, allowing for a stable trapping. Also the potentials corresponding to a $30\,nm$ (red) and a $25\,nm$ (blue) are deep enough to allow at least a metastable trapping.

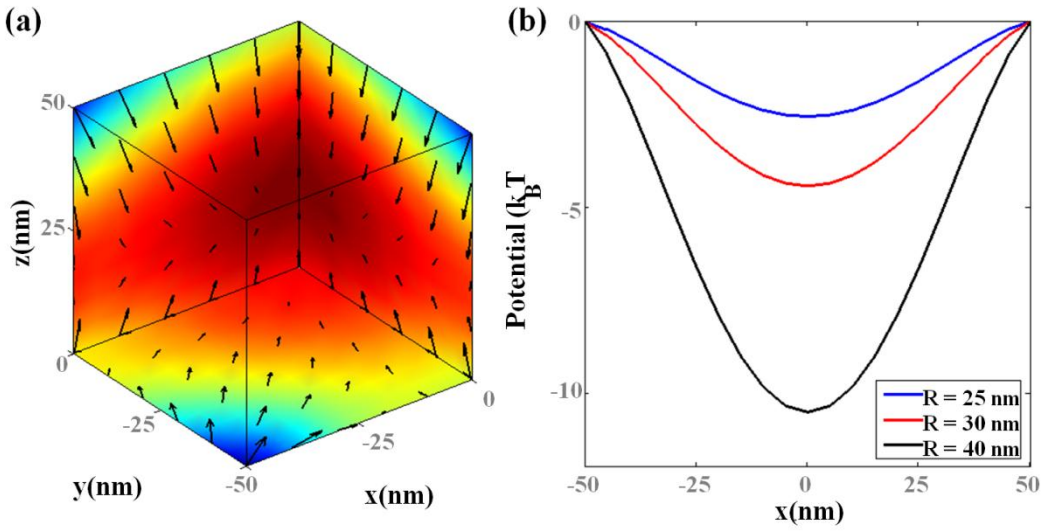

Figure 2.5: Trapping forces in the subwavelength focus at the center of the Sierpinski nanocarpet (see Figure 2.4 (a)). (a) *3D distribution of the force field and* (b) *trapping potential for particles ($\varepsilon_{particle} = 2.5$) of different radii R.*

Chapter 3

Unidirectional Optical Yagi-Uda Antennas

Optical antennas, acting as converters between propagating and localized fields, provide an effective route to couple photons in and out of nanoscale objects. As seen in Section 1.2.4, these antennas, that operate in the visible regime, are the counterparts of conventional radio- and micro-wave antennas [Balanis (2005); Bharadwaj *et al.* (2009); Novotny & van Hulst (2011)].

A characteristic of antennas is their directed emission and reception. So far, in the optical regime, the control of directionality has mainly been pursued by photonic crystal structures [Kramper *et al.* (2004)] and surface-plasmon–based devices [Lezec *et al.* (2002); López-Tejeira *et al.* (2007); Yu *et al.* (2008)]. However, for such structures approaching the nanometer scale, diffraction can limit the collimated beaming of light. On the other hand, the interaction of quantum emitters with light is best enhanced with micro-cavities [Pelton *et al.* (2002); Badolato *et al.* (2005)]. Compared with these approaches, plasmonic nanoantennas offer a much smaller footprint in an open geometry combining strong subwavelength fields and increased transition rates, together with the prospect of directionality. Earlier work observed variations in the angular emission of molecules by the presence of metallic objects in their near field [Gersen *et al.* (2000); Taminiau *et al.* (2008): Kühn *et al.* (2008)]. From experience at radio and microwave frequencies, it is known that highly directed beams are commonly obtained with Yagi-Uda antennas [Yagi (1928)]. In the optical regime, directional far-field scattering of a polarized laser beam from an array of Yagi-Uda antennas has been recently presented [Kosako *et al.* (2010)]. Complete control of the direction of light emission from a single quantum emitter using an optical Yagi-Uda antenna has been theoretically proposed [Hofmann *et al.* (2007); Li *et al.* (2007); Taminiau *et al.* (2008)].

This chapter reports the realization and observation of unidirectional nanoscale photon sources by coupling single-quantum systems to a Yagi-Uda design [Curto *et al.* (2010)]. The realization of such a source requires the precise near-field coupling of an emitter to a nanoscale antenna that is tuned to the emitter's emission spectrum. Within this framework, a novel fabrication protocol was, therefore, developed in order to place a quantum dot at the resonant feed element of a nanofabricated Yagi-Uda antenna. The surface chemistry protocol was developed with the help of Mark P. Kreuzer, while the presented numerical simulations and optical experiments were respectively carried out by Tim H. Taminiau and Alberto G. Curto in the group of Niek F. van Hulst at ICFO.

3.1 Nanofabrication Process

Feeding energy into an optical antenna is a task that can be accomplished from the far-field or, like in this work, from the near-field by coupling to a local optical emitter, such as a quantum dot. This second option allows one to excite the nanostructure at a designated position rather than driving the whole antenna simultaneously. In order to obtain a strong near-field coupling of the quantum dot to the antenna mode, it is critical to accurately place the emitter at a position of high electromagnetic mode density – that is, for a Yagi-Uda antenna, at the extremities of the feed element, being the latter a dipole antenna. Positioning a single emitter with respect to a nanostructure with a few

tens of nanometers of accuracy, however, constitutes a formidable nanotechnology challenge.

With this goal in mind, this section introduces a novel nanofabrication protocol for the accurate positioning of semiconductor quantum dots on gold nanoantennas by means of a two-step electron beam lithography process combined with surface chemistry: the first lithography step defines the antenna structures on a glass substrate, while the second step sets the boundaries for the formation of a self-assembled monolayer of intermediate linkers exclusively on the exposed areas; core-shell quantum dots are finally immobilized on these functionalized areas.

Previous approaches to similar positioning problems were mainly relying on spin-casting quantum dots solutions over the nanostructures of interest [Falk *et al.* (2009)]. Only a few approaches tried to achieve a more deterministic protocol, for example, by exploiting optical tweezers [Jauffred *et al.* (2008)] or more sophisticated forms of feedback control [Ropp *et al.* (2010)].

3.1.1 Design of an optical Yagi-Uda antenna

A Yagi-Uda antenna consists of an actively driven dipole ($\lambda/2$) feed element surrounded by a set of parasitic elements acting as reflectors and directors. The reflectors and directors are detuned in length with respect to the dipolar resonance of the feed, and the spacing between elements is chosen so that a traveling wave pointing toward the directors is created [Yagi (1928)]. Figure 3.1 (a) illustrates the typical geometry of a radiofrequency Yagi-Uda antenna: a high directivity can be obtained with distances of about $a_r = 0.25\lambda$ between the feed and the reflector and about $a_d = 0.3\lambda$ between the feed and the director and between the directors [Balanis (2005)].

Rescaling this design down to optical frequencies raises some challenges mainly because, in this frequency range, metals behave as strongly coupled plasma rather than as perfect conductors [Section 1.2.4]. Numerical simulations were, therefore used to design five-element gold Yagi-Uda antennas for operation wavelengths of $\sim 800\,nm$. Further detail about the simulations can be found in [Taminiau *et al.* (2008); Curto *et al.* (2011)]. As explained in Appendix C, the nanofabrication of the antennas was then performed by e-beam lithography on PPMA followed by thin-film deposition ($30\,nm$ of gold) and lift-off. An optimal fabricated antenna is shown in Figure 3.1 (b) with feed length $L_f = 145\,nm$, spacing $a_r = 175\,nm$ between reflector and feed, and spacing $a_d = 200\,nm$ between directors. The total length is $830\,nm$, which is approximately one emission wavelength. The complete set of parameters (YU145) is reported in Table 3.1 together with the design parameters of other, slightly detuned, optical Yagi-Uda antennas.

	YU110	*YU125*	*YU145*	*YU160*
$L_f(nm)$	110	125	145	160

$L_d(nm)$	100	115	130	140
$L_r(nm)$	160	155	175	195
$w(nm)$	55	60	60	70
$a_d(nm)$	180	180	200	195
$a_r(nm)$	150	150	175	180
$L_{total}(nm)$	750	760	830	835

Table 3.1: Parameters sets of nanofabricated optical Yagi-Uda antennas as measured by Scanning Electron Microscopy. *L_f is the length of the feed element, L_d the length of the three directors, L_r the length of the reflector, w the width of the elements, a_r the separation between the centers of the reflector and the feed, a_d the separation between the centers of the feed element and the first director, and the spacing between directors. The thickness of the elements is 30 nm for all antennas. L_{total} is the total length of the Yai-Uda antenna.*

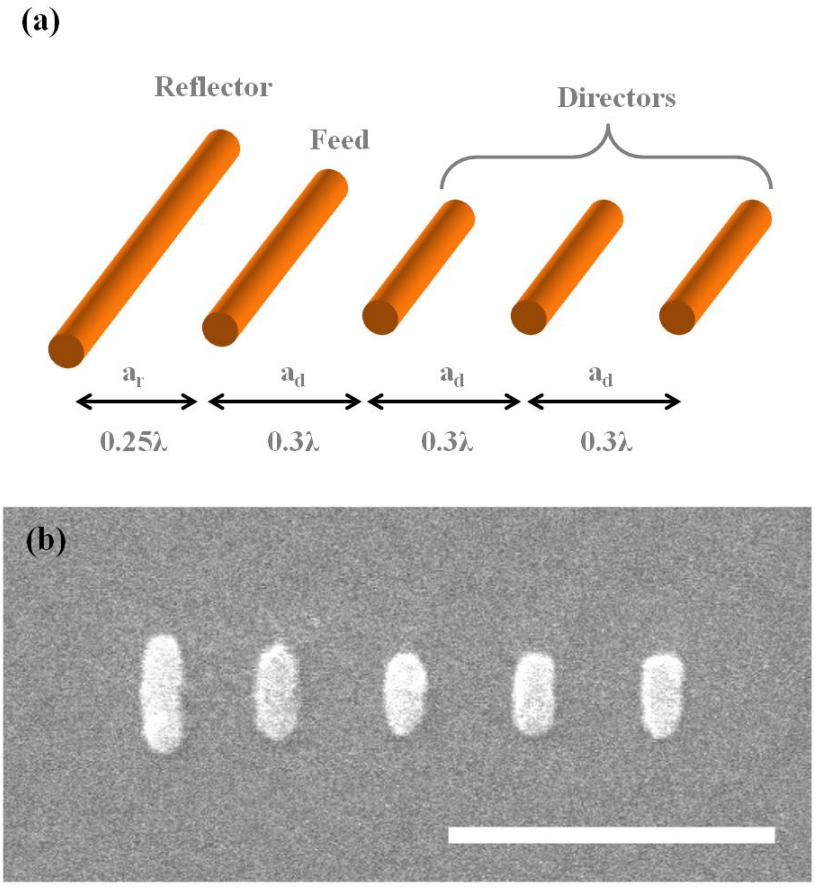

Figure 3.1: An optical Yagi-Uda antenna. (a) *Typical geometry of a five-element radiofrequency Yagi-Uda antenna.* (b) *SEM image of nanofabricated five-element Yagi-Uda antenna consisting of a feed element, one reflector, and three directors (YU145 in Table 3.1). The white scale bar corresponds to* $500\ nm$.

3.1.1 Positioning of single emitters on nanoantennas

The next steps of the fabrication process aim to precisely place single quantum dots at one end of the feed element of the Yagi-Uda antennas, where coupling to the antenna mode is most efficient. In order to achieve this goal, the developed protocol involves a second lithography step, together with a selective chemical functionalization of predefined areas. This process is schematically represented in Figure 3.2 (a-f), and it is described hereafter.

The used emitters are core-shell (CdSeTe/ZnS) quantum dots with a polymer coating (Invitrogen, Qdot 800 ITK). They are around $10\ nm$ in size, and are functionalized with amine-polyethylene glycol (amine-PEG) which can be used as a chemical linker (amine group ($-NH_2$)). Their emission wavelength is centered at $800\ nm$ with a quite broad absorption spectrum below $750\ nm$. They are commercially prepared in a $8\ \mu M$ solution, but they need to be further diluted to one part in eighty with phosphate buffered saline (PBS): this is a suitable enough concentration to avoid clusterization and to guarantee the formation of a homogeneous monolayer of quantum dots on gold.

Before chemically functionalizing the antennas, a 30-nm-thick PMMA layer is spin-coated over the substrate to serve as a positive resist also for the second lithography step. While the first lithography defines the antenna structures on the substrate, the second lithography sets the boundaries for the formation of a self-assembled monolayer of mercapto-undecanoic acid (MUA) exclusively in the predefined PMMA gaps: on one side, these molecules end with a thiol group ($-SH$) offering a selective binding site to the gold nanoantennas; on the opposite side, however, the molecules end with a carboxylic group ($-COOH$), thus offering a free binding site for the complementary amine groups of the quantum dots (Figure 3.2 (g)) [Love *et al.* (2005)].

After activation with Ethyl-3-(3-dimethylaminipropynol)-carbodiimide (EDC), quantum dots are covalently bound to the MUA functionalized region, and the remaining resist with the unselectively bound quantum dots is removed by a standard lift-off protocol in acetone.

Because of the MUA layer and the polymer coating of the quantum dots, the estimated distance between the outer surface of the quantum dot shell and the metal is around $6\ nm$, sufficient to avoid luminescence quenching and to provide efficient coupling to the underlying antenna.

Of course, for this protocol to work, a critical step is the accurate alignment, within a few nanometers, between the first and the second lithography: for this purpose, three gold alignment marks (size $1\mu m\ x\ 1\mu m$) are fabricated around the nanoantennas during the first lithography step (Figure 3.2 (a)). Figure 3.2 (h), for example, shows the

accuracy in the positioning of a 50-nm titanium dot at different locations with respect to a gold nanorod.

Finally, by controlling the size of the PMMA gaps of the second exposure, the number of single emitters deposited inside can also be tuned down to individual quantum dots.

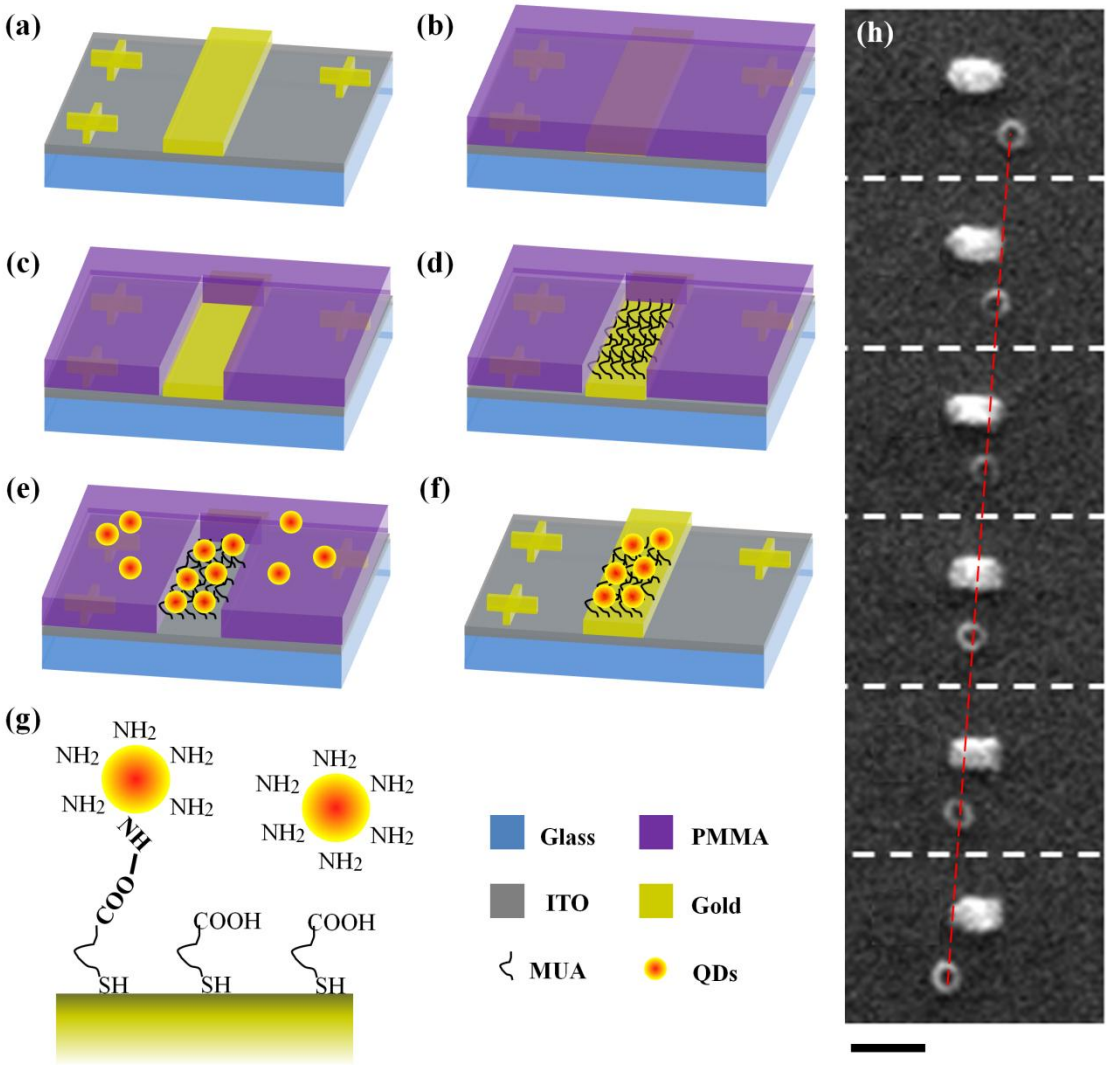

Figure 3.2: Schematic of the quantum dot nanopositioning protocol. (a) *The first lithography step defines the gold nanostructures and the alignment marks around them;* (b) *a 30-nm-thick film of PMMA is spin-coated over the sample;* (c) *the resist is then patterned by exposure to an electron beam and developed;* (d) *a self-assembled monolayer of MUA is formed on gold;* (e) *quantum dots are covalently bound to the MUA functionalized areas;* (f) *the remaining resist with the unselectively bound quantum dots is removed by a standard lift-off in acetone.* (g) *Chemical functionalization of the gold surface: the MUA layer offers selective binding sites both to gold and the polymer-coated quantum dots.* (h) *A 50-nm titanium dot (second lithography) is moved along a nanorod (first lithography) with 15-nm steps. The black scale bar represents* 100 *nm.*

3.2 Optical Characterization

Having fabricated the sample as described in the previous section, the emission of the quantum dots on the nanoantennas was then characterized with a confocal microscope with three dedicated detection branches: for luminescence imaging in direct space, angular detection, and spectroscopy, respectively.

The use of a high–numerical aperture (NA) oil immersion objective (Zeiss, α Plan-Apochromat 100x/1.46 NA) is essential for the angular detection. The sample is excited by a circularly polarized He-Ne laser beam ($\lambda = 633\ nm$) with a power on the order of some microwatts after reflection on a dichroic mirror (Semrock, 665LP). The laser is focused to address a single antenna at a time. The resulting luminescence is further separated from the excitation wavelength with a long-pass filter (Omega, 690 LP). For confocal detection, the use of a polarizing beam-splitter and two detection channels ($I_{\parallel}$ and $I_{\perp}$) with avalanche photodiodes (Perkin Elmer, SPCM-AQR-14 and 16) allows one to determine polarization anisotropies.

For the detection of the angular emission, an electron-multiplying charge-coupled device (EMCCD) camera (Andor, iXon^{EM}+ 897) was used to record images of the intensity distribution on the back focal plane of the high-NA objective – conoscopy [Lieb *et al.* (2004)]. These Fourier-space images (momentum space) contain the directions of emission toward the substrate. The angular radiation patter is related to the intensity and coordinates of the back-focal plane of the objective by the following relation (Figure 3.3 (a)):

$$I(\theta, \varphi) = I\big(k_x, k_y\big)cos(\theta), \tag{3.1}$$

where the cosine factor is an apodization factor, $k_x = KRsin(\theta)cos(\varphi)$ and $k_y = KRsin(\theta)sin(\varphi)$, being R the radius in pixels of a given point in the image of the back focal plane and K a calibration constant related to the magnification of the imaging system that can be obtained by fitting to the diffraction orders of calibration diffraction gratings.

A different detection branch was used to image the luminescence of the quantum dots in direct space: all presented confocal luminescence images are color-coded (red-yellow-green) for the degree of linear polarization DOLP

$$DOLP = \big(I_{\parallel} - I_{\perp}\big)/\big(I_{\parallel} + I_{\perp}\big), \tag{3.2}$$

with red being linear polarization parallel to the feed longitudinal axis. All antenna-emitter systems in Figure 3.3 (b) show red (linearly polarized), confirming that the quantum dot drives the linear dipole of the feed element [Taminiau *et al.* (2008); Shegai *et al.* (2008)]. The emission arises from quantum emitters as discrete blinking events interrupt the signal during raster-scanning of the sample. This blinking is better seen in the luminescence time trace displayed in Figure 3.3 (c), in which clear on and off states

can be identified, which is characteristic of a single emitter. These time traces point out that single quantum dots occur frequently, whereas the typical number of quantum dots observed is one, two, or three – a number that can be controlled by both the size of the functionalized area and the concentration of the deposited solution of quantum dots.

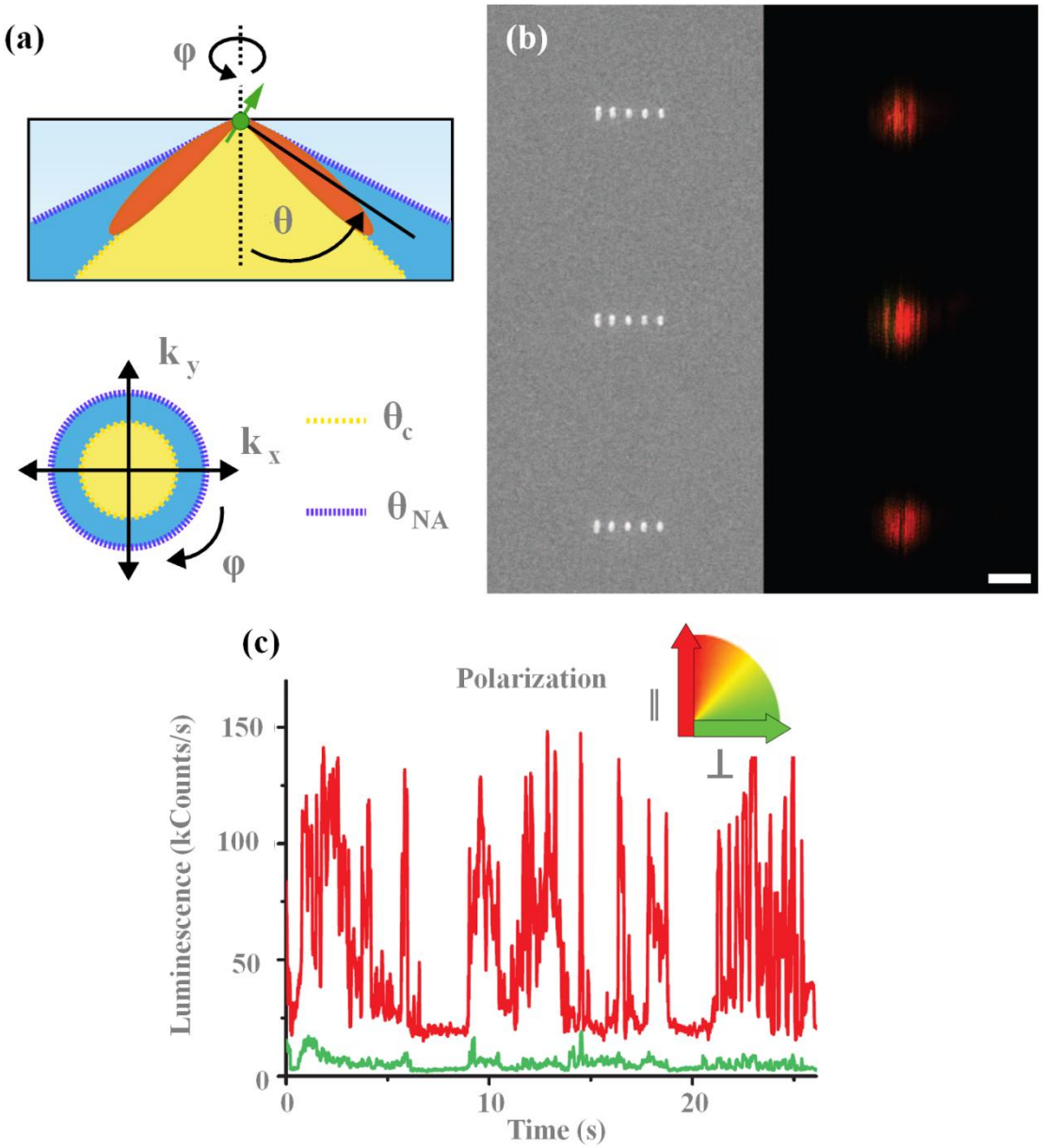

Figure 3.3: Detection of optical Yagi-Uda antennas driven by quantum dots. (a) *Radiation pattern of a dipole close to a dielectric interface and explanation of conoscopy highlighting the critical and numerical aperture angles.* (b) *Comparison of SEM and scanning confocal luminescence microscopy images of three antennas driven by quantum dots. The image is color-coded for degree of linear polarization. The scale bar represents* 500 *nm.* (c) *Intensity time trace of luminescence in both polarization channels for one of the antennas in* (b)*, showing blinking of a single quantum dot.*

3.2.1 Comparison with non-unidirectional antennas

To gain direct insight into the changes in the quantum dot emission upon coupling to the antenna, three types of nanostructures are compared (Figure 3.4 (a) and (b)): small 60-nm gold squares, $\lambda/2$ dipole antennas, and the Yagi-Uda antennas. The small, off-resonant squares were taken as a reference for quantum dots on metal; the dipole antennas are essentially the feed element of a Yagi-Uda antenna. In the reference case, the polarization of the luminescence varies, with a DOLP ranging from -0.5 to 0.5 (Figure 3.4 (a), first column) because the quantum dots have different orientations and the gold squares induce no preferential direction. The corresponding emission pattern is shown in Figure 3.4 (b). The momentum space images contain two distinct circles in the polar angle θ: the outer circle is the maximum collection angle of our objective ($\theta_{NA} = 72.8°$), whereas the inner circle is the critical angle for the glass-air interface ($\theta_c = 41.1°$). A dipole close to an interface emits primarily into the high-index medium, with sharply peaked maxima at the critical angle (Figure 3.3 (a)). Moreover, the quantum dots used here exhibit a degenerate transition dipole moment contained on a *bright* plane [Koberling *et al.* (2003); Brokmann *et al.* (2005)]. As a result, the radiation pattern of one of these quantum dots is nearly isotropic in the azimuthal angle φ.

When coupled to a $\lambda/2$ dipole resonant nanoantenna (Figure 3.4, second column), the picture changes dramatically: the quantum dot luminescence turns into a clear linear polarization parallel to the long axis of the antenna ($DOLP \approx 0.8$), and the radiation pattern transforms to that of a linear dipole close to an interface [Lieb *et al.* (2004)]. These are two clear signatures of the near-field coupling [Taminiau *et al.* (2008)]. The emission of the quantum dot becomes fully determined by the antenna mode, both in polarization and direction, despite the degeneracy of the quantum dot dipole moment.

Finally, if the quantum dot is positioned at one end of the $\lambda/2$ feed element of Yagi-Uda antennas (Figure 3.4, third column), the luminescence remains strongly linearly polarized ($DOLP \approx 0.8$), but the radiation pattern now shows a single lobe, demonstrating the unidirectional emission of a quantum dot due to coupling to an optical antenna.

The directional performance can be quantified by a front-to-back ratio (F/B), defined as the intensity ratio between the point with maximum emitted power and the point diametrically opposite in the radiation pattern. The F/B value is essentially $0\ dB$ for the reference squares and the dipole antennas, as expected for symmetrical structures. For the Yagi-Uda antenna in Figure 3.4 (b), F/B is $6\ dB$. The directed emission is centered at $\theta = 49.4°$, with a beam half width at half maximum of $12.5°$ in θ and $37°$ in φ. The experimental angular radiation pattern can be calculated from the Fourier-plane image according to Equation (3.1) and agrees well with the theoretical prediction (Figure 3.4 (c)). The simulations quantify that as much as 83.2% of the quantum dot emission is directed into the high-index glass substrate. The emission is thus truly unidirectional, unlike configurations with a low-index contrast interface, which results in two separate emission lobes [Kosako *et al.* (2010)]. The total brightness of the quantum dots coupled to Yagi-Uda antennas is comparable with that of dipole

antennas. This observation is in agreement with previous calculations and theoretical predictions [Taminiau *et al.* (2008)], which show that adding the parasitic antenna elements does not strongly reduce the antenna radiation efficiency (only a 10% to 20% reduction). The Yagi-Uda antenna redirects the emission instead of suppressing one half of the radiation. Because of excitation enhancement, the number of counts detected from both types of antennas is much higher than for a quantum dot on glass without coupling to an antenna.

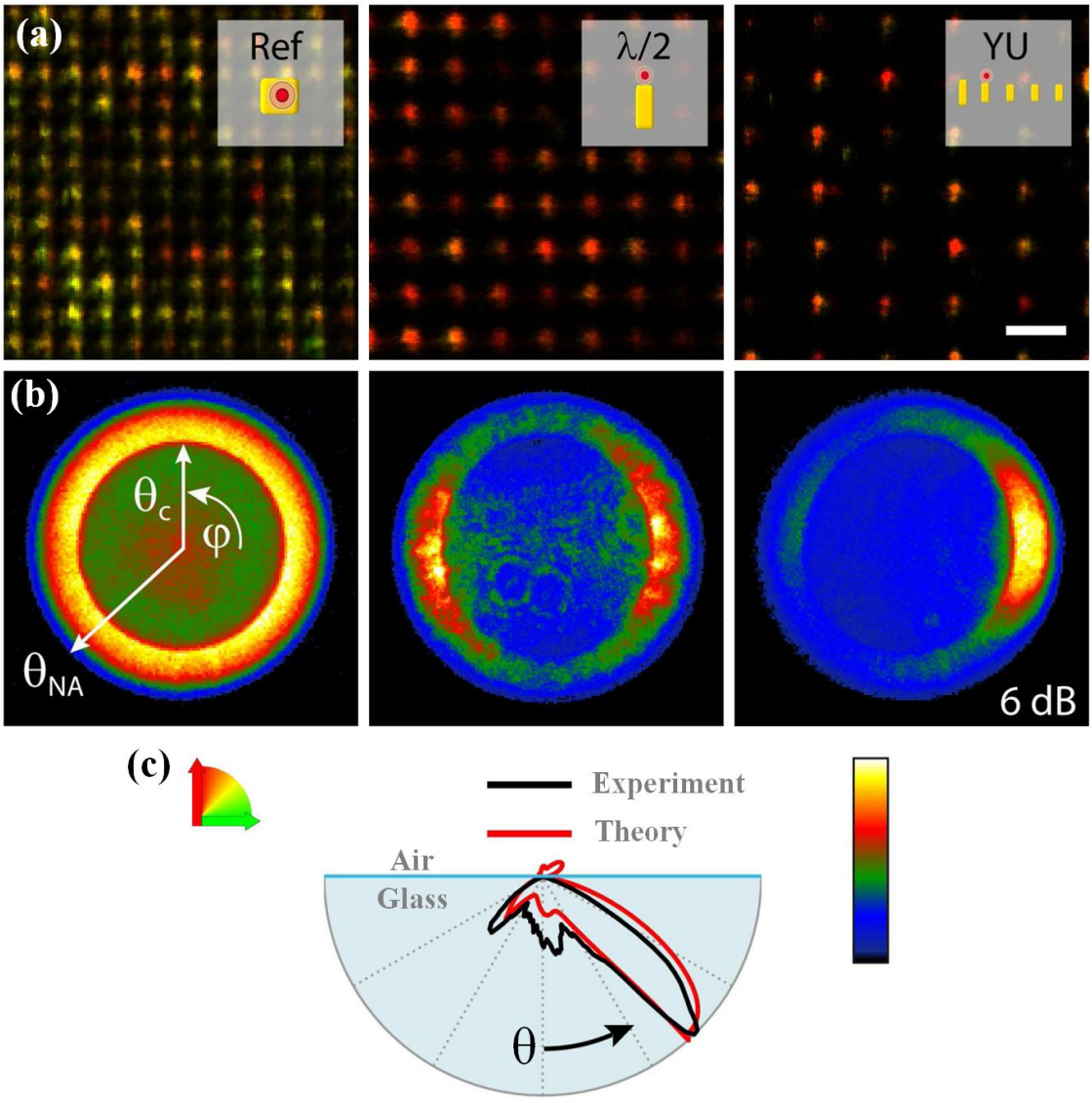

Figure 3.4: Unidirectional emission of a quantum dot coupled to an optical Yagi-Uda antenna. (a) *Scanning confocal luminescence images of quantum dots on reference 60-nm gold squares (Ref), half-wave dipole antennas ($\lambda/2$), and Yagi-Uda antennas (YU), respectively. Different colors show variations in the degree of linear polarization. YU corresponds to antennas with the parameters set YU145 in Table 3.1. The schematics in the insets are not to scale. The white scale bar represents* 2 μm. (b) *Radiation pattern (intensity distribution at the back focal plane of the objective) from an individual structure in* (a). *Critical (θ_c) and numerical aperture (θ_{NA}) angles are indicated. For*

YU, an 830-nm long-pass filter was used. (c) *Angular radiation patter in the polar angle (θ) for the experimental Yagi-Uda antenna (black), which is in good agreement with the theoretical prediction (red).*

The presented antenna, therefore, transforms the non-directional quantum dot luminescence into a directed light source that can be efficiently collected, simply with a low NA. Further optimization of the many Yagi-Uda design parameters, including the addition of more director elements, might sharpen up the unidirectional cone and tune the central emission angle. The operation bandwidth can be increased by the use of a log-periodic design [Balanis (2005)]. By reciprocity, the antennas should work both in emission and absorption. The near-field coupling to the antenna plasmon resonance enhances radiative transition rates, increasing the emission efficiency. All this control over photon emission is obtained from an antenna that is only a single wavelength long. Unidirectional optical antennas thus provide a route to effectively communicate light to, from, and between nano-emitters, for example in directed, bright single-photon sources for quantum optical technologies, planar biochemical sensors, and light-harvesting and emission devices.

3.2.2 Tuning of optical Yagi-Uda antennas

Any Yagi-Uda antenna is designed to operate at a certain frequency and bandwidth. To assess the frequency dependence of the directionality, Yagi-Uda antennas tuned to four different resonant frequencies were fabricated (Figure 3.5 (a)), identified with their feed element lengths L_f: 110 to 160 nm (a complete parameter set can be found in Table 3.1). Increasing the antenna length creates a red-shift of the resonance. The shortest antennas (YU110 and YU125) emit clearly unidirectionally. These antennas are tuned close to the quantum dot emission, and their bandwidth contains the complete luminescence spectrum. These observations are in agreement with a calculated bandwidth of 150 nm for end-fire operation, defined as $F/B > 3\,dB$. On the other hand, for longer antennas (YU145 and YU160) the antenna resonance is more detuned from the quantum dot emission, and directivity is hindered by short-wavelength components of the spectrum. This spectral dependence does also occur for radio frequency Yagi-Uda antennas [Takla & Shen (1977)] and was in fact predicted for the optical regime [Hofmann *et al.* (2007); Koenderink *et al.* (2009)].

To corroborate the analysis above, the dependence of the directionality on the wavelength of the emitted photons for a given antenna was also evaluated, YU145 (Figure 3.5 (b) and (c)). This antenna was red-detuned from the quantum dot emission. As a result, the quantum dot emission spectrum was modified by the near-field coupling to the antenna (Figure 3.5 (c)) [Ringler *et al.* (2008)]. The emission spectrum of an individual quantum dot coupled to a YU145 antenna was divided in three parts by using three different filters. Although hardly any directed emission was observed for the complete spectrum (Figure 3.5 (a)), a high directivity was recovered when only the long-wavelength part of the spectrum was selected (Figure 3.5 (b)). For short

wavelengths – below a cut-off value –the emission was even reversed, with the main lobe pointing backward. Similar behavior was observed for the longer antenna YU160, with all characteristic wavelengths shifted to longer wavelengths. The numerically calculated back-focal-plane images agree well with the experimental results (Figure 3.5 (b)). The maximum experimental F/B values tend to be lower than the theoretical values because part of the signal stems from autoluminescence of the gold nanoparticles and a fraction of the quantum dot emission is not coupled to the antenna, both of which contribute to a minor isotropic background. Thus, by tuning the antenna or selecting certain emission bands the frequency dependence of the directivity of an optical Yagi-Uda antenna is proved.

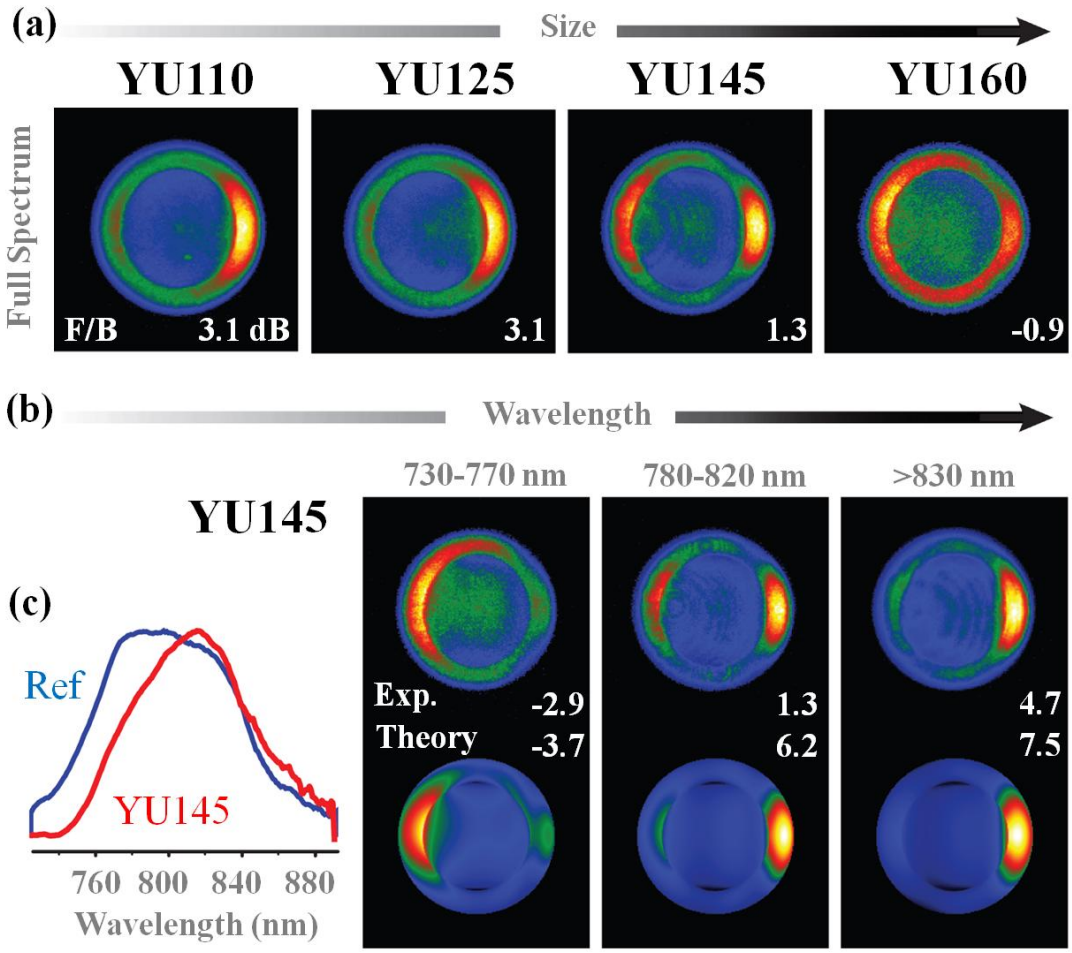

Figure 3.5: Tuning of optical Yagi-Uda antennas. (a) *Radiation patters in the back focal plane of the objective for four different individual Yagi-Uda antennas of increasing overall size, characterized by the length of the feed element* lengths L_f *from* 110 *to* 160 *nm. The full emission spectrum is recorded.* (b) *Angular radiation patterns for different spectral detection windows for the YU145 shown in* (a). *Theory and experiment are compared. The front-to-back ration in decibels is indicated for each pattern.* (c) *Luminescence spectra of quantum dots coupled to the reference and YU145.*

Chapter 4

Influence of Spatial Phase Shaping on Nanoantennas

As seen in the previous two chapters, tailoring the shape and the dimensions of metal nanoparticles is a fundamental ingredient in order to tune plasmonic resonances and to control light fields on the nanoscale: plasmonic nanostructures, in particular, have been designed to confine light in truly subwavelength volumes opening new opportunities to enhance the interaction of light with small quantities of matter down to the molecular level [Section 1.3].

Beyond confining light at fixed locations, imposed by the structure geometry, there is, however, a need for dynamic spatial control of such *hot-spots*, for instance in order to selectively address optically different nearby nano-objects.

Section 1.4 reviewed several strategies borrowed from the field of coherent control that have recently been suggested to reach this goal: a first approach relies on temporally shaping the phase and amplitude of an ultra-short laser pulse illuminating the nanostructures [Stockman *et al.* (2002); Aeschlimann *et al.* (2007)]; control of the local optical response of a metal surface was also achieved by adjusting the temporal phase between two unshaped ultra-short pulses [Kubo *et al.* (2005)]; alternatively, the idea of time reversal has also been proposed lately [Li & Stockman (2008)].

This chapter proposes a novel approach, based on continuous light flows, that aims at achieving a deterministic control of plasmonic fields by using the spatial polarization inhomogeneities of high order beams, such as Hermite-Gaussian and Laguerre-Gaussian beams [Appendix C]. A prior study showed that azimuthally and radially polarized beams with different polarization singularities are transmitted through subwavelength apertures in metal film with different efficiencies [Kindler *et al.* (2007)]. Here, instead, the spatial phase shaping of the illumination field provides, in fact, an additional degree of freedom to drive nano-optical antennas and consequently control their near-field response. Furthermore, the potential of this approach to deterministically confine light at specific locations of a more complex metallic nanostructure is also demonstrated.

4.1 Gap Antennas: A Case Study

A coupled antenna, formed by two adjacent gold nanowires separated by a tiny air nanogap, is a good first test structure to demonstrate the concept proposed above. It is now well-known that driving the overall antenna with a field linearly polarized across the gap leads to a strong gradient of surface charges responsible for a dramatic enhancement of the field within the gap region (Figure 1.6). This study, however, focuses on a configuration where the polarization of the incident field is not constant over the whole antenna extension. In particular, the overall near-field response of the antenna is expected to be dramatically changed when driving out of phase each of the constitutive bars forming the structure.

Such illumination conditions, in particular, can be provided by higher-order light fields, such as Hermite-Gaussian or Laguerre-Gaussian beams [Appendix C]. These two families of optical fields form two different bases which can independently describe any paraxial beam [Siegman (1986)]. The Hermite-Gaussian functions are separable on the transverse Cartesian coordinates (x, y); they are labeled with two natural non-negative

integer indices, $HG_{nm}(x,y)$, corresponding to the number of π-phase jumps along the x and y direction, respectively [Appendix C.1]. The Laguerre-Gaussian modes have a cylindrical geometry and are also described with two discrete indices, $LG_{lp}(\rho,\varphi)$. In this case, the non-negative integer index p corresponds to the intensity nodes of the functions along the radial direction (with $\rho > 0$). The index l can take negative values and is proportional to the orbital angular momentum of the mode in the direction of propagation [Appendix C.2]. These two sets of modes can be directly linked with the non-paraxial multipole solutions of the Maxwell equations [Molina-Terriza (2008)]. In practice, any Hermite-Gaussian or Laguerre-Gaussian beam can be generated from a Gaussian beam by either using patterned phase masks or a spatial light modulator (SLM).

4.1.1 The hybridization model

The longitudinal resonance of a gap antenna can be understood in terms of hybridization of the longitudinal resonances of each of the individual antennas, resulting from the coupling over the narrow separation gap [Prodan *et al.* (2003); Nordlander *et al.* (2004)].

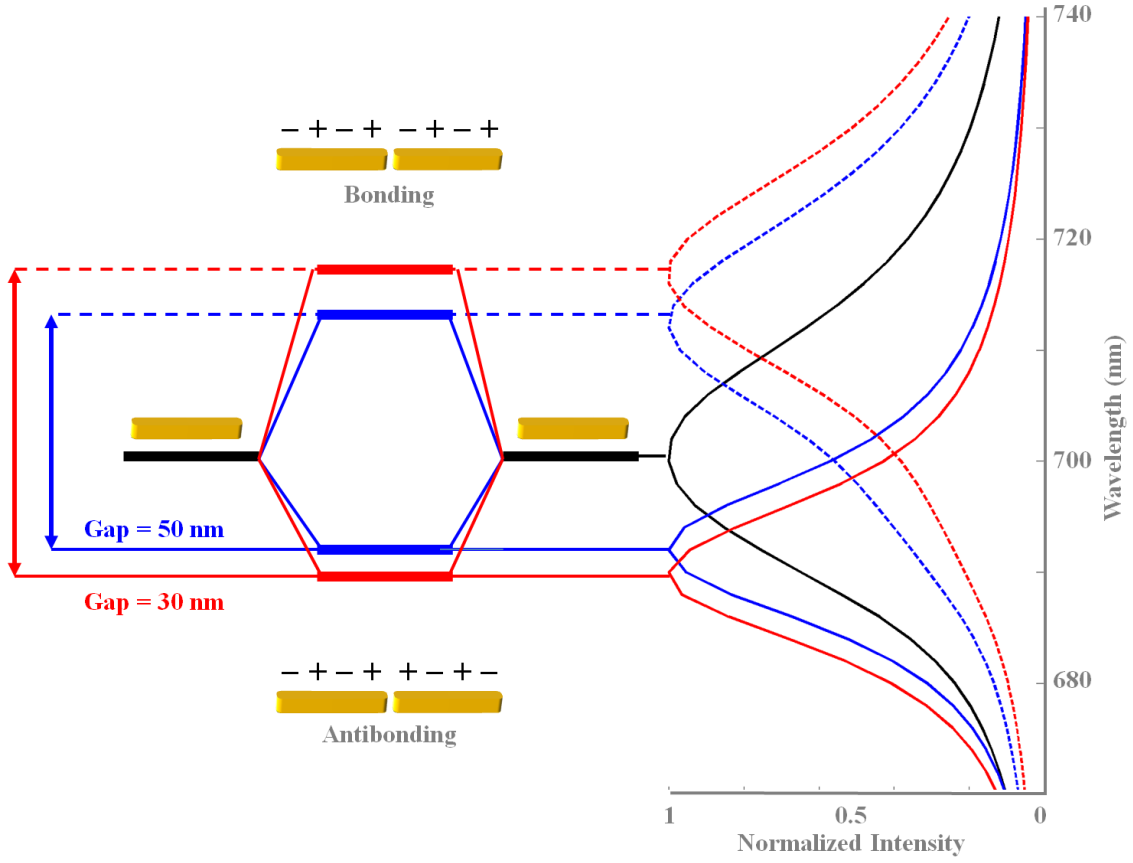

Figure 4.1: Energy splitting of the modes of a coupled gap antenna. *Energy-level diagram and simulated near-field intensity spectra of symmetric linear gold gap*

antennas formed by $500x100x40\ nm^3$ *arms with a 30-nm (red) and a 50-nm (blue) gap, as well as single rods with the same dimensions (black). The spectra of the bonding modes (dashed curves, red and blue) are obtained under plane wave illumination of the antenna, while the spectra of the antibonding modes (solid curves, red and blue) are obtained by driving each of the antenna arms out of phase with two independent plane-waves. All spectra are calculated* $5\ nm$ *away from the antenna ends.*

According to this model, the coupling between nanorods causes a mode splitting into a lower-energy *bonding mode* and a higher-energy *antibonding mode*, respectively. The simulated near-field spectral intensities in Figure 4.1 show this energy splitting for the $3\lambda/2$ mode of a $500x100x40\ nm^3$ gold nanorod (black continuous curve) lying on a glass substrate (ε_{gold} is taken from [Palik (1985)], $\varepsilon_{glass} = 2.3$ and $\varepsilon_{air} = 1$): driving the coupled antenna with a plane-wave linearly polarized across the gap induces a shift of the system resonance to longer wavelengths (*bonding mode*), while driving the two antenna arms separately with two out-of-phase plane-waves induces a shift of the resonance towards shorter wavelengths (*antibonding mode*). As sketched in the figure, the energy splitting of the modes increases with reduced gap size, revealing the distance dependence of the interparticle coupling [Section 1.3.2]: the red and blue curves represent the energy splitting for a 30-nm and a 50-nm gap, respectively.

In practice, even in presence of strong coupling, antibonding modes are usually not observed in white-light scattering experiments since their excitation is symmetry-forbidden under normal incidence with a plane wave [Funston *et al.* (2009); Slaughter *et al.* (2010)]. The antibonding antenna mode can, however, be excited if the symmetry of the system is broken either by the shape of the structure [Hao *et al.* (2008); Funston *et al.* (2009); Slaughter *et al.* (2010)] or, as in this study, by the illumination conditions.

4.1.2 Experimental setup

In order to evaluate the influence of high-order beams on the local response of optical antennas, mode mapping experiments were performed using two-photon-induced luminescence (TPL) microscopy, since it was previously shown that TPL mapping over a gold gap antenna provides direct information about its actual mode distribution [Ghenuche *et al.* (2008)]. Gap antennas formed by two adjacent ($500x100x40\ nm^3$) gold bars and separated by a $50\ nm$ air gap were fabricated on a ITO-coated glass substrate by combining e-beam lithography with liftoff [Appendix B]. The fabricated sample was mounted on a 3D piezoelectric scanner lying in the sample plane of an inverted optical microscope (Olympus IX71) equipped with a high-NA oil immersion objective (Olympus, Plan Achromat, 100x/1.25 NA). The expanded beam from a tunable fs-pulsed Ti:Saph laser ($\sim 150\ fs$ pulse width) operated at $750\ nm$ was sent on a removable phase mask and, after reflection on a dichroic mirror (Semrock, FF670), it was focused on the back-focal plane of the objective by means of a 2-meter-long focal-length lens. This optical configuration is schematically represented in Figure 4.2. By focusing the phase-shaped beam on the back-focal plane of the objective, it was

possible to generate an almost collimated incident beam ($\sim 2\ \mu m$ beam waist) that was commensurable with the whole antenna size.

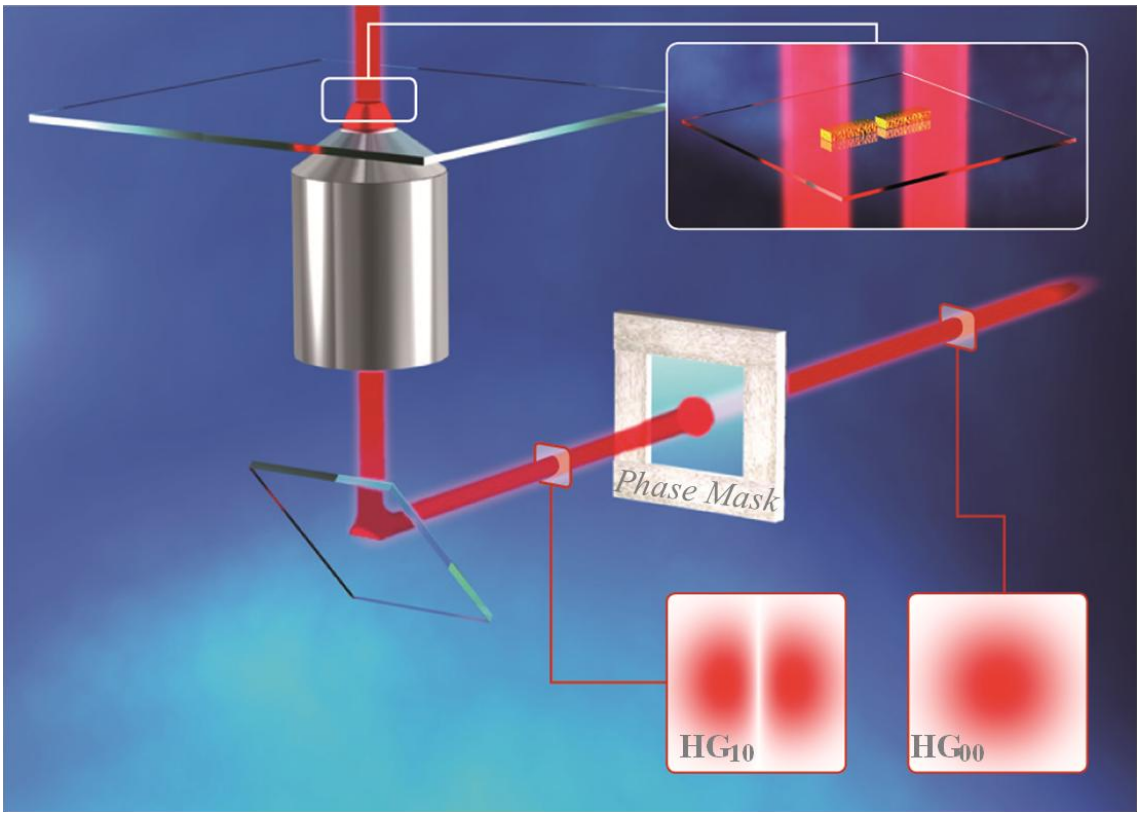

Figure 4.2: Schematic view of the optical excitation path of the setup. *The Gaussian beam generated by a tunable fs-pulsed laser is converted into a higher-order beam using a phase mask before being focused, after reflection on a dichroic mirror, on the back-focal plane of a high-NA oil immersion objective. At the sample, an almost collimated beam illuminates one antenna at the time (top inset).*

While accurate nano-positioning of the antennas with respect to the optical axis was done using the piezoelectric scanner, mapping the TPL at each point of the sample surface was performed by raster scanning the confocal detection volume using an automated steering mirror (Newport, FSM-300) and a band-pass filter (Thorlabs, FGB37) included in the detection path. The microscope tube-lens (focal length, $f_1 = 18\ cm$), together with other two lenses (focal lengths, $f_2 = f_3 = 15\ cm$) in the detection path, formed an image of the TPL signal onto an avalanche photodiode (SPCM-AQRH Single Photon Counting APD from Perkin Elmer), whose aperture a was set to 30 μm by means of a pinhole. The in-plane resolution is then given by

$$res = \frac{a}{M} = 300\ nm, \tag{4.1}$$

where the total magnification M is given as

$$M = M_{TL}\frac{f_3}{f_2}, \tag{4.2}$$

being $M_{TL} = 100$ the total magnification of the microscope's objective and tube lens.

4.1.3 Experimental TPL measurements

Figure 4.3 shows TPL maps recorded over a gap antenna illuminated by three different beams, all linearly polarized along the x-axis. The wavelength of the illumination beam was set at the resonance ($750\,nm$) of a single $500x100x40\,nm^3$ nanofabricated rod. At this wavelength, the coupling to both bonding and antibonding mode is still reasonably strong for the case of a 50-nm separation gap, as can be appreciated by the simulated spectra in Figure 4.1. The difference in resonant wavelength between fabricated and modeled structures is mainly due to differences in their shape and to the presence, in the real sample, of an additional thin layer of ITO [Appendix B], which notoriously induces a red-shift of the resonance [Section 1.2.3]. For reference, in Figure 4.3 (a-b), the case of a Gaussian beam (HG_{00}) without any phase mask is the first to be considered. The TPL distribution is dominated by emission maxima around the gap region. It is interesting to note that, despite the significant differences in the excitation/collection scheme used in [Ghenuche *et al.* (2008)], very similar maps were found.

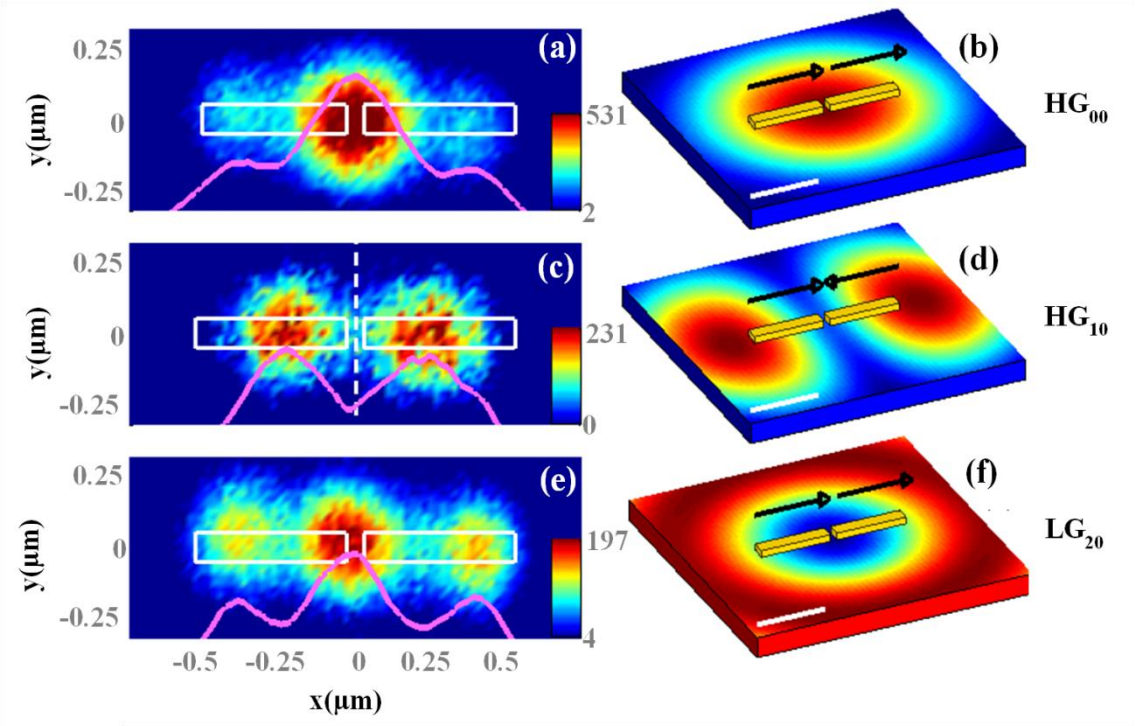

Figure 4.3: Experimental near field optical response of a gap antenna driven by higher-order beams. (a,c,e) *Experimental TPL maps recorded on a gap antenna (white rectangles) when driven by three different incident beams ($\lambda = 750\,nm$):* (a) HG_{00}

(Gaussian), (c) HG_{10} *and* (e) LG_{20}*. The color scale gives the TPL intensity in photon counts. In* (b)*, the vertical dashed line locates the* π*-shift position of the* HG_{10} *beam.* (b,d,f) *Associated computed intensity distribution of the incident field (scale bar, 500 nm). Each of the three beams is linearly polarized along the x-axis. The black arrows give the relative polarization orientation across the beam.*

A drastic change in the antenna near-field response was observed when switching the illumination from a Gaussian beam to a HG_{10} beam, whose phase jump coincides with the position of the antenna gap ($x = 0$). In particular, unlike the Gaussian case, the gap region now appears as an emission minimum (Figure 4.3 (c-d)). Such drastic inversion in the near-field contrast is attributed to the π-phase shift in the polarization of the field driving each of the two antenna arms. In fact, a first intuitive interpretation can be that, by driving each of the arms with opposite phases, the surface charge gradient across the gap vanishes, thus canceling the associated electric field. Beyond the change within the gap region, driving the antenna with a HG_{10} beam instead of a Gaussian beam leads also to a displacement of the TPL emission from the outer extremities toward the center of each arm. Further data were acquired for different relative positions between the π-phase shift of the incident HG_{10} beam and the gap of the nanoantenna (Figure 4.4). These data show that the minimum of TPL emission in the gap region is observed within a range of about 100 nm around the gap center. Any lateral shift within this range only alters the symmetry of the TPL distribution along the overall antenna.

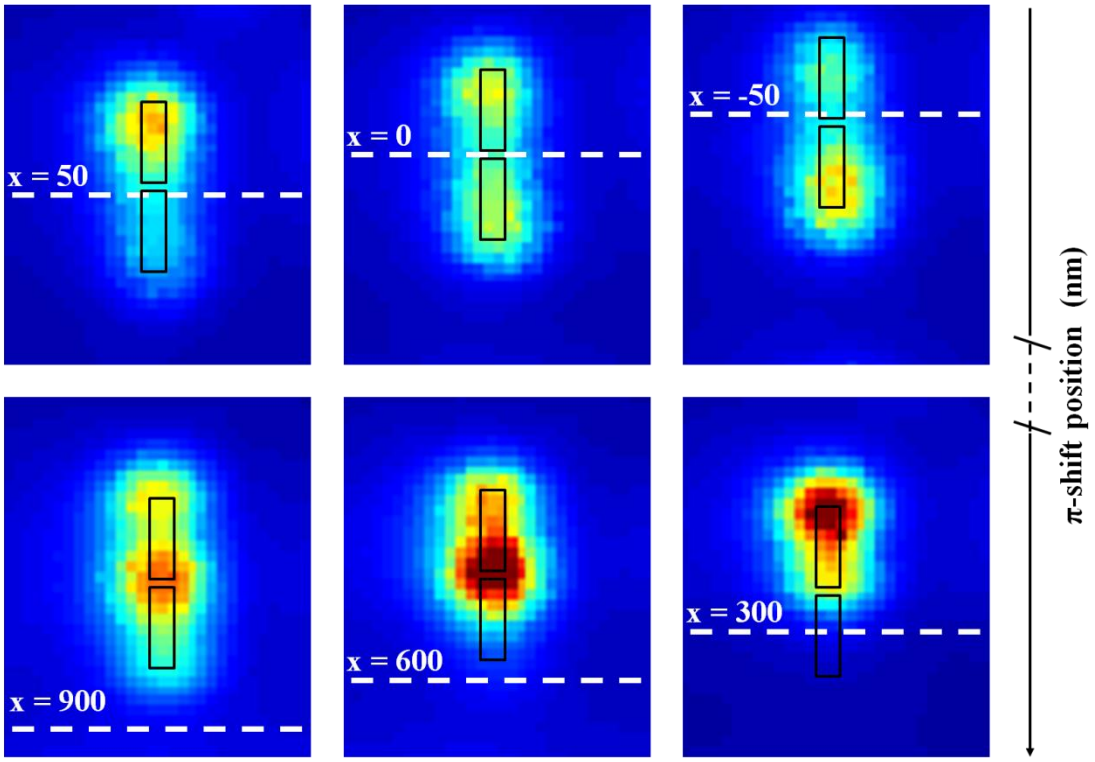

Figure 4.4: TPL distributions recorded on a gap antenna as a function of the relative position of the π-phase shift of the incident HG_{10} with respect to the antenna. *The TPL*

emission from the antenna has a minimum in the gap when the π-phase shift of the incident HG_{10} beam is located within a range of about $100\ nm$ around the gap (top row). When either of the two antenna arms overlaps the π-phase shift ($x = 300\ nm$), its emission is completely quenched and the antenna emission resembles the emission of a single rod [Ghenuche et al. (2008)]. Finally, the antenna emission is again dominated by a maximum in the gap, when the entire antenna is contained within an area of constant polarization ($x = 900\ nm$).

At this stage, in order to verify that the change in the antenna mode distribution is not governed by the intensity distribution of the electric field of the HG_{10}, it is instructive repeating the experiment for a LG_{20} beam (Figure 4.3 (e-f)). While the LG_{20} beam, like the HG_{10} beam, features a minimum in intensity at its center, its polarization is in-phase on both sides of the $x = 0$ axis. The TPL distribution was found to be very similar to the Gaussian case, confirming that the phase change across the antenna is the main parameter which controls its near-field optical response.

4.1.4 Simulated field and charge distributions

To get further insight into the physics involved and validate the experimental data, numerical calculations based on the green dyadic method were performed [Appendix A]. The distribution of the fourth power of the electric near-field within the half plane of the antenna was calculated for each type of beam. Additionally, for a more direct comparison with the experimental data to account for the finite resolution of the confocal setup, the maps were convoluted with a Gaussian profile ($300\ nm$ waist). Moreover, in order to appropriately approximate the actual illumination conditions in the real experiment, the incident electric field was first modeled in its paraxial expression, and then focused through an aplanatic optical lens with an adequate numerical aperture ($NA = 0.4$) [Leutenegger *et al.* (2006)].

For each of the illumination conditions, a very good agreement is found between the calculated mode maps, shown in Figure 4.5, and the TPL data of Figure 4.3. In order to better understand the origin of the local changes induced by the introduction of a π-phase jump at the gap location, it is instructive to map the actual distribution of surface charges, given by the divergence of the electric field, for the three beams considered in the experiments (Figure 4.5 (d-f)). Each of the maps has been normalized to its respective maximum for a clearer comparison. The equal periodicity in the surface charge oscillations shows that the same ($3\lambda/2$) antenna mode is coupled in each of the individual bars independently of the incident beam, as already suggested by the hybridization model. A major difference is observed for the HG_{10} beam, for which the gradient of opposite charges vanishes within the gap region (Figure 4.5 (e)). This further confirms that the cancelation of the local field within the gap is a consequence of simultaneously driving in phase opposition the antenna's arms, and consequently of coupling to the antenna's antibonding mode – also known as dark mode. A comparison of the maps (d) and (e) of Figure 4.5 also provides some insight on the substantial

differences in the local field distribution along the arms between the HG_{10} and the Gaussian beam. Although the same mode of the individual bars is coupled in both cases, for the HG_{10}, the higher ratio between the magnitude of charges along the bars and at their extremities explains the displacement of the field intensity toward the center of the bars.

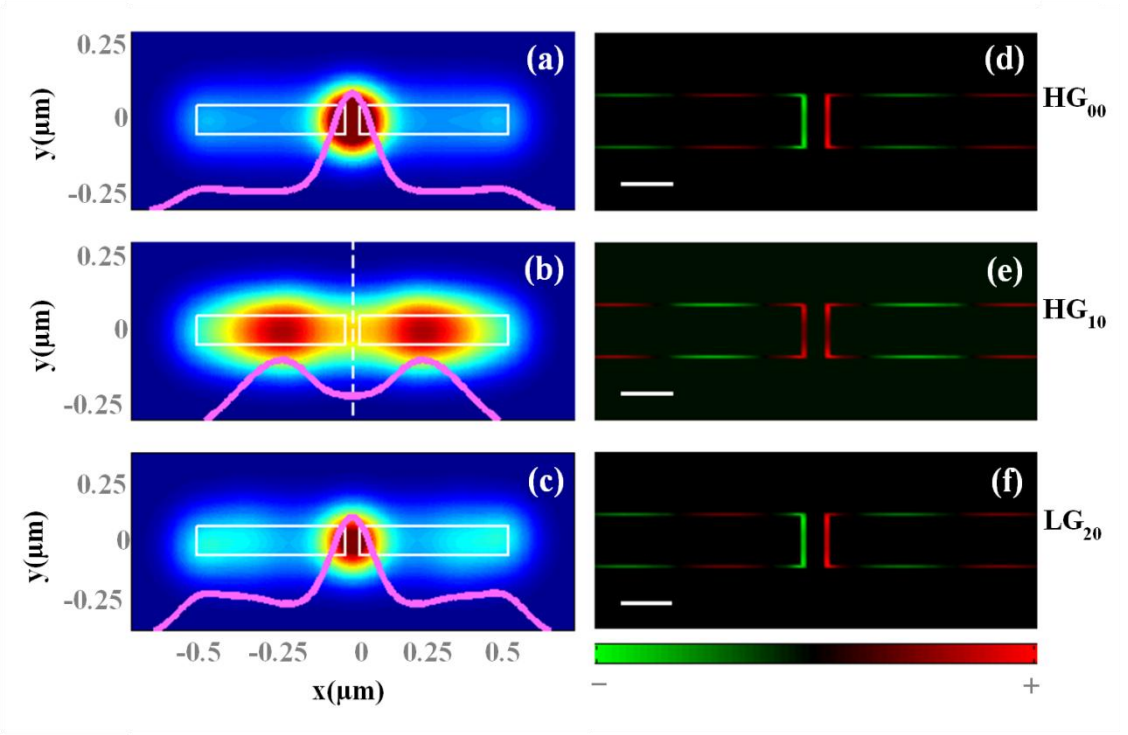

Figure 4.5: Simulated near field optical patterns and charge distributions of a gap antenna driven by higher-order beams. (a-c) *Convoluted* $|E|^4$*maps computed in the half-plane of a gap antenna for three types of beams considered in the experiments of Figure 4.3. In* (b)*, the vertical dashed line locates the* π*-shift position of the* HG_{10} *beam.* (d-f) *Associated surface charge distributions (scale bar, 100 nm).*

4.2 Towards More Complex Architectures

In what follows, Hermite-Gaussian beams are used to deterministically control the confinement of light in more complex plasmonic architectures. The first geometry is a double gap antenna formed by three 500-nm aligned gold bars separated by two identical 50-nm air gaps. For reference, a TPL map was first recorded when driving the whole antenna with a Gaussian beam linearly polarized along the x-axis. As expected, field enhancement was observed in both gaps (Figure 4.6 (a)). Figure 4.6 (b) and (c), instead, show TPL maps recorded when the π-phase shift of a HG_{10} beam coincides successively with the right and left gaps, so that one of the three rods forming the antenna is always driven in opposition of phase to the other two arms. These data demonstrate how a suitable positioning of the phase jump over the double antenna enables one to selectively switch on and off one of the two *hot-spot* sites.

While these results provide a first experimental evidence of the feasibility of using spatial phase-shaped beams for controlling the near field distribution of plasmonic systems, it is important at this stage to evaluate the potentiality of this approach to achieve spatial light control within a subwavelength region. For this purpose, numerical simulations were performed on a 3×4 array of $100\ nm$ gold pads separated by 30-nm gap when illuminated by different Hermite-Gaussian beams. Figure 4.7 shows the evolution of the computed electric near-field intensity distribution at its collective plasmon resonance ($860\ nm$) for different (n, m) sets. According to Equation (1.4), this structure covers a surface area that is commensurable with the diffraction limited focus ($375\ nm$ for a wavelength of $860\ nm$ and for $NA = 1.4$), delimited by a dashed circle in Figure 4.7.

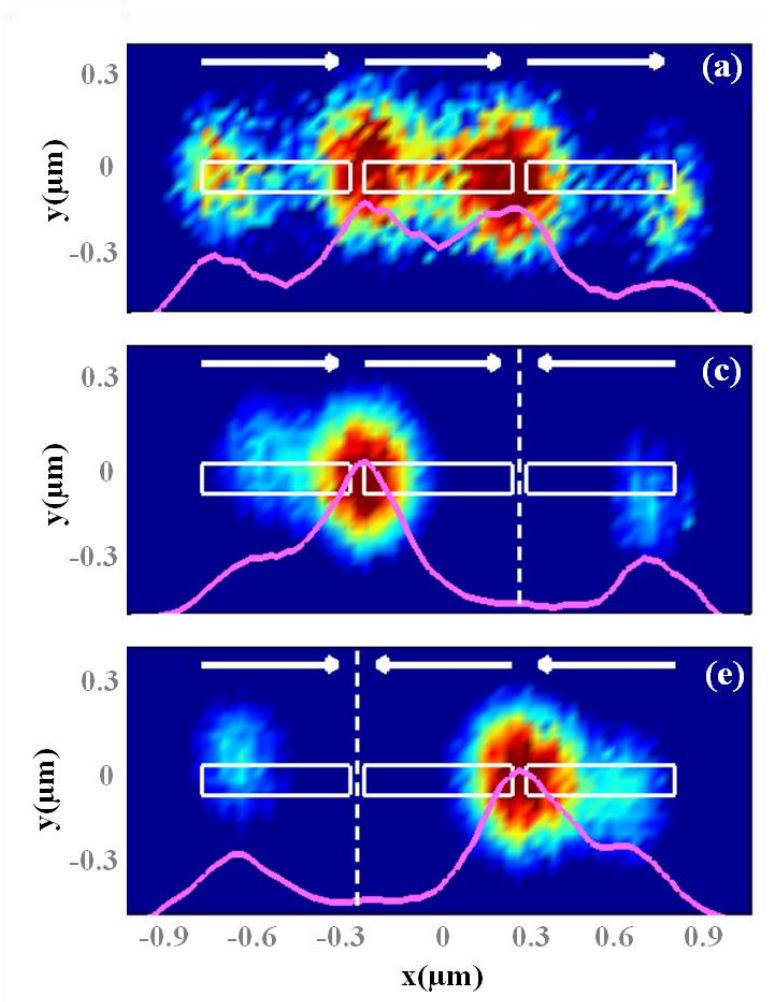

Figure 4.6: TPL distributions recorded on a double gap antenna driven by higher-order beams. *Experimental TPL maps recorded for* (a) *a Gaussian beam, and* (b-c) *for a* HG_{10} *beam whose π-phase shift (located by the vertical dashed line) coincides with* (b) *the right gap and* (c) *the left gap.*

For reference, Figure 4.7 (a-b) displays the near-field map when illuminating the array with a $500\ nm$ waist Gaussian beam linearly polarized along the x-axis. Under these conditions, an intensity maximum is observed at each of the gaps oriented

perpendicular to the incident field. By switching to a HG_{01}, whose phase jump coincides with the central line, the field along the later is inhibited and only the gaps of the outer rows remain bright (Figure 4.7 (c-d)). Conversely, the use of a HG_{04} enables a reverse situation where the light is exclusively confined within the gaps of the central row (Figure 4.7 (d-e)). In this case, therefore, the minimum distance between two *hot spots* that can be selectively switched on and off is of the order of $100\,nm$, i.e. three times shorter than the diffraction limit at the considered wavelength.

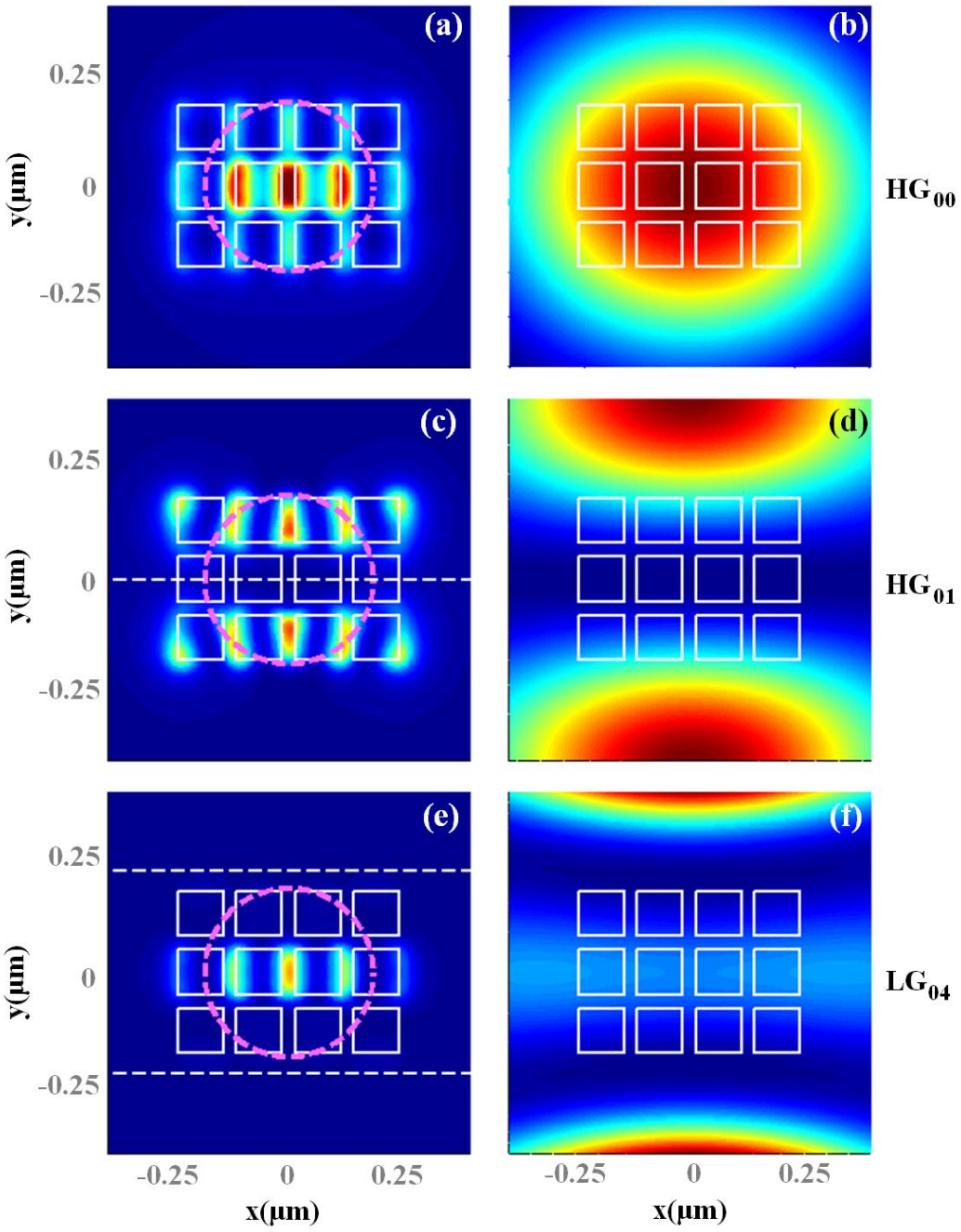

Figure 4.7: Subwavelength control of the emission of a complex plasmonic architecture. (a,c,f) *Numerical electric neat-field intensity distribution computed for different illumination around a* 3×4 *matrix of 100-nm gold pads separated by 30-nm gaps. The*

incident wavelength is 860 nm *and the polarization is aligned along the* x*-axis. The pink dashed circle depicts the limit of diffraction, while the dashed lines locate the* π*-phase shifts. All maps were normalized to the maximum of map* (a) *was applied.* (b,d,f) *Intensity distributions of the corresponding incident fields.*

Chapter 5

Towards a Deterministic Dynamic Control of Nanoantennas

The previous chapter introduced a new strategy for the accurate and dynamical control of the optical near-field on the subwavelength scale. This approach, based on continuous wave flows, consists in exploiting the spatial phase shaping – in opposition to a temporal phase shaping (Section 1.4.1) – of higher-order laser beams: for example, as seen, the phase jumps at the focus of Hermite-Gaussian beams enable the coupling of the incident field to a plasmonic dark mode in a gold gap antenna.

Achieving a deterministic control of the light confinement at any specific location of a generic plasmonic nanostructure, however, requires a procedure that enables one to determine the actual incident field that leads to the desired near-field pattern. To this end, this chapter proposes a novel, fully deterministic numerical protocol towards the control of the optical near-field response of a generic nanosystem in an accurate and dynamical way. The so-called deterministic optical inversion (DOPTI) algorithm enables one to reconstruct, from a desired near-field pattern, the closest physical solution for the incident field, expressed on a basis of focused higher-order beams [Appendix C]. This protocol combined with spatial phase shaping by a spatial light modulator (SLM) offers a realistic approach towards the dynamical control of the near-field of any linear nanosystems.

5.1 DOPTI: The Inversion Algorithm

The general principle behind the DOPTI algorithm can be understood by considering a standard configuration in which a continuous incident field $\mathbf{E_{in}}$, after focusing through an objective lens, impinges on a generic nano-object of dielectric function $\varepsilon_{ob}(\omega)$. Upon linear interaction, the electric field $\mathbf{E_{out}}$ inside the object connects to $\mathbf{E_{in}}$ by:

$$\mathbf{E_{out}} = \mathbb{X}\,\mathbf{E_{in}}, \tag{5.1}$$

as sketched in Figure 5.1 (left red path). In this functional equation, $\mathbb{X}$ is a linear operator that describes the optical response of the nano-object and is derived from Maxwell's equations.

As shown in the right blue path of Figure 5.1, a full control of the optical near-field response would consist in retrieving the incident field $\mathbf{E_{in}^{i}}$ that leads to the desired output field $\mathbf{E_{out}^{i}}$ by solving:

$$\mathbf{E_{in}^{i}} = \mathbb{X}^{-1}\mathbf{E_{out}^{i}}, \tag{5.2}$$

where the linear operator $\mathbb{X}$ is assumed to be invertible. This is usually the case although special attention must be paid when $\mathbb{X}$ is singular [Bretscher (1995)].

The following discussion focuses on the Green dyadic method [Appendix A] in order to find a generalized expression for the matrix $\mathbb{X}$, but any other solver of Maxwell's equations could be used equivalently.

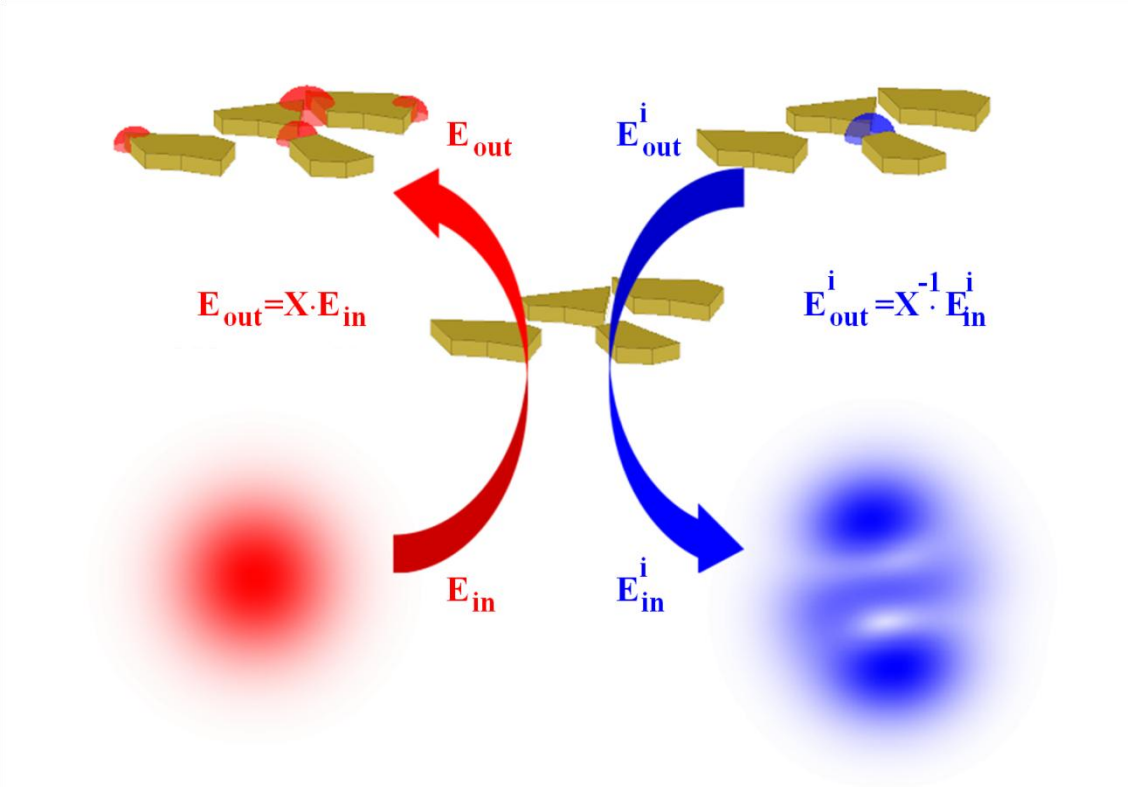

Figure 5.1: Schematic of the DOPTI algorithm. *The left path (red) sketches a situation in which a Gaussian beam (*$\mathbf{E_{in}}$*) impinges on the structure leading to the output field (*$\mathbf{E_{out}}$*). The right path (blue) sketches the reverse situation in which the optimal incident field* $\mathbf{E^i_{in}}$ *is computed from the desired output field* $\mathbf{E^i_{out}}$.

5.1.1 Eigenmode analysis

An absolute control of the near-field of any nano-object requires controlling the coherent coupling of a superposition of its eigenmodes [Stockman *et al.* (2002)]. The goal here is, therefore, to make explicit the connection between the desired near-field pattern $\mathbf{E^i_{out}}$ and the eigenmodes of the nanosystem.

To this end, the first step involves looking for the self-consistent electric field $\mathbf{E_{out}}$ inside the nano-object by discretizing its volume V into N identical subwavelength dipoles located at the positions $\mathbf{r_i}$, where $i \in [1, N]$. This procedure generates a system of N vectorial equations with N unknown fields $\mathbf{E_{out}}(\mathbf{r_i})$:

$$\mathbf{E_{out}}(\mathbf{r_i}) = \mathbf{E_{in}}(\mathbf{r_i}) + \chi \frac{V}{N} \sum_{j=1}^{N} \mathbb{S}\,(\mathbf{r_i}, \mathbf{r_j}) \mathbf{E_{out}}(\mathbf{r_j}). \tag{5.3}$$

where $\chi(\omega) = \frac{\varepsilon_{ob}(\omega) - \varepsilon(\omega)}{4\pi}$, being $\varepsilon_{ob}(\omega)$ and $\varepsilon(\omega)$ the frequency dependent dielectric functions of the metal and of the surrounding, $\mathbb{S}\,(\mathbf{r_i}, \mathbf{r_j}) = \mathbb{S}_0(\mathbf{r_i}, \mathbf{r_j}) + \mathbb{S}_{\text{surf}}(\mathbf{r_i}, \mathbf{r_j})$ is

the Green dyadic tensor including a free-space term $\mathbb{S}_0(\mathbf{r_i}, \mathbf{r_j})$ and a reflection term $\mathbb{S}_{\text{surf}}(\mathbf{r_i}, \mathbf{r_j})$ accounting for the presence of a surface [Appendix A].

Equation (5.3) forms a linear system that can be rewritten in a simplified notation, after removing the self-consistency [Appendix A]:

$$\mathbf{E}_{\text{in}} = \mathbb{M}\,\mathbf{E_{out}}, \tag{5.4}$$

where $\mathbf{E}_{\text{in}}$ and $\mathbf{E_{out}}$ are $3N$-supervectors defined by $\mathbf{E}_0 = (\mathbf{E}_0(\mathbf{r}_1),\ \mathbf{E}_0(\mathbf{r}_2), \dots, \mathbf{E}_0(\mathbf{r}_{\text{N}}))$ and $\mathbf{E_{out}} = (\mathbf{E_{out}}(\mathbf{r}_1),\ \mathbf{E_{out}}(\mathbf{r}_2), \dots, \mathbf{E_{out}}(\mathbf{r}_{\text{N}}))$. $\mathbb{M}$ is a $(3N \times 3N)$ invertible matrix [Appendix A], formed by the (3×3) elements $\mathbb{M}_{ij} = \boldsymbol{\delta}_{ij} - \chi \frac{V}{N} \mathbb{S}(\mathbf{r_i}, \mathbf{r_j})$.

At this stage, the eigenmode analysis of the inverse of the matrix $\mathbb{M}$ would allow one to determine all the possible fundamental illumination conditions (eigenvectors) of the nanosystem under study, together with their frequency-dependent resonant behavior (eigenvalues). This analysis can be performed analytically in the case of single dipoles, like in Equations (1.7) and (1.8). In a more complex system instead, a more general method must be developed in order to relate the desired near-field pattern $\mathbf{E^i_{out}}$ to the optimal superposition of eigenmodes, thus to the optimal incident field $\mathbf{E^i_{in}}$.

5.1.2 Projection on a basis of higher-order beams

Equation (5.4) always provides a mathematical solution for the incident field $\mathbf{E^i_{in}}$ associated to any distribution of the desired field $\mathbf{E^i_{out}}$, which has been previously defined in magnitude and phase at the center of every mesh. However, the practical implementation of this inversion approach depends on whether there is a physical incident field close enough to the ideal mathematical solution that can be created in a standard experimental configuration that is, from the collimated Gaussian beam of a laser. For example, the ideal mathematical solution may include evanescent components or spatially next-by phase discontinuities that are hard to control in a standard experimental configuration.

In order to overcome this issue, an additional condition must therefore be imposed: the field $\mathbf{E^i_{in}}$ must be decomposable on a basis $\mathbb{H}$ of n focused Hermite-Gaussian beams, whose symmetry axis coincides with the origin of the Cartesian coordinates $\mathbf{r_0} = \mathbf{0}$. For practical purposes, the infinite expansion of Hermite-Gaussian beams has to be truncated into a finite superposition of incident modes. The choice of such a basis allows one to establish a direct link with standard experimental conditions, where the incident field is the result of focusing a paraxial beam through an aplanatic lens [Novotny & Hecht (2006); Leutenegger *et al.* (2006)]. On the one hand, Hermite-Gaussian beams form an orthogonal basis that can completely describe any paraxial beam before the lens [Siegman (1986)] and, on the other hand, they can feature, after focusing, phase singularities at the subwavelength scale [Berry (1994)]. $\mathbf{E^i_{in}}$ can therefore be expressed as:

$$\mathbf{E}_{\mathbf{in}}^{\mathbf{i}} = \mathbb{H}\,\boldsymbol{\beta}, \tag{5.5}$$

where $\boldsymbol{\beta}$ is the vector containing the complex coefficient of the superposition, and $\mathbb{H}$ is a $(3N \times n)$ matrix whose columns contains the complex values of the focused elements of the selected basis at each mesh position of the nano-object under study.

Inserting Equation (5.5) into Equation (5.4) makes explicit the linear relationship between the unknown coefficients of the superposition $\boldsymbol{\beta}$ and the desired output field $\mathbf{E}_{\mathbf{out}}^{\mathbf{i}}$:

$$\mathbf{E}_{\mathbf{out}}^{\mathbf{i}} = \mathbb{M}^{-1}\mathbb{H}\,\boldsymbol{\beta}, \tag{5.6}$$

Equation (5.6) is a linear overdetermined system with $3N$ equations and n unknowns ($3N \gg n$). As a consequence, depending on the desired near-field pattern, a unique solution for Equation (5.6) does not always exist; a turnaround approach is to look for the value $\boldsymbol{\beta}^{\mathbf{a}}$ of the coefficients of the superposition that offers the best physical approximation $\mathbf{E}_{\mathbf{out}}^{\mathbf{a}}$ to our ideal electric field $\mathbf{E}_{\mathbf{out}}^{\mathbf{i}}$ such that:

$$\mathbf{E}_{\mathbf{out}}^{\mathbf{i}} = \mathbf{E}_{\mathbf{out}}^{\mathbf{a}} + \mathbf{r} = \mathbb{M}^{-1}\mathbb{H}\,\boldsymbol{\beta}^{\mathbf{a}} + \mathbf{r}, \tag{5.7}$$

where the $3N$-supervector $\mathbf{r}$ is the vector of residuals or error vector, that only vanishes when Equation (5.6) has a unique solution.

5.1.3 Least mean square solution

This becomes a standard fitting problem that can be solved by adopting any linear algorithm, such as a linear least mean squares algorithm (LMS) [Bretscher (1995)]. The LMS solution is, for example, given by [Bretscher (1995)]:

$$\boldsymbol{\beta}^{\mathbf{a}} = \left(\mathbb{X}^{\mathbf{h}}\mathbb{X}\right)^{-\mathbf{1}}\mathbb{X}^{\mathbf{h}}\mathbf{E}_{\mathbf{out}}^{\mathbf{i}}, \qquad \mathbb{X} = \mathbb{M}^{-1}\mathbb{H}, \tag{5.8}$$

$$\mathbf{r} = \mathbf{E}_{\mathbf{out}}^{\mathbf{i}} - \mathbf{E}_{\mathbf{out}}^{\mathbf{a}} = \mathbf{E}_{\mathbf{out}}^{\mathbf{i}} - \mathbb{X}\,\boldsymbol{\beta}^{\mathbf{a}}, \tag{5.9}$$

where the matrix $\mathbb{X}^{\mathbf{h}}$ is the transpose conjugate (Hermitian) of $\mathbb{X}$. Unlike Equation (5.6), given a certain geometry ($\mathbb{M}$) and some free space conditions ($\mathbb{H}$), the first implication of Equations (5.8) and (5.9) is that it is always possible to find one and only one solution $\boldsymbol{\beta}^{\mathbf{a}}$ to the linear set of Equation (5.8), because the $(n \times n)$ matrix $\left(\mathbb{X}^{\mathbf{h}}\mathbb{X}\right)^{-\mathbf{1}}\mathbb{X}^{\mathbf{h}}$ is always full rank by construction. It is also interesting to note that finding the best physical approximation to the incident field $\mathbf{E}_{\mathbf{in}}^{\mathbf{i}}$, calculated directly

from Equation (5.4), by applying the LMS method to Equation (5.5), is not equivalent to solving Equation (5.8) because matrix $\mathbb{M}$ is not unitary ($\mathbb{M}\,\mathbb{M}^{\mathbf{h}} \neq \mathbf{I}$).

At this stage, summing the different elements of the basis $\mathbb{H}$, after weighting them for the complex coefficients $\boldsymbol{\beta}^{\mathbf{a}}$, finally gives the distribution of the incident field in order to obtain the best approximation to the initial $\mathbf{E}^{\mathbf{i}}_{\mathbf{out}}$, by solving the standard direct problem of Equation (5.1). Assuming paraxial approximation for the incoming field at the entrance of the objective lens, the complex coefficients $\boldsymbol{\beta}^{\mathbf{a}}$ can also be used to reconstruct the incident field before focusing by superimposing the paraxial description of the Hermite-Gaussian beams of the basis $\mathbb{H}$ [Appendix C]. This is possible because the integration, which describes the effect of the focusing optics on the incoming field at the entrance of the objective lens, is a linear operation [Novotny & Hecht (2006); Leutenegger *et al.* (2006)].

The LMS solution also gives direct insight on how physical and viable our initial ideal field $\mathbf{E}^{\mathbf{i}}_{\mathbf{out}}$ is in terms of relative error r and absolute efficiency η. The normalized error and efficiency of the DOPTI algorithm can be estimated by applying the following equations:

$$r = \frac{\|\mathbf{r}\|^2}{\left[\!\left[\mathbf{E}^{\mathbf{i}}_{\mathbf{out}}\right]\!\right]^2} = \frac{\sum_{i=1}^{3N}|\mathbf{r}(i)|^2}{\sum_{i=1}^{3N}\left|\mathbf{E}^{\mathbf{i}}_{\mathbf{out}}(i)\right|^2}, \tag{5.10}$$

$$\eta = k\|\boldsymbol{\beta}^{\mathbf{a}}\|^2 = k\sum_{i=1}^{n}|\boldsymbol{\beta}^{\mathbf{a}}(i)|^2, \tag{5.11}$$

where k is a normalization constant: for example, $k = \max_{\mathrm{i}}\left|\mathbf{E}^{\mathbf{i}}_{\mathbf{out}}(i)\right|^2 / \max_{\mathrm{i}}|\mathbf{E}^{\mathbf{a}}_{\mathbf{out}}(i)|^2$, where $i \in [1,3N]$, ensures the same maximum intensity for the reconstructed output electric field and the originally desired one. Overall, the error r and the efficiency η respectively quantify the fidelity which the approximated solution describes the intended output field with, and the coupling efficiency of the desired incident field. According to this definition of efficiency, for $\mathbf{E}^{\mathbf{a}}_{\mathbf{out}}$ to reach the same maximum intensity as $\mathbf{E}^{\mathbf{i}}_{\mathbf{out}}$, the total power of the incident field has to be exactly η times higher. Finally, for most applications, the restrictive definition here adopted for the error r provides a worst-case scenario.

Even though there is no practical limitation on the choice of the desired near-field pattern, smaller errors and higher efficiency are expected for patterns that are close to a superposition of the eigenmodes of either the whole structure or a portion of it.

5.2 Numerical Case Studies

As case studies to illustrate the DOPTI algorithm, numerical simulations were performed over two ensembles of five $80x80x40\ nm^3$ gold nanopads, lying on a glass

substrate (ε_{gold} is taken from [Palik (1985)], $\varepsilon_{glass} = 2.3$ and $\varepsilon_{air} = 1$) and arranged to form two different patterns: a V-shaped structure (Figure 5.2 (a)) and a cross-shaped structure (Figure 5.2 (e)). The design parameters for these two structures are reported in Table 5.1.

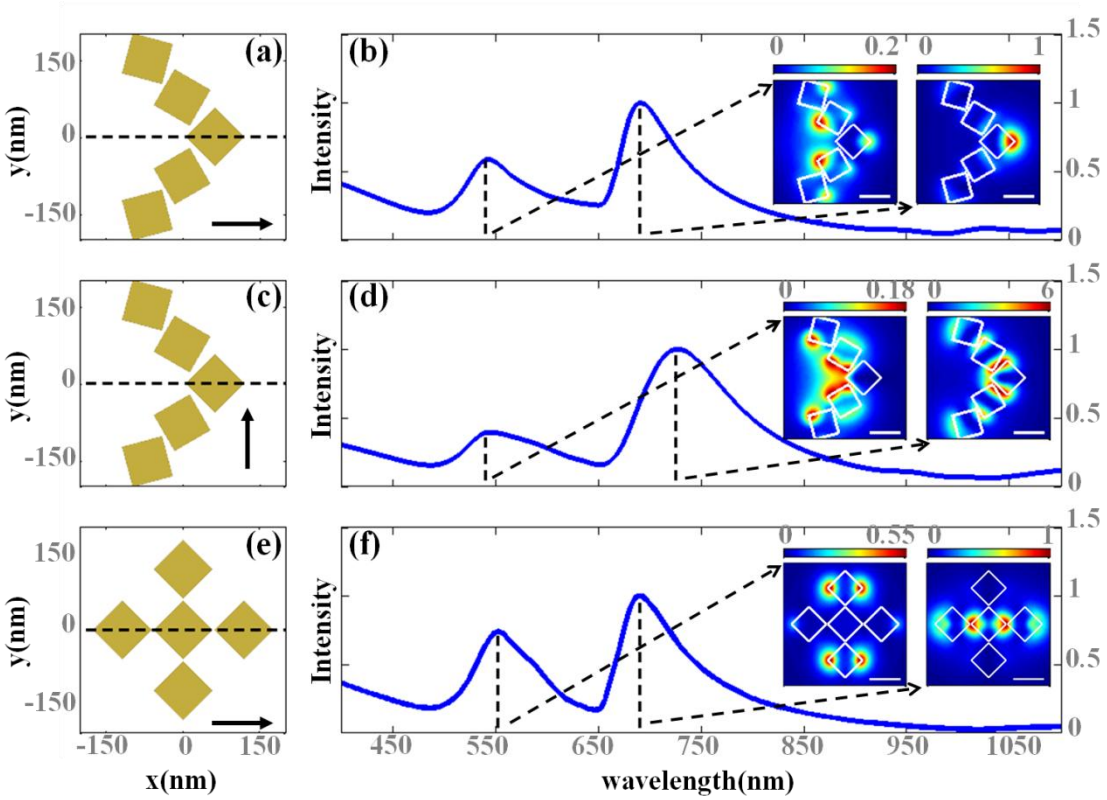

Figure 5.2: Partial control of the optical response of a nanostructure upon plane wave illumination. (a-b) *Geometry and normalized far-field scattering spectrum of a V-shaped structure illuminated by a plane wave linearly polarized along x (black arrow). The right insets show the normalized electric near-field intensities at* 545 *nm and* 690 *nm (white scale bar,* 100 *nm).* (c-d) *Geometry and normalized far-field scattering spectrum of the same structure illuminated by a plane wave linearly polarized along y (black arrow). The right insets show the normalized electric near-field intensities at* 550 *nm and* 725 *nm (white scale bar,* 100 *nm).* (e-f) *Geometry and normalized far-field scattering spectrum of a cross-shaped structure illuminated by a plane wave linearly polarized along x (black arrow). Due to the symmetry of the structure, the optical response of this structure does not change when illuminated by a plane wave linearly polarized along y. The right insets show the normalized electric near-field intensities at* 560 *nm and* 690 *nm (white scale bar,* 100 *nm). All near-field intensities were calculated* 20 nm *above the gold nanopads.*

For the two structures, Figures 5.2 (b), (d), and (e) plot the calculated far-field spectra for a plane wave illumination linearly polarized along the x- and y-direction. Upon each polarization, both structures feature two resonances each associated with a

different electric near-field intensity distribution (right insets of Figure 2 (b,d,f)). While changing the direction of the linear incident polarization and/or the wavelength leads to significant changes in the near-field response of these nanosystems, the degree of control that can be exerted still remains strongly limited and imposed by the fixed geometry.

V-shaped structure		Cross-shaped structure	
Coordinates (nm)	Orientation (rad)	Coordinates (nm)	Orientation (rad)
$(61.57, 0)$	$\pi/4$	$(0, 0)$	$\pi/4$
$(-1.93, 76.21)$	$-\pi/6$	$(118.14, 0)$	$\pi/4$
$(-1.93, -76.21)$	$\pi/6$	$(-118.14, 0)$	$\pi/4$
$(-69.13, 8.3)$	$-\pi/12$	$(0, 118.14)$	$\pi/4$
$(-69.13, -28.3)$	$\pi/12$	(0, -118.14)	$\pi/4$

Table 5.1: Design parameters of the V-shaped and the cross-shaped nanostructures. *The two structures are ensembles of five* $80x80x40\ nm^3$ *gold square pads arranged to form two different patterns: a V-shaped structure (Figure 5.2 (a)) and a cross-shaped structure (Figure 5.2 (e)). For every pad of the two structures, the coordinates of its center and its orientation with respect to the x-axis (black dashed line in Figure 5.2 (a,c,e)) are given.*

The DOPTI algorithm, nevertheless, allows one to control the output field of these two plasmonic structures in a very efficient and flexible way, and, by applying Equation (5.8), to identify the optimal incident field for a given desired output. In the following calculations, the expansion of the Hermite-Gaussian basis $\mathbb{H}$ was truncated to the first seven orders to limit the phase complexity, so that $\mathbb{H}$ is a $(3N \times 14)$ matrix – for each order, both orthogonal polarizations along the Cartesian axis, x and y, are considered [Appendix C]. Finally, the focusing optics was modeled through a high numerical aperture ($NA = 1.25$) aplanatic lens with a 3-mm entrance radius [Novotny & Hecht (2006); Leutenegger *et al.* (2006)].

5.2.1 Deterministic control on a V-shaped structure

Figures (5.3) (a-e) show different scenarios of subwavelength control that one would like to achieve over the V-shaped nanostructure of Figure (5.2) (a), where light is selectively coupled to one of the dipolar modes (resonance at around $560\ nm$) of each of the adjacent pads of the ensemble. In practice, the desired electric field $\mathbf{E}_{\mathbf{out}}^{\mathbf{a}}$ is

determined by computing the response of a single isolated pad upon a focused Gaussian illumination. This field is then imposed to the target pad of the complex nanosystem and used as input for the DOPTI algorithm in Equation (5.8). The distance between the centers of two adjacent pads is less than half the limit of diffraction according to Equation (1.4) – approximately $270\ nm$ at a wavelength of $560\ nm$ with $NA = 1.25$), represented by the pink dashed circle in Figures (5.3) (a-e).

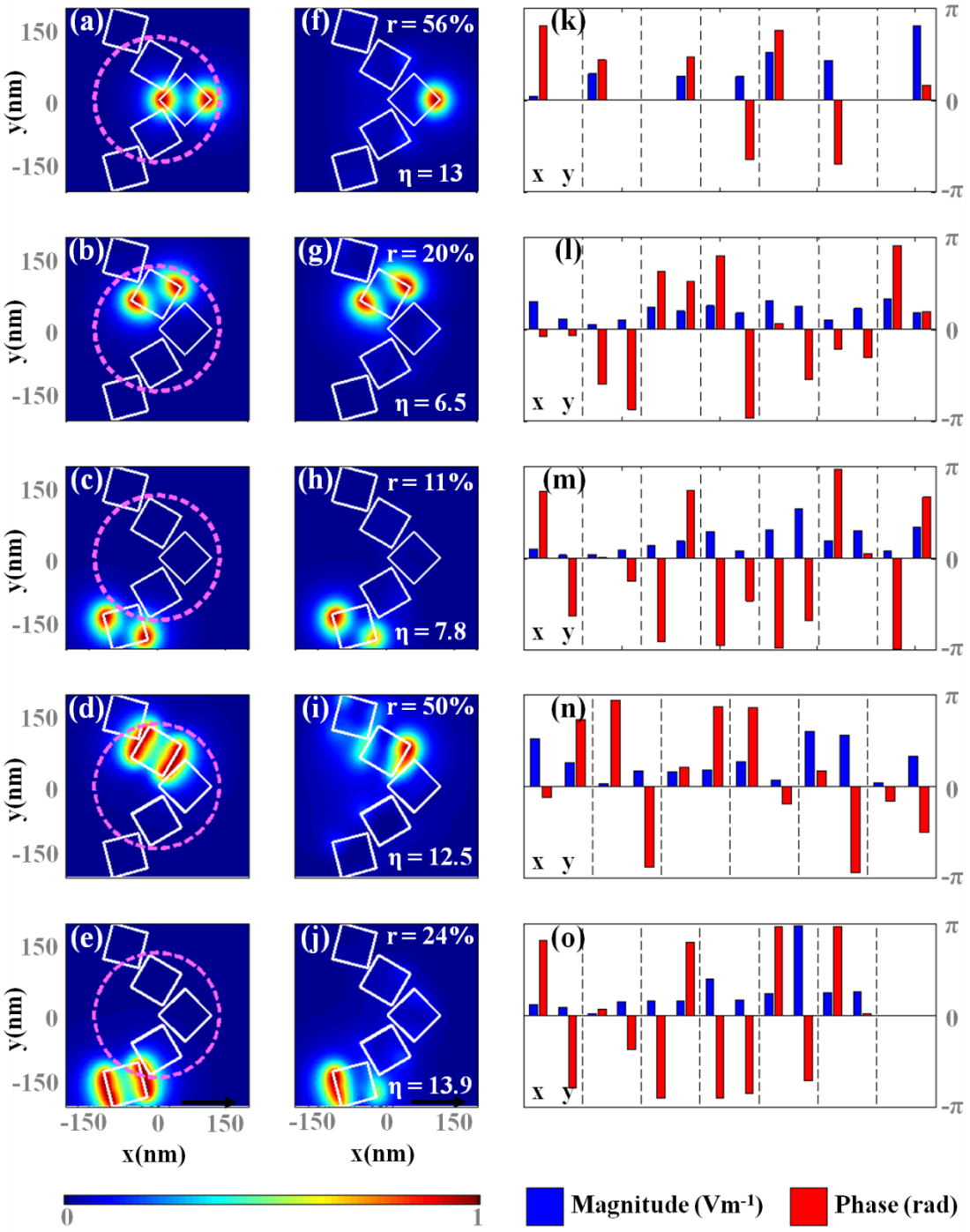

Figure 5.3: DOPTI subwavelength control on a V-shaped ensemble of gold nanoparticles. (a-e) *Normalized desired electric near-field intensity patterns at* $560\ nm$. *The pink dashed circle depicts the limit of diffraction.* (f-j) *Corresponding normalized*

reconstructed electric near-field intensities calculated from the five intended output near-field patterns in (a-e). *Error and efficiency are reported. The near-field intensities were calculated* 20 nm *above the pads.* (k-o) *Corresponding magnitude (blue) and phase (red) of the* β *coefficients of the superposition on a base of 14 Hermite-Gaussian beams. Every order* f *the base appears with the two orthogonal polarizations along* x *and* y. *Magnitude and phase are on the same scale, between* $-\pi$ *and* π.

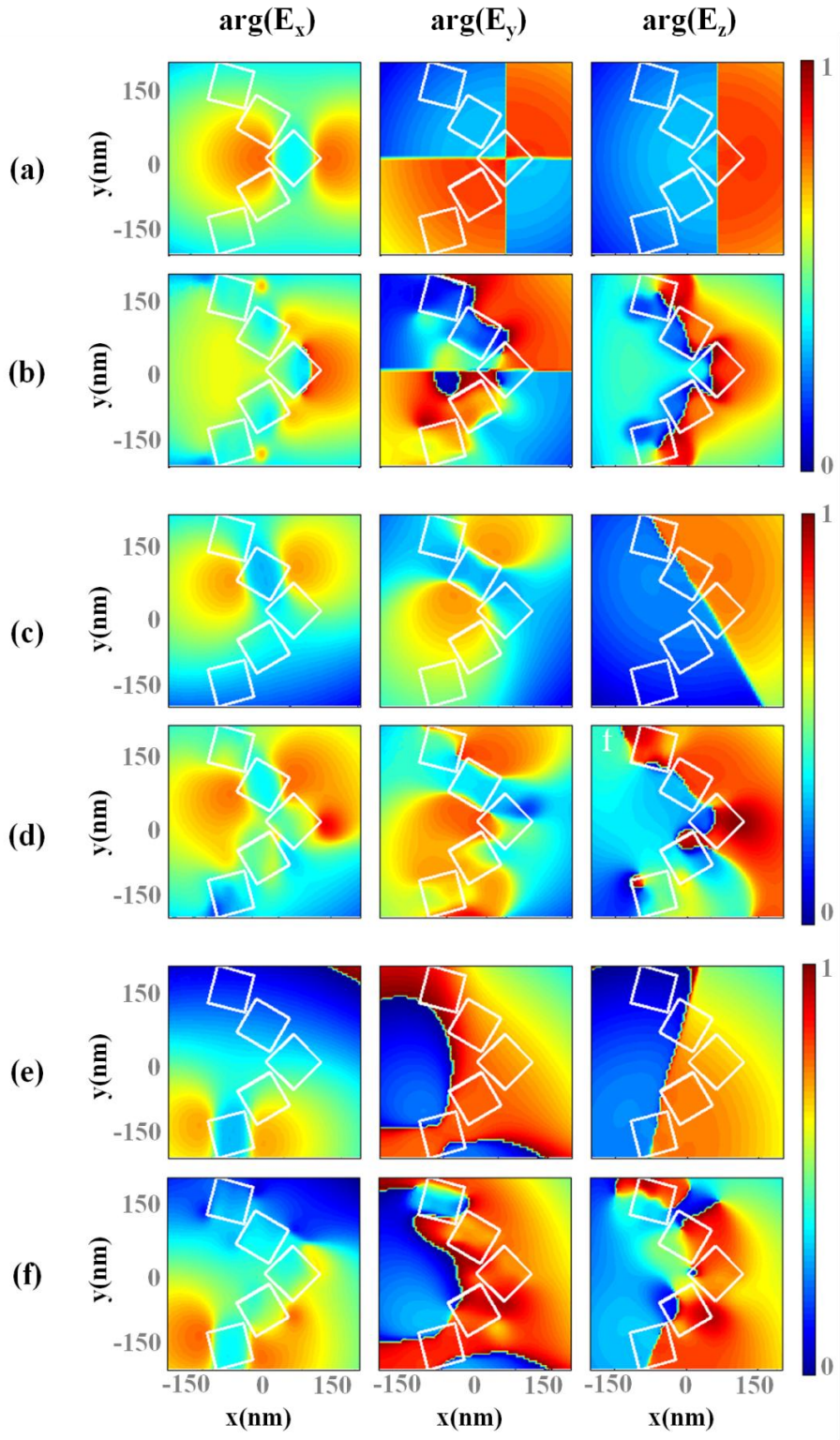

Figure 5.4: Phase information complementary to Figure 5.3. *Maps* (a, c, e) *shows the phase distributions for the x, y and z components of the desired electric near-field distributions, whose intensities are shown in Figure 5.3 (a-c) , respectively. Maps* (b, d, f) *shows the phase distributions for the x, y and z components of the corresponding reconstructed electric near-field distributions, whose intensities are shown in Figure 5.3 (f-h) , respectively.*

Figures 5.3 (f-j) show the intensity maps of the reconstructed near-field $\mathbf{E_{out}^{a}}$ associated to the desired near-field patterns of Figures 5.3 (a-e). Additionally, Figure 5.4 provides the corresponding desired and reconstructed phase distributions for the first three near-field patterns of Figure 5.3. Finally, Figures 5.3 (k-o) plot the associated magnitude and phase of the coefficients of the vector $\boldsymbol{\beta^{a}}$ that are needed in order to reconstruct the optimal incident field for the excitation of $\mathbf{E_{out}^{a}}$.

According to Equations (5.10) and (5.11), the error r is found to be of respectively 56%, 20%, 11%, 50% and 24%, while the efficiency η is respectively 13, 6.5, 7.8, 12.5 and 13.9. According to Equation (5.11), these values, which express the ratios between the power of the incident fields in the ideal case and in the DOPTI solution, ensure the same maximum intensity for the reconstructed output electric field and the originally desired one. The restrictive definition for the LMS error r provides a worst-case scenario. For instance, a definition of the error based on simply concentrating light around a single gold pad – that is, without necessarily reproducing exactly its dipolar mode pattern – would lead to much smaller errors of those in Figure 5.3. At this stage, it also becomes clear that an approach exclusively based on reproducing the required incident intensity pattern (without considering the phase distribution), for instance through a superposition of diffracted limited Gaussian spots, would suffer from a much lower level of control.

5.2.1 Deterministic control on a cross-shaped structure

In order to demonstrate the applicability of the DOPTI approach to other geometries, the cross-shaped ensemble of particles in Figure 5.2 (e) was also considered: here the aim is to selectively address optically the positions A, B and C, where, for example, several nearby nano-objects, such as nanoemitters, could be located. This time, the input of the DOPTI algorithm is the electric field $\mathbf{E_{out}^{i}}$ derived by concentrating light on the left corner of a single pad of the ensemble of particles. Tests on this nanostructure were performed at two wavelengths, $560\,nm$ and $690\,nm$, for which the respective limits of diffraction sit approximately at $270\,nm$ and $335\,nm$ – represented by the two pink circles in Figure 5.5 (a). For both wavelengths, the separation distance between points A, B and C is substantially less than half the limit of diffraction. Figures 5.5 (b) and (c) show how it is possible to selectively localize light at any of these points for both wavelengths with intensity ratio up to $1/100$. The corresponding normalized electric near-field intensities are reported in Figures 5.5 (d),

(e) and (f) for $\lambda = 560\ nm$, and in Figure 5.5 (g), (h) and (i) for $\lambda = 690\ nm$ together with the respective errors and efficiency according to Equations (5.10) and (5.11).

Accurate control of the field concentration at the three points is successively achieved at both wavelengths, showing that the DOPTI method is almost independent from the illumination wavelength. Nevertheless, efficiency and errors are better at 560 *nm* than at 690 *nm*, most probably because at the former wavelength the intended field patterns $\mathbf{E}^{\mathbf{i}}_{\mathbf{out}}$ are closer to the eigenmodes of the structure upon plane wave illumination.

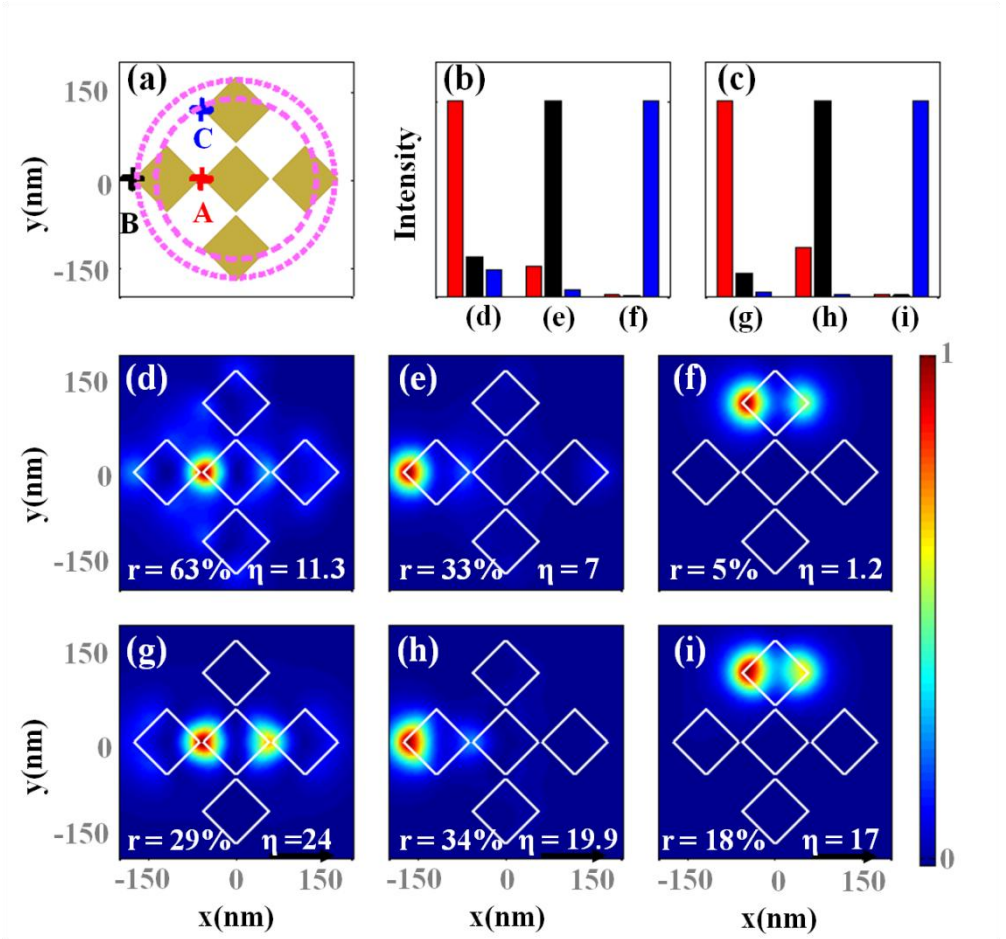

Figure 5.5: DOPTI subwavelength control on a cross-shaped ensemble of gold nanoparticles. (a) *The overall size of the cross-shaped nanostructure of Figure 5.2 (e) is comparable to the limit of diffraction for* 560 *nm and for* 690 *nm (two pink dashed circles, respectively).* (b-c) *Intensity concentration at points A (red), B (black) and C (blue) at* 560 *nm and at* 690 *nm, respectively.* (d-i) *Normalized electric near-field distributions calculated for the cases at* 560 *nm* (d-f) *and at* 690 *nm* (g-i). *The near-field intensities were calculated* 20 *nm above the pads.*

Conclusion

The work reported in this Thesis introduced new tools, both experimental and theoretical, to extend the current level of control over the spatial distribution of light on the subwavelength scale. Such a control is primarily important in order to extend concepts and functionalities of macro-optics down to the nanometer scale. A priori, however, optical control on this length scale goes against the law of diffraction of light, which, in fact, represents to ultimate limit to be overcome.

In the past decades, the concept of nanoantennas has emerged in plasmonics as an enabling technology for communicating energy to and from the nanoscale, and for controlling the spatial distribution of light on subwavelength scales [Novotny & van Hulst (2011)].

As seen in **Chapter 1**, learning how to accurately control the optical response of these nanoantennas represents a very promising approach to the dynamic control of the spatial distribution of light fields on the nanometer scale. In particular, two main complementary approaches have been traditionally followed in order to control the optical response of plasmonic nanoantennas: the first, *static approach* aims at optimizing the design of the nanoantenna as a function of its specific application, while the second, *dynamic approach* aims at reversibly tuning the optical near-field response of a given nanostructure by engineering its excitation light over time and space.

On the one hand, tailoring the shape and the dimensions of metal nanoparticles is a fundamental ingredient in order to tune plasmonic resonances and to control light fields on the nanoscale. Because of recent progress in numerical modeling and the spreading of nanofabrication techniques, single particles or simple systems of coupled particles are already well described and understood. As novel examples of static control, **Chapters 2 and 3** studied new designs of plasmonic nanostructures: **Chapter 2** proposed the use of fractal nanostructures to extend the degrees of freedom and the parameters available for the design of plasmonic structures [Volpe *et al.* (2011)], while **Chapter 3** characterized the performance of a unidirectional Yagi-Uda nanoantenna [Curto *et al.* (2010)]. As far as the static control is concerned, the new frontier, which still largely waits to be explored, is therefore represented by the study of systems of many particles, and their unique capabilities of molding light field on the nanoscale, both in term of intensity [Del Negro & Boriskina (2011)] and phase [Yu *et al.* (2011)].

On the other hand, the optical near-field distribution resulting from the interaction between light and plasmonic nanostructures is not only determined by the geometry of the metal system but also by the properties of the incident light: the accurate and dynamic control of the optical near-field on a subwavelength scale – independently of the geometry of the nanosctructure – is also a very important ingredient for the development of future nano-optical devices. To this end, **Chapters 4 and 5** described a new theoretical and experimental tool for the dynamic and deterministic control of the optical response of nanoantennas based on a spatial reconfiguration of the excitation light [Volpe *et al.* (2009); Volpe *et al.* (2010)]. Currently, while this task seems to be more and more at reach of present research developments [Gjonaj *et al.* (2011)], a last challenge is probably set by the realization of one comprehensive technique for the coherent control of plasmonic systems on the nanoscale that joins the advantages of a modulation of the incident field both in frequency and space.

Finally, complementing static and dynamic approaches in one powerful tool will enormously advance the current ability to control the optical response of nanoantennas over space and time on a subdiffraction scale. This advanced form of control will not only have fundamental implications in our understanding of the physics underlying nanoscale phenomena, but it will also be useful, in terms of applications, in order better control and enhance the efficiency, to name but a few, of photodetection, light emission, sensing, heat transfer, and spectroscopy on the nanometer scale.

List of Publications

VOLPE, GIORGIO, VOLPE, GIOVANNI & QUIDANT, ROMAIN (2011). Fractal plasmonics: subdiffraction focusing and broadband spectral response by a Sierpinski nanocarpet. *Optics Express*, **19**, 3612-3618.

VOLPE, GIORGIO, MOLINA-TERRIZA, GABRIEL & QUIDANT, ROMAIN (2010). Deterministic subwavelength control of light confinemt in nanostructures. *Physical Review Letters*, **105**, 216802.

CURTO, ALBERTO G., **VOLPE, GIORGIO**, TAMINIAU, TIM H., KREUZER, MARK P., QUIDANT, ROMAIN & VAN HULST, NIEK F. (2010). Unidirectional emission of a quantum dot coupled to a nanoantenna. *Science*, **329**, 930-933.

GRAELLS, SIMÓ, AÇIMOVIÇ, SRDJAN, **VOLPE, GIORGIO**, & QUIDANT, ROMAIN (2010). Direct growth of optical antennas using e-beam induced gold deposition. *Plasmonics*, **5**, 135-139.

VOLPE, GIORGIO, CHERUKULAPPURATH, SUDHIR, JUANOLA-PARRAMON, ROSER, MOLINA-TERRIZA, GABRIEL & QUIDANT, ROMAIN (2009). Controlling the optical near field of nanoantennas with spatial phase-shaped beams. *Nano Letters*, **9**, 3608-3611.

Appendix A

The Green Dyadic Method

Most of the calculations in this thesis are performed with a homemade Matlab code based on the Green dyadic method. This formalism, which only requires the definition of the geometry and the dielectric function of the object under study, provides a semi-analytical solution for the scattering problem, since it renders an analytical expansion of the electromagnetic field by numerical means. This appendix reviews the main information on this formalism; additional details can be found in [Martin *et al.* (1995); Girard (2005); Novonty & Hecht (2006)].

In the Green formalism, the self-consistent electric field $\boldsymbol{E}(\boldsymbol{r},\omega)$ inside a generic scatter can be obtained solving the correspondent wave equation using the *Lippmann-Schwinger* integral:

$$\boldsymbol{E}(\boldsymbol{r},\omega) = \boldsymbol{E}_0(\boldsymbol{r},\omega) + \int \chi(\omega)\boldsymbol{G}(\boldsymbol{r},\boldsymbol{r}',\omega)\,\boldsymbol{E}(\boldsymbol{r},\omega)d\boldsymbol{r}', \tag{A.1}$$

where $\chi(\omega) = \varepsilon_{ob}(\omega) - \varepsilon(\omega)$, being $\varepsilon_{ob}(\omega)$ and $\varepsilon(\omega)$ the frequency dependent dielectric functions of the scatter and of its surrounding, $\boldsymbol{G}(\boldsymbol{r},\boldsymbol{r}',\omega)$ is the Green dyadic tensor, and $\boldsymbol{E}_0(\boldsymbol{r},\omega)$ is the solution of the homogeneous wave equation (the absence of any scatter).

A.1 Discretization in the Source Region

Searching for exact solutions of Equation (A.1) requires a volume discretization procedure of the source region. As first step, we look for the self-consistent electric field inside the source region by discretizing its volume into N sub-wavelength meshes located at the positions $\boldsymbol{r}_i$, where $i \in [1,N]$. This procedure generates a system of N vectorial equations with N unknown fields $\boldsymbol{E}(\boldsymbol{r}_i,\omega)$:

$$\boldsymbol{E}(\boldsymbol{r}_i,\omega) = \boldsymbol{E}_0(\boldsymbol{r}_i,\omega) + \chi(\omega)\sum_{j=1}^{N} v_j \boldsymbol{G}(\boldsymbol{r}_i,\boldsymbol{r}_j,\omega)\boldsymbol{E}(\boldsymbol{r}_j,\omega). \tag{A.2}$$

This system of equations can be rewritten in a simplified notation, after removing the self-consistency:

$$\boldsymbol{E}_0 = \boldsymbol{M}\boldsymbol{E}, \tag{A.3}$$

where $\boldsymbol{E}_0$ and $\boldsymbol{E}$ are 3N-supervectors defined by $\boldsymbol{E}_0 = (\boldsymbol{E}_0(\boldsymbol{r}_1), \boldsymbol{E}_0(\boldsymbol{r}_2), \dots, \boldsymbol{E}_0(\boldsymbol{r}_N))$ and $\boldsymbol{E} = (\boldsymbol{E}(\boldsymbol{r}_1), \boldsymbol{E}(\boldsymbol{r}_2), \dots, \boldsymbol{E}(\boldsymbol{r}_N))$. $\boldsymbol{M}$ is a $(3N \times 3N)$ invertible matrix, formed by the (3×3)elements $\boldsymbol{M}_{ij} = \boldsymbol{\delta}_{ij} - \chi(\omega)v_j\boldsymbol{G}(\boldsymbol{r}_i,\boldsymbol{r}_j,\omega)$.

The electric field inside the source region can now be calculated by solving

$$\boldsymbol{E} = \boldsymbol{M}^{-1}\boldsymbol{E}_0, \tag{A.4}$$

And the electric field in a generic position $\boldsymbol{r}$ outside the source id deduced from the self-consistent field inside the structure:

$$\boldsymbol{E}(\boldsymbol{r},\omega) = \boldsymbol{E}_0(\boldsymbol{r},\omega) + \chi(\omega)\sum_{j=1}^{N} v_j \boldsymbol{G}\big(\boldsymbol{r},\boldsymbol{r}_j,\omega\big)\boldsymbol{E}\big(\boldsymbol{r}_j,\omega\big). \tag{A.5}$$

A.2 Explicit Expression of the Green Tensor

In order to model half-space problems, the green tensor $\boldsymbol{G}(\boldsymbol{r},\boldsymbol{r}',\omega)$ typically includes a free-space term $\boldsymbol{G}_0(\boldsymbol{r},\boldsymbol{r}',\omega)$ and a reflection term $\boldsymbol{G}_{surf}(\boldsymbol{r},\boldsymbol{r}',\omega)$ that accounts for the presence of a surface so that:

$$\boldsymbol{G}(\boldsymbol{r},\boldsymbol{r}',\omega) = \boldsymbol{G}_0(\boldsymbol{r},\boldsymbol{r}',\omega) + \boldsymbol{G}_{surf}(\boldsymbol{r},\boldsymbol{r}',\omega), \tag{A.6}$$

where the explicit expression for the free-space tensor is given by

$$\boldsymbol{G}_0(\boldsymbol{r},\boldsymbol{r}',\omega) = \frac{e^{ik|R|}}{4\pi\epsilon(\omega)}[-k^2\boldsymbol{T}_1(\boldsymbol{R}) - ik\boldsymbol{T}_2(\boldsymbol{R}) + \boldsymbol{T}_3(\boldsymbol{R})], \tag{A.7}$$

with $k = \sqrt{k_0\epsilon(\omega)}$, $\boldsymbol{R} = \boldsymbol{r} - \boldsymbol{r}'$, and $\boldsymbol{T}_1(\boldsymbol{R})$, $\boldsymbol{T}_2(\boldsymbol{R})$ and $\boldsymbol{T}_3(\boldsymbol{R})$ are three dyadic tensors that gradually describe the transition from near-field to far-field,

$$\boldsymbol{T}_1(\boldsymbol{R}) = \frac{\boldsymbol{R}\boldsymbol{R}^T - R^2\boldsymbol{I}}{R^3},$$
$$\boldsymbol{T}_2(\boldsymbol{R}) = \frac{3\boldsymbol{R}\boldsymbol{R}^T - R^2\boldsymbol{I}}{R^4},$$
$$\boldsymbol{T}_3(\boldsymbol{R}) = \frac{3\boldsymbol{R}\boldsymbol{R}^T - R^2\boldsymbol{I}}{R^5}.$$

The expression for the retarded surface propagator $\boldsymbol{G}_{surf}(\boldsymbol{r},\boldsymbol{r}',\omega)$ can be also calculated analytically for the most general case [Paulus *et al.* (2000)]; in the proximity of the surface, however, the following approximation holds:

$$\boldsymbol{G}_{surf}(\boldsymbol{r},\boldsymbol{r}',\omega) = \frac{1}{4\pi k}\frac{\varepsilon_{sub}(\omega) - \varepsilon(\omega)}{\varepsilon_{sub}(\omega) + \varepsilon(\omega)}\boldsymbol{G}^{surf}(\boldsymbol{r},\boldsymbol{r}'), \tag{A.8}$$

where the elements of $\boldsymbol{G}^{surf}(\boldsymbol{r},\boldsymbol{r}')$ are given by

$$G_{xx}^{surf} = \frac{2(x-x')^2 - (y-y')^2 - (z+z')^2}{R'}$$

$$G_{xy}^{surf} = \frac{3(x-x')(y-y')}{R'}$$

$$G_{xz}^{surf} = -\frac{3(x-x')(z+z')}{R'}$$

$$G_{yx}^{surf} = G_{xy}^{surf}$$

$$G_{yy}^{surf} = \frac{2(y-y')^2 - (x-x')^2 - (z+z')^2}{R'}$$

$$G_{yz}^{surf} = -\frac{3(y-y')(z+z')}{R'}$$

$$G_{xz}^{surf} = -G_{zx}^{surf}$$

$$G_{yz}^{surf} = -G_{zy}^{surf}$$

$$G_{xx}^{surf} = \frac{(x-x')^2 + (y-y')^2 - 2(z+z')^2}{R'}.$$

Finally, it is important to deal with the mathematical singularity of the free-space Green dyadic function $\boldsymbol{G}_0(\boldsymbol{r}, \boldsymbol{r}', \omega)$ for $\boldsymbol{r}' \to \boldsymbol{r}$. This divergence that occurs inside the source region can easily be removed [Yaghjian (1980)], and for a tridimensional mesh made of cubic or spherical cells of volume v , the limit reads

$$\boldsymbol{G}_0(\boldsymbol{r}, \boldsymbol{r}, \omega) = -\frac{1}{3v\epsilon(\omega)}\boldsymbol{I}. \tag{A.9}$$

Appendix B

Sample Nanofabrication

The metal nanostructures that appear in this thesis were mainly fabricated by e-beam lithography on positive electron-sensitive resist with either of two scanning electron microscopes: a FEI-QUANTA 200 or a FEI-INSPECT F50. Both microscopes are equipped with a RAITH-ELPHY+ control system for advanced lithography.

B.1 E-Beam Lithography on PMMA

The fundamental steps of the fabrication process are summarized in Figure B.1. The initial substrate for the lithography is made of glass, on which a 10-nm layer of Indium Tin Oxide (ITO) is deposited by e-beam deposition: electrically conductive and optically transparent, ITO does not significantly affect the final optical properties of the nanofabricated sample, and, at the same time, prevents its electric charging during the lithography process.

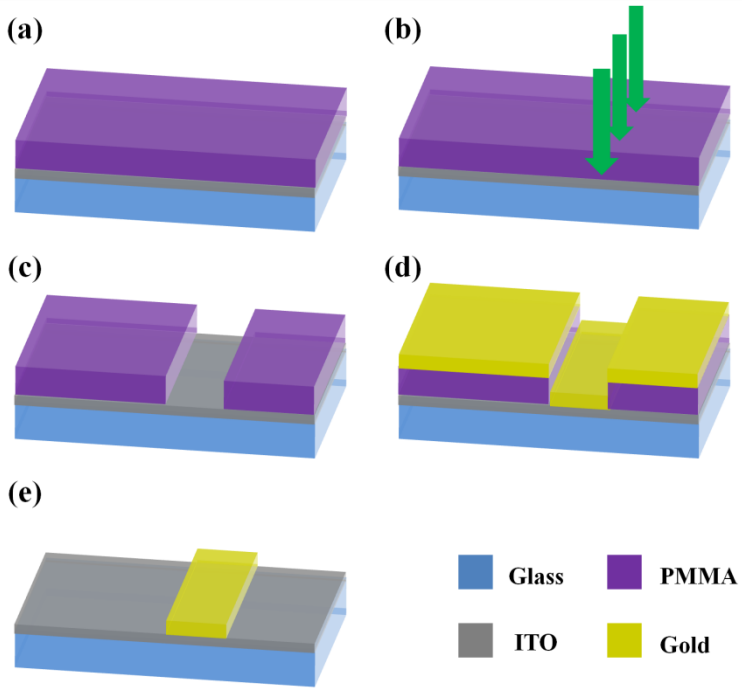

Figure B.1: Fundamental steps of e-beam lithography on positive resist. (a) *A thin film of positive resist, such as PMMA, is spin-coated over a glass sample covered with 10 nm ITO;* (b) *the resist is then patterned by exposure to an electron beam and* (c) *developed;* (d) *metal is deposited onto the sample;* (e) *after lift-off, the remaining resist is dissolved and the deposited metal stays anchored to the sample only in the areas that were originally exposed to the electron beam.*

A Polymethyl methacrylate (PMMA) film is then spin-coated onto the substrate. Typically, the resist thickness is at least three times the height of the desired metal nanostructures. At this point, the resist is patterned by an electron beam (acceleration voltage of 30kV), and developed in MIBK:IPA (3:1) immediately after. Using thermal

evaporation, a gold layer is deposited on the developed resist. Finally, after lift-off, the remaining resist is dissolved and the deposited metal stays only in the areas originally exposed to the electron beam.

B.2 Performance of the Fabrication Process

E-beam lithography on positive or negative electron sensitive resists combined with thermal evaporation of gold layers is a process that has been extensively used to fabricate arrays of plasmonic nanostructures, with remarkable results in terms of minimum gaps (a few nanometers) between adjacent structures [Açimoviç *et al.* (2009); Jain *et al.* (2007)]. The minimum size of the particles that can be fabricated depends on many factors, such as the resist resolution and thickness, the exposure dose, and the process of metal deposition. Figure B.2 (a), for example, shows an array of $50x50x30\ nm^3$ nanofabricated gold particles.

This method, in particular, suffers from the multi-crystalline character of the gold film produced by vapor deposition, where the precision of the fabricated structure is ultimately limited by the size of the vapor grains, typically from about 20 nm (Figure B.2 (b)).

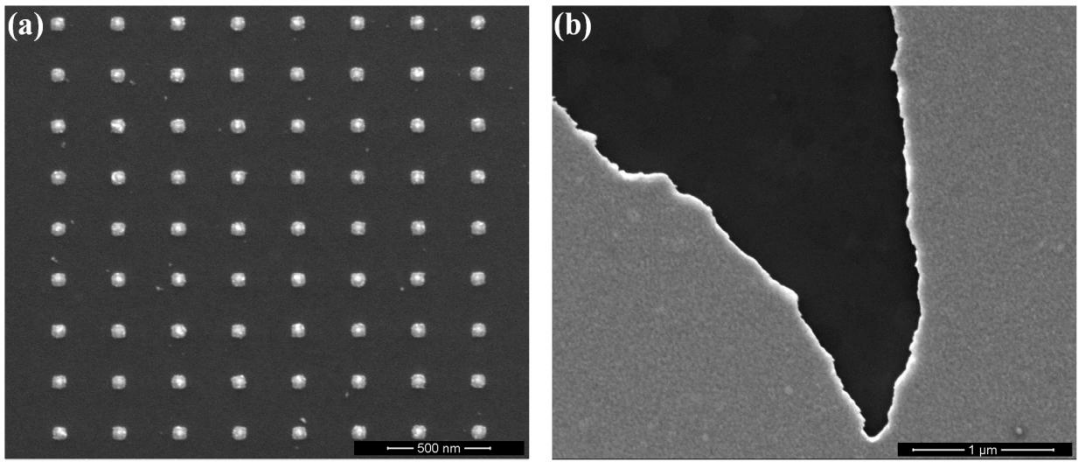

Figure B.2: Performance of the e-beam lithography on PPMA. (a) *A SEM micrograph of an array of* $50x50x30\ nm^3$ *nanofabricated gold particles: many independent factors can influence the resolution of the fabrication process, such as the resist and its thickness and/or the exposure dose.* (b) *A SEM micrograph of a typical gold surface (clearer area) produced by vapor deposition and consisting of randomly oriented grains from about 20 nm in size.*

Colloidal metal particles usually offer better crystallinity, but the accurate positioning of colloids onto a substrate still remains challenging, even though, recently, chemically grown single-crystalline gold flakes, after immobilization on a substrate, have been proposed as a platform for focused-ion beam (FIB) milling and other top-

down nanofabrication techniques for the fabrication of high-definition nanostructures on a substrate [Huang *et al.* (2010)].

Appendix C

Higher-Order Light Fields

Shaping the amplitude and phase of femtosecond light pulses is a useful tool to dynamically generate waveforms that are modulated both in frequency and space and that can be focused onto microscopic time domains on a femtosecond time scale [Wefers & Nelson (1993); Feurer *et al.* (2003)]. This shaping offers a unique opportunity to coherently control ultrafast phenomena on the nanoscale, where the phase and the polarization of the excitation pulse provide additional degrees of freedom to perform such a control.

In Chapter 4 and 5, this thesis proposes a novel approach based on continuous light flows to achieve a deterministic control of plasmonic fields by using the spatial phase inhomogeneities of higher order laser beams, such as Hermite-Gaussian and Laguerre-Gaussian beams. The interesting properties of these two sets of beams come from the fact that both independently form a complete orthogonal basis of solutions of the wave equation in paraxial approximation: any bidimensional complex light field can, therefore, be obtained as a superposition of these two sets of beams [Siegman (1986)]. In order to facilitate the reading of Chapter 4 and 5, this appendix reviews some general concepts about these higher-order beams.

C.1 Hermite-Gaussian Beams

The Hermite-Gaussian modes are light beams whose field distribution can be described by some complex functions based on the Hermite polynomials $H_n(x)$:

$$H_n(x) = (-1)^n e^{x^2} \frac{d^n}{dx^n} e^{-x^2} = e^{x^2/2} \left(x - \frac{d}{dx}\right)^n e^{-x^2/2}, \tag{C.1}$$

being the index n a non-negative integer. In Cartesian coordinates, when the direction of propagation is z, the analytical tridimensional expression for these beams then reads:

$$\begin{gathered} HG_{nm}(x,y,z) = HG_0 \frac{\omega_0}{\omega(z)} \times \\ H_n\sqrt{2}\frac{x}{\omega(z)} exp\left(-\frac{x^2}{\omega(z)^2}\right) H_m\sqrt{2}\frac{y}{\omega(z)} exp\left(-\frac{y^2}{\omega(z)^2}\right) \times \\ exp\left(-j\left[kz - (1+n+m)atan\frac{z}{z_0} + \frac{k(x^2+y^2)}{2R(z)}\right]\right) \end{gathered} \tag{C.2}$$

where $\omega(z)$ is the beam width, $\omega_0$the beam waist, k the wave number, and $R(z)$ is the radius of curvature of the beam's wave-front.

The Hermite-Gaussian beams have a Cartesian symmetry, and the indices n and m determine the shape of the beam profile in the x- and y-direction, respectively: the intensity distribution for these modes, in fact, has n intensity nulls (nodes) in the x-direction and m nodes in the y-direction, at each one of which the phase undergoes a jump of π radiants in the direction perpendicular to the node. Finally, a Gaussian beam

is obtained when $n = m = 0$. Figure C.1 plots intensity and phase profiles of the first twelve Hermite-Gaussian modes.

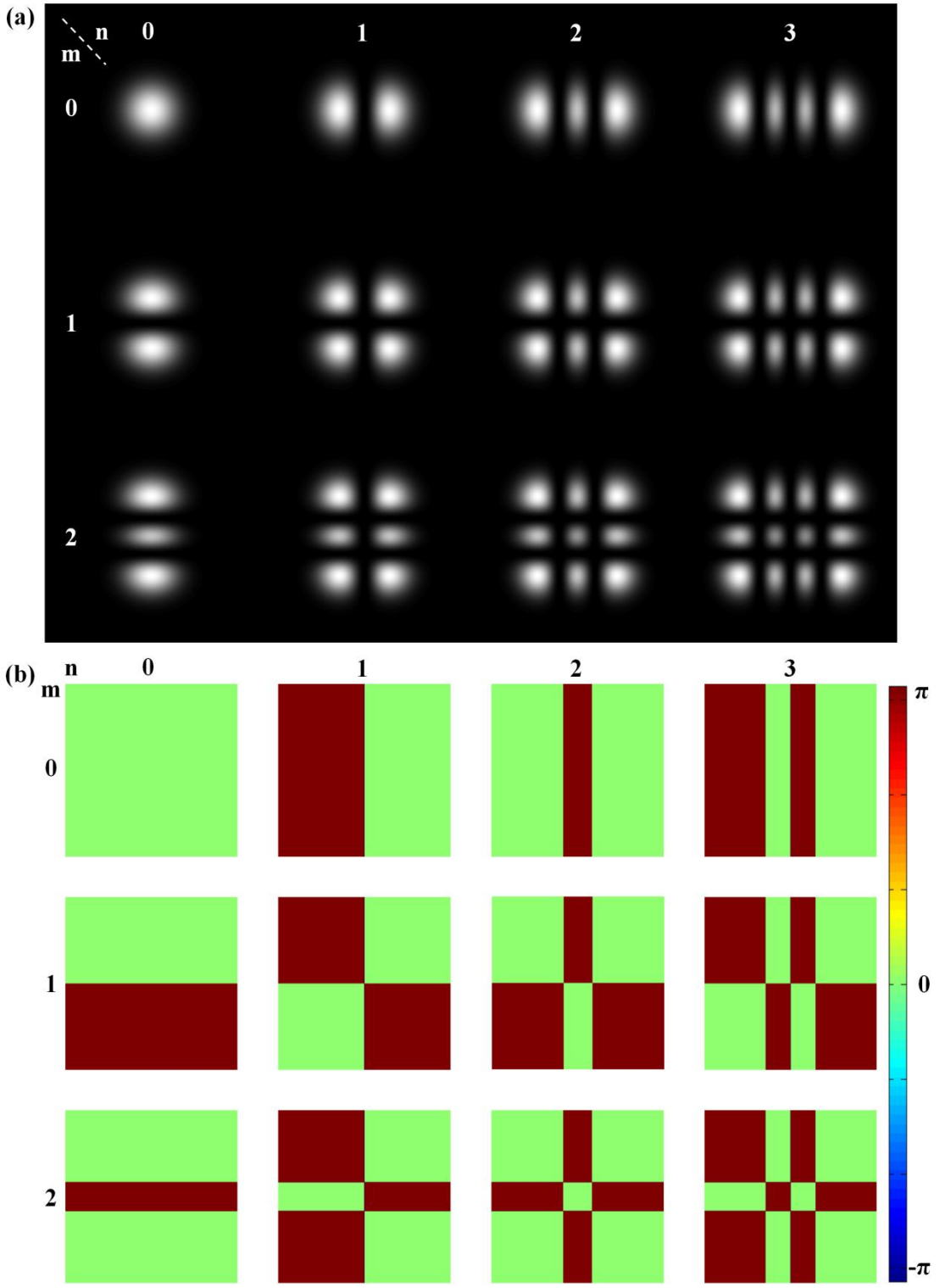

Figure C.1: First twelve Hermite-Gaussian beams. (a) *Intensity and* (b) *phase profiles of the first twelve Hermite-Gaussian beams: for Hermite-Gaussian modes, the indices* n and m *determine the shape of the beam profile by controlling the number of intensity*

nulls (and correspondent phase jumps) in the two orthogonal directions perpendicular to the direction of propagation of the beam.

C.2 Laguerre-Gaussian Beams

The Laguerre-Gaussian modes are light beams whose field distribution can be described by some complex functions based on the Laguerre polynomials $L_p^l(x)$:

$$L_p^l(x) = \frac{x^{-l}e^x}{p!}\frac{d^n}{dx^n}(e^{-x}x^{l+p}), \tag{C.3}$$

being the index l any integer, and the index p any non-negative integer.

In cylindrical coordinates, when the direction of propagation is z, the analytical tridimensional expression for these beams then reads:

$$\begin{aligned} LG_{lp}(\rho,\varphi,z) = \sqrt{\frac{p!}{\pi(l+p)!}}\left(\frac{\sqrt{2}}{\omega(z)}\right)^{l+1} \times \\ \rho^l exp\left(-\frac{\rho^2}{\omega^2(z)}\right) L_p^l\left(\frac{2\rho^2}{\omega^2(z)}\right) \times \\ exp\left[-\frac{ik\rho^2 z}{2(z^2+z_0^2)}\right] exp\left[i(2p+l+1)\text{atan}\left(\frac{z}{z_0}\right)\right] exp(il\varphi) \end{aligned} \tag{C.4}$$

where $\omega(z)$ is the beam width, k the wave number, and z_0 the Rayleigh length.

The Laguerre-Gaussian beams have a cylindrical symmetry, and the shape of their beam profile is determined by the two indices p and l: p determines the number of nodes along the radial direction, while l determines the phase distribution of the mode along the azimuthal direction. This phase variation, due to the term $exp(il\varphi)$, results in a helix structure of the wavefront. Consequently, there is a phase singularity at the center of the beam for $l \neq 0$ and, in order to fulfill the wave equation, the intensity is null at that point. Because of this phase singularity, Laguerre-Gaussian beams are also called doughnut beams or optical vortices. Figure C.2 plots intensity and phase profiles of the first twelve Laguerre-Gaussian modes.

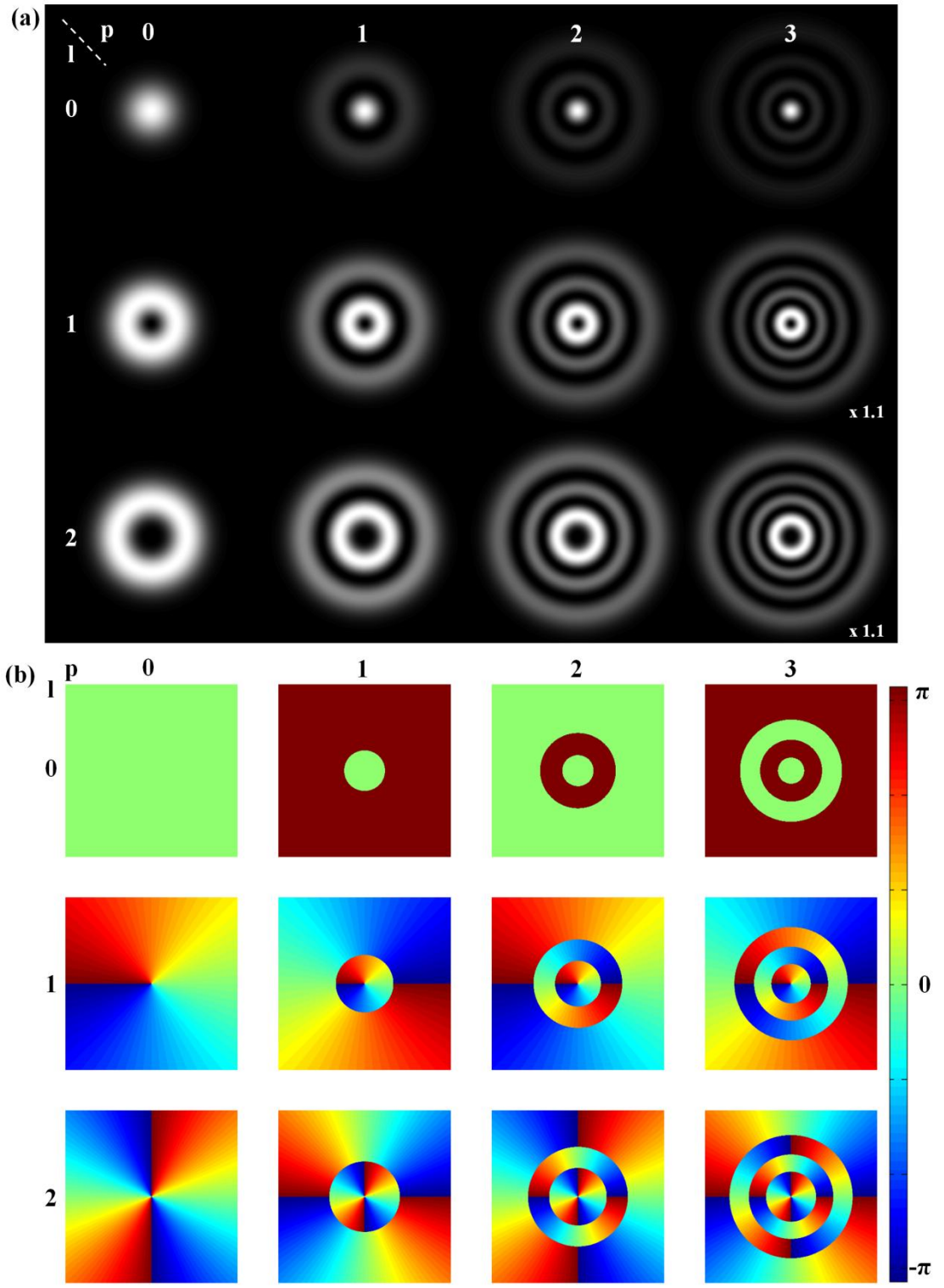

Figure C.1: First twelve Laguerre-Gaussian beams. (a) *Intensity and* (b) *phase profiles of the first twelve Laguerre-Gaussian beams: for Laguerre-Gaussian modes, the indices* l and p *determine the shape of the beam profile:* p *determines the number of nodes along the radial direction, while* l *determines the phase distribution of the mode along the azimuthal direction. The intensities profiles of the* LG_{13} *and* LG_{23} *have been rescaled in size to fully fit into the figure.*

Bibliography

AÇIMOVIÇ, S.S., KREUZER, M.P., GONZALEZ, M.U. & QUIDANT, R. (2009). Plasmon near-field coupling in metal dimmers as a step toward single-molecule sensing. *ACS Nano*, **3**, 1231-1237.

AESCHLIMANN, M., BAUER, M., BAYER, D., BRIXNER, T., GARCÍA DE ABAJO, F.J., PFEIFFER, W., ROHMER, M., SPINDLER, C. & STEEB, F. (2007). Adaptive subwavelength control of nano-optical fields. *Nature*, **446**, 301-304.

AIZPURUA, J., BRYANT, G.W., RICHTER, L.J. & GARCÍA DE ABAJO, F.J. (2005). Optical properties of coupled metallic nanorods for field-enhanced spectroscopy. *Physical Review B*, **71**, 235420.

ALMEIDA, V.R., BARRIOS, C.A., PANEPUCCI, R.R. & LIPSON, M. (2004). All-optical control of light on a silicon chip. *Nature*, **431**, 1081-1084.

ATWATER, H.A. & POLMAN, A. (2010). Plasmonics for improved photovoltaic devices. *Nature Materials*, **9**, 205-213.

BADOLATO, A., HENNESSY, K., ATATÜRE, M., DREISER, J., HU, E., PETROFF, P.M. & IMAMOGLU, A. (2005). Deterministic coupling of single quantum dots to ssingle nanocavity modes. *Science*, **308**, 1158-1161.

BALANIS, C.A. (2005). *Antenna theory: analysis and design*. Wiley, Hoboken, New Jersey.

BAO, Y.J., ZHANG, B., WU, Z., SI, J.W., WANG, M., PENG, R.W., LU, X., LI, Z.F., HAO, X.P. & MING, N.B. (2007). Surface-plasmon-enhanced transmission through metallic film perforated with fractal-featured aperture array. *Applied Physics Letters*, **90**, 251914.

BARNES, W.L., DEREUX, A. & EBBESEN, T.W. (2003). Surface plasmon subwavelength optics. *Nature*, **424**, 824-830.

BERRY, M.V. (1994). *Faster than Fourier, quantum coherence and realuty; in celebration of the 60th birthday of Yakir Aharonov*. Edited by J. S. Anandan and J. L. Safko. World Scientific, Singapore.

BERTHELOT, J., BOUHELIER, A., HUANG, C., MARGUERITAT, J., COLAS DES FRANCS, G., FINOT, E., WEEBER, J.C., DEREUX, A., KOSTCHEEV, S., EL AHRACH, H.I., BAUDRION, A.L., PLAIN, J., BACHELOT, R., ROYER, R. &

WIEDERRECHT, G.P. (2009). Tuning of an optical dimer nanoantenna by electrically controlling its load impedence. *Nano Letters*, **9**, 3914-3921.

BHARADWAJ, P., BOUHELIER, A. & NOVOTNY, L. (2011). Electrical excitation of surface plasmons. *Physical Review Letters*, **106**, 226802.

BHARADWAJ, P., DEUTSCH, B. & NOVOTNY, L. (2009). Optical Antennas. *Advances in Optics and Photonics*, **1**, 438-483.

BORN, M. & WOLF, E. (2002). *Principles of Optics*. Cambridge University Press, Cambridge, England.

BOZHEVOLNYI, S.L., MARKEL, V.A., COELLO, V., KIM, W., & SHALAEV, W.E. (1998). Direct observation of localized dipolar excitations on rough nanostructured surfaces. *Physical Review B*, **58**, 11441.

BRETSCHER, O. (1995). *Linear algebra with applications*. Prentice Hall, New Jersey.

BRIXNER, T., GARCÍA DE ABAJO, F.J., SCHNEIDER, J. & PFEIFFER, W. (2005). Nanoscopic ultrafast space-time-resolved spectroscopy. *Physical Review Letters*, **95**, 093901.

BRIXNER, T., GARCÍA DE ABAJO, F.J., SCHNEIDER, J., SPINDLER, C. & PFEIFFER, W. (2006). Ultrafast adaptive optical near-field control. *Physical Review B*, **73**, 125437.

BRONGERSMA, M.L. & SHALAEV, V.M. (2010). The case of plasmonics. *Science*, **328**, 440-441.

BROKMANN, X., COOLEB, L., HERMIER, J.P. & DAHAN, M. (2005). Emission properties of semiconductor quantum dots close to a dielectric interface. *Chemical Physics*, **318**, 91-98.

CHEN, C., CHU, P., BOBISCH, C.A., MILLS, D.L. & HO, W. (2010). Viewing the interior of a single molecule: vibronically resolved photon imaging at submolecular resolution. *Physical Review Letters*, **105**, 217402.

CHEN, H.T., O`HARA, J.F., AZAD, A.K., TAYLOR, A.J., AVERITT, R.D., SHREKENHAMER, D.B. & PADILLA, W.J. (2006). Experimental demonstration of frequency-agile terahertz metamaterials. *Nature Photonics*, **2**, 295-298.

CHEN, H.T., PADILLA, W.J., ZIDE, J.M.O., GOSSARD, A.C., TAYLOR, A.J. & AVERITT, R.D. (2006). Active terahertz met material devices. *Nature*, **444**, 597-600.

CHOI, H., PILE, D.F., NAM, S., BARTAL, G. & ZHANG, X. (2009). Compressing surface plasmons for nano-scale optical focusing. *Optics Express*, **17**, 7519-7524.

CHU, K.C., CHAO, C.Y., CHEN, Y.F., WU, Y.C. & CHEN, C.C. (2006). Electrically controlled surface plasmon resonance frequency of gold nanorods. *Applied Physics Letters*, **89**, 103107.

CRAIGHEAD, H.G. & NIKLASSON, G.A. (1984). Characterization and optical properties of arrays of small gold particles. *Applied Physics Letters*, **44**, 1134-1136.

CUCHE, A., MOLLET, O., DREZET, A. & HUANT, S. (2010). "Deterministic" quantum plasmonics. *Nano Letters*, **10**, 4566-4570.

CURTO, A.G., VOLPE, G., TAMINIAU, T.H., KREUZER, M.P., QUIDANT, R. & VAN HULST, N.F. (2010). Unidirectional emission of a quantum dot coupled to a nanoantenna. *Science*, **329**, 930-933.

DAL NEGRO, L. & BORISKINA, S. (2011). Deterministic aperiodic nanostructures for photonics and plasmonics applications. *Laser Photonics Review*, 1-41.

DE WAELE, R., FEMIUS KOENDERINK, A. & POLMAN, A. (2007). Tunable nanoscale localization of energy on plasmon particle arrays. *Nano Letters*, **7**, 2004-2008.

DICKEN, M.J., AYDIN, K., PRYCE, I.M., SWEATLOCK, L.A., BOYD, E.M., WALAVALKAR, S., MA, J. & ATWATER, H.A. (2009). Frequency tunable near-infrared metamaterials based on VO_2 phase transition. *Optics Express*, **17**, 18330-18339.

DICKSON, W., WURTZ, G.A., EVANS, P.R., POLLARD, R.J. & ZAYATS, A.V. (2008). Electronically controlled surface plasmon dispersion and optical transmission through metallic hole arrays using liquid crystal. *Nano Letters*, **8**, 281-286.

DURACH, M., RUSINA, A., STOCKMAN, M.I. & NELSON, K. (2007). Toward full spatiotemporal control on the nanoscale. *Nano Letters*, **7**, 3145-3149.

EBBESEN, T.W., LEZEC, H.J., GHAEMI, H.F., THIO, T. & WOLFF, P.A. (1998). Extraordinary optical transmission through sub-wavelength hole arrays. *Nature*, **391**, 667-669.

EVANS, P.R., WURTZ, G.A., HENDREN, W.R., ATKINSON, R., DICKSON, W., ZAYATS, A.V. & POLLARD, R.J. (2007). Electrically switchable nonreciprocal transmission of plasmonic nanorods with liquid crystal. *Applied Physics Letters*, **91**, 043101.

FANG, N., LEE, H., SUN, C. & ZHANG, X. (2005). Sub-diffraction-limited optical imaging with a silver superlens. *Science*, **308**, 534-537.

FALK, A.L., KOPPENS, F.H., YU, C.L., KANG, K., DE LEON SNAPP, N., AKIMOV, A.V., LUKIN, M.D. & PARK, H. (2009). Near-field electrical detection of optical plasmons and single-plasmon sources. *Nature Physics*, **5**, 475-479.

FERNANDEZ-CUESTA, I., NIELSEN, R.B., BOLTASSEVA, A., BORRISÉ, X., PÉREZ-MURANO, F. & KRISTENSEN, A. (2007). V-groove plasmonic waveguides fabricated by nanoimprint lithography. *Journal of Vacuum Science & Technology B*, **25**, 2649-2653.

FEURER, T., VAUGHAN, C. & NELSON, K.A. (1993). Spatiotemporal coherent control of lattice vibrational waves. *Science*, **299**, 374-377.

FUNSTON, A.V., NOVA, C., DAVIS, T.J. & MULVANEY, P. (2009). Plasmon coupling of gold nanorods at short distances and in different geometries. *Nano Letters*, **9**, 1651-1658.

GERSEN, H., GARCÍA-PARAJÓ, M.F., NOVOTNY, L., VEERMAN, J.A., KUIPERS, L. & VAN HULST, N.F. (2000). Influencing the angular emission of a single molecule. *Physical Review Letters*, **85**, 5312.

GHENUCHE, P., CHERUKULAPPURATH, S., TAMINIAU, T.H., VAN HULST, N.F. & QUIDANT, R. (2008). Spectroscopic mode mapping of resonant plasmon nanoantennas. *Physical Review Letters*, **101**, 116805.

GHENUCHE, P., CORMACK, I.G., BADENES, G., LOZA-ALVAREZ, P. & QUIDANT, R. (2007). Cavity resonances in finite plasmonic chains. *Applied Physics Letters*, **90**, 041109.

GJONAJ, B., AULBACH, J., JOHNSON, P.M., MOSK, A.P., KUIPERS, L. & LAGENDIJK, A. (2011). Active spatial control of plasmonic fields. *Nature Photonics*, **5**, 360-363.

GIANNINI, V., FERNÁNDEZ-DOMÍNGUEZ, A.I., HECK, S.C. & MAIER, S.A. (2011). Plasmonic nanoantennas: Fundamentals and their use in controlling radiative properties of nanoemitters. *Chemical Reviews*, **111**, 3888-3912.

GIRARD, C. (2005). Near field in nanostructures. *Reports on Progress in Physics*, **68**, 1883-1933.

GRAELLS, S., ALCUBILLA, R., BADENES, G. & QUIDANT, R. (2007). Growth of plasmonic gold nanostructures by electron beam induced deposition. *Applied Physics Letters*, **91**, 121112.

GRAND, J., ADAM, P.M., GRIMAULT, A.S., VIAL, A., CHAPELLE, M.L., BIJCON, J.L., KOSTCHEEV, S. & ROYER, P. (2006). Optical extinction spectroscopy of oblate, prolate and ellipsoid shaped gold nanoparticles: Experiments and theory. *Plasmonics*, **1**, 135-140.

GRBIC, A. & ELEFTHERIADES, G.V. (2004). Overcoming the diffraction limit with a planar left-handed transmission-line lens. *Physical Review Letters*, **92**, 117403.

HAO, F., SONNEFRAUD, Y., VAN DORPE, P., MAIER, S.A., HALAS, N.J. & NORDLANDER, P. (2008). Symmetry breaking in plasmonic nanocavities: subradiant LSPR sensing and a tunable Fano resonance. *Nano Letters*, **8**, 3983-3988.

HÄRTLING, T., ALAVERDYAN, Y., HILLE, A., WENZEL, M.T., KÄLL, M., & ENG, L.M. (2008). Optically controlled interparticle distance tuning and welding of single gold nanoparticle pairs by photochemical metal deposition. *Optics Express*, **16**, 12362-12371.

HELL, S.W. (2007). Far-field optical nanoscopy. *Science*, **316**, 1153-1158.

HOFMANN, H.F., KOSAKO, T. & KADOYA, Y. (2007). Design parameters for a nano-optical Yagi-uda antenna. *New Journal of Physics*, **9**, 217.

HRELESCU, C., SAUT, T.K., ROGACHT, A.L., JÄCKEL, F., LAURENT, G., DOUILLARD, L. & CHARRA, F. (2011). Selective excitation of individual plasmonic hotspots at the tips of single gold nanostars. *Nano Letters*, **11**, 402-407.

HUANG, J.S., CALLEGARI, V., GEISLER, P., BRÜNING, C., KERN, J., PRANGSMA, J.C., WU, X., FEICHTNER, T., ZIEGLER, J., WEINMANN, P., KAMP, M., FORCHEL, A., BIAGIONI, P., SENNHAUSER, U. & HECHT, B.

(2011). Atomically flat single-crystalline gold nanostructures for plasmonic nanocircuitry. *Nature Communications*, **1**, 150.

HUANG, X., XIAO, S., HUANGFU, J., WANG, Z., RAN, L. & ZHOU, L. (2010). Fractal plasmonic metamaterials for subwavelength imaging. *Optics Express*, **18**, 10377-10387.

HUSNIK, M., KLEIN, M.W., FETH, N., KÖNIG, M., NIEGEMANN, J., BUSCH, K., LINDEN, S. & WEGENER, M. (2008). Absolute extinction cross-section of individual magnetic split-ring resonators. *Nature Photonics*, **2**, 614-617.

JAIN, P.K. & EL-SAYED, M.A. (2008). Surface plasmon coupling and its universal size scaling in metal nanostructures of complex geometry: Elongated particle pairs and nanosphere trimers. *Journal Physical Chemistry C*, **112**, 4954-4960.

JAIN, P.K., HUANG, W. & EL-SAYED, M.A. (2007). On the universal scaling behavior of the distance decay of plasmon coupling in metal nanoparticle pairs: A plasmon ruler equation. *Nano Letters*, **7**, 2080-2088.

JAUFFRED, L., RICHARDSON, A.C. & ODDERSHEDE, L.B. (2008). Three-dimensional optical control of individual quantum dots. *Nano Letters*, **8**, 3376-3380.

JIA, S. & FLEISCHER, J.W. (2010). Nonlinear light propagation in fractal waveguide arrays. *Optics Express*, **18**, 14409-14415.

JIN, R., CAO, Y., MIRKIN, C.A., KELLY, K.L., SCHATZ, G.C. & ZHENG, J.G. (2001). Photoinduced conversion of silver nanospheres to nanoprisms. *Science*, **294**, 1901-1903.

JOHNSON, P.B. & CHRISTY, R.W. (1972). Optical constants of the noble metals. *Physical Review B*, **6**, 4370-4379.

JUAN, M.L., RIGHINI, M. & QUIDANT, R. (2011). Plasmon nano-optical tweezers. *Nature Photonics*, **5**, 349-356.

KALKBRENNER, T., HAKANSON, U., SCHÄDLE, A., BURGER, S., HENKEL, C. & SANDOGHDAR, V. (2005). Optical microscopy via spectral modifications of a nanoantenna. *Physical Review Letters*, **95**, 200801.

KINDLER, J., BANZER, P., QUABIS, S., PESCHEL, U. & LEUCHS, G. (2005). Waveguide properties of single subwavelength holes demonstrated with radially and azimuthally polarized light. *Applied Physics B*, **89**, 517-520.

KNIGHT, M.W. & HALAS, N.J. (2008). Nanoshells to nanoeggs to nanocups: Optical properties of reduced symmetry core-shell nanoparticles beyond the quasistatic limit. *New Journal of Physics*, **10**, 105006.

KOBERLING, F., KOLB, U., PHILIPP, G., POTAPOVA, I., BASCHÉ, T. & MEWS, A. (2003). Fluorescence anisotropy and crystal structure of individual semiconductor nanocrystals. *Journal of Physical Chemistry B*, **107**, 7463-7471.

KOENDERINK, A.F. (2009). Plasmon nanoparticle array waveguides for single photon and single plasmon sources. *Nano Letters*, **9**, 4228-4233.

KOSAKO, T., KADOYA, Y. & HOFMANN, H.F. (2010). Directional control of light by a nano-optical Yagi-Uda antenna. *Nature Photonics*, **4**, 312-315.

KRACHMALNICOFF, V., CASTANI, E., DE WILDE, Y. & CARMINATI, R. (2010). Fluctuations of the local density of states probe localized surface plasmons on disordered metal films. *Physical Review Letters*, **105**, 183901.

KRAMPER, P., AGIO, M., SOUKOULIS, C.M., BIRNER, A., MÜLLER, F., WEHRSPOHN, R.B., GÖSELE, U. & SANDOGHDAR, V. (2004). Highly directional emission from photonic crystal waveguides of subwavelength width. *Physical Review Letters*, **92**, 113903.

KREUZER, M.P., QUIDANT, R., BADANES, G. & MARCO, M.P. (2006). Quantitative detection of doping substances by a localized surface Plasmon sensor. *Biosensors & Bioelectronics*, **21**, 1345-1349.

KREIBIG, U. & VOLLMER, M. (1993). *Optical properties of metal clusters*. Springer Verlag, New York, USA.

KRENN, J.R., SCHIDER, G., RECHBERGER, W., LAMPRECHT, B. & LEITNER, A. (2000). Design of multipolar plasmon excitations in silver nanoparticles. *Applied Physics Letters*, **77**, 3379-3381.

KRETSCHMANN, E. & RAETHER, H. (1968). Radiative decay of non-radiative surface plasmons excited by light. *Zeitschrift für Naturforshung*, **23A**, 2135-2136.

KUBO, A., ONDA, K., PETEK, H., SUN, Z., JUNG, Y.S. & KIM, H.K. (2005). Femtosecond imaging of surface plasmon dynamics in a nanostructured silver film. *Nano Letters*, **5**, 1123-1127.

KÜHN, S., MORI, G., AGIO, M. & SANDOGHDAR, V. (2008). Modification of single molecule fluorescence close to a nanostructure: radiation pattern, spontaneous emission and quenching. *Molecular Physics*, **106**, 893-908.

LEROUX, Y.R., LACROIX, J.C., CHANE-CHING, K.I., FAVE, C., FELIDJ, N., LEVI, G., AUBARD, J., KRENN, J.R. & HOHENAU, A. (2005). Conducting polymer electrochemical switching as an easy means for designing active plasmonic devices. *Journal of the American Chemical Society*, **127**, 16022-12023.

LEUTENEGGER, M., RAO, R., LEITGEB, R.A. & LASSER, T. (2006). Fast focus field calculations. *Optics Express*, **14**, 11277-11291.

LEZEC, H.J., DEGIRON, A., DEVAUX, E., LINKE, R.A., MARTIN-MORENO, L., GARCÍA-VIDAL, F.J. & EBBESEN, T.W. (2002). Beaming light from a subwavelength aperture. *Science*, **297**, 820-822.

LI, J., SALANDRINO, A. & ENGHETA, N. (2007). Shaping light beams in the nanometer scale: a Yagi-Uda nanoantenna in the optical domain. *Physical Review B*, **76**, 245403.

LI, K., STOCKMAN, M.I. & BERGMAN, D.J. (2003). Self-similar chain of metal nanospheres as an efficient nanolens. *Physical Review Letters*, **91**, 227402.

LI, X. & STOCKMAN, M.I. (2008). Highly efficient spatiotemporal coherent control in nanoplasmonics on a nanometer-femtosecond scale by time reversal. *Physical Review B*, **77**, 195109.

LIEB, M.A., ZAVISLAV, J.M. & NOVOTNY, L. (2004). Single-molecule orientations determined by direct emission pattern imaging. *Journal of the Optical Society of America B*, **21**, 1210-1215.

LINK, S., MOHAMED, M.B. & EL-SAYED, M.A. (1999). Simulation of the optical absorption spectra of golf nanorods as a function of their aspect ratio and the effect of the medium dielectric constant. *Journal of Physical Chemistry B*, **103**, 3073-3077.

LIU, Z., THORESON, M.D., KILDISHEV, A.F. & SHALAEV, V.M. (2009). Translation of nanoantenna hot spots by a metal-dielectric composite superlens. *Applied Physics Letters*, **95**, 033114.

LÓPEZ-TEJEIRA, F., RODRIGO, S.G., MARTÍN-MORENO, L., GARCÍA-VIDAL, F.J., DEVAUX, E., EBBESEN, T.W., KRENN, J.R., RADKO, I.P., BOZHEVOLNYI, S.I., GONZÁLEZ, M.U., WEEBER, J.C. & DEREUX, A. (2007).

Efficient unidirectional nanoslit couplers for surface plasmons. *Nature Physics*, **3**, 324-328.

LOVE, J.C., ESTROFF, L.A., KRIEBEL, J.K., NUZZO, R.G. & WHITESIDES, J.M. (2005). Self-assembled monolayers of thiolates on metals as a form of nanotechnology. *Chemical Review*, **105**, 1103-1169.

MAIER, S.A. (2007). *Plasmonics: Fundamentals and applications*. Springer Verlag, New York, USA.

MANDELBROT, B.B. (1982). *The fractal geometry of nature*. W. H. Freeman, San Francisco, USA.

MARTIN, O.J., GIRARD, C. & DEREUX, A., (1995). Generalized field propagator for electromagnetic scattering and light confinement. *Physical Review Letters*, **74**, 526-529.

MOERNER, W.E. & KADOR, L. (1989). Optical detection and spectroscopy of single molecules in a solid. *Physical Review Letters*, **62**, 2535-2538.

MERLEIN, J., KAHL, M., ZUSCHLAG, A., SELL, A., HALM, A., BONEBERG, J., LEIDERER, P., LEITENSTORFER, A. & BRATCHITSCH, R. (2008). Nanomechanical control of an optical antenna. *Nature Photonics*, **2**, 230-233.

MEIYAMARU, F., SAITO, Y., TAKEDA, M.W., HOU, B., LIU, L., WEN, W. & SHENG, P. (2008). Teraherzt electric response of fractal metamaterials structures. *Physical Review B*, **77**, 045124.

MOLINA-TERRIZA, G. (2008). Determination of the angular momentum of a paraxial beam. *Physical Review A*, **78**, 053819.

MÜHLSCHLEGEL, P., EISLER, H.J., MARTIN, O.J.F., HECHT, B. & POHL, D.W. (2005). Resonant optical antennas. *Science*, **308**, 1607-1609.

MÜLLER, J., SÖNNICHSEN, C., VON POSCHINGER, H., VON PLESSEN, G., KLAR, T.A. & FELDMANN, J. (2002). Electrically controlled light scattering with single metal nanoparticles. *Applied Physics Letters*, **81**, 171.

NEHL, L.C., LIAO, H. & HAFNER, J.H. (2006). Optical properties of star-shaped gold nanoparticles. *Nano Letters*, **6**, 683-688.

NODA, S., TOMODA, K., YAMAMOTO, N. & CHUTINAN, A. (2000). Full three-dimensional photonic bandgap crystals at near-infrared wavelengths. *Science*, **289**, 604-606.

NOGUEZ, C. (2007). Surface plasmons on metal nanoparticles: The influence of shape and physical environment. *Journal of Physical Chemistry C*, **111**, 3806-3819.

NORLANDER, P., OUBRE, C., PRODAN, E., LI, K. & STOCKMAN, M.I. (2004). Plasmon hybridization in nanoparticle dimers. *Nano Letters*, **4**, 899-903.

NOVOTNY, L. (2007). Effective wavelength scaling for optical antennas. *Physical Review Letters*, **98**, 266802.

NOVOTNY, L. & HAFNER, C. (1994). Light propagation in a cylindrical waveguide with a complex, metallic, dielectric function. *Physical Review E*, **50**, 4094-4106.

NOVOTNY, L. & HECHT, B. (2006). *Principle of nano-optics*. Cambridge University Press, Cambridge, England.

NOVOTNY, L. & VAN HULST, N. (2011). Antennas for light. *Nature Photonics*, **5**, 83-90.

OKAMOTO, T. (2001). Near-field optics and surface plasmon polaritons. *Topics in Applied Physics*, **81**, 97-122.

OLK, P., RENGER, J., WENZEL, M.T. & ENG, L.M. (2008). Distance dependent spectral tuning of two coupled metal nanoparticles. *Nano Letters*, **8**, 1174-1178.

OTTO, A. (1968). Excitation of nonradiative surface plasma waves in silver by the method of frustrated total reflection. *Zeitschrift für Physik*, **216**, 398.

PALIK, E.D. (1985). *Handbook of optical constants of solids*. Academic Press, Orlando, Florida.

PARK, S.Y. & STROUD, D. (2004). Splitting of surface plasmon frequencies of metal particles in a nematic liquid crystal. *Applied Physics Letters*, **85**, 2920.

PAULUS, M., GAY- BALMAZ, P. & MARTIN, O.J.F. (2000). Accurate and efficient computation of the Green's tensor for stratified media. *Physical Review E*, **62**, 5797-5807.

PEITGEN, H.O., JÜRGENS, H. & SAUPE, D. (1992). *Chaos and fractals: New frontiers of science*. Springer Verlag, Berlin, New York.

PENDRY, J.B. (2000). Negative refraction makes a perfect lens. *Physical Review Letters*, **85**, 3966-3969.

PELTON, M., SANTORI, C., VUCKOVIC, J., ZHANG, B., SOLOMON, G.S., PLANT, J. & YAMAMOTO, Y. (2002). Efficient source of single photons: a single quantum dot in a micropost microcavity. *Physical Review Letters*, **89**, 233602.

PÉREZ-GONZÁLEZ, O., ZABALA, N., & AIZPURUA, J. (2011). Optical characterization of charge transfer and bonding dimer plasmons in linked interparticle gaps. *New Journal of Physics*, **13**, 083013.

PILE, D.F.P. & GRAMOTNEV, D.K. (2006). Adiabatic and nonadiabatic nanofocusing of plasmons for nano-scale optical focusing. *Applied Physical Letters*, **89**, 041111.

PRODAN, E., RADLOFF, C., HALAS, N.J. & NORLANDER, P. (2003). A hybridization model for the plasmon response of complex nanostructures. *Science*, **302**, 419-422.

PRYCE, I.M., AYDIN, K., KELAITA, Y.A., BRIGGS, R.M. & ATWATER, H.A. (2010). Highly strained complaint optical metamaterials with large frequency tunability. *Nano Letters*, **10**, 4222-4227.

RAETHER, H. (1988). *Surface plasmons on smooth and rough surfaces and on gratings*. Springer Verlag, Berlin, Germany.

RAZAVI, B. (2008). *Fundamentals of microelectronics*. Wiley, Hoboken, New Jersey.

RENGER, J., GRAFSTRÖM, S. & ENG, L.M. (2007). Direct excitation of surface plasmon polaritons in nanopatterned metal surfaces and thin films. *Physical Review B*, **76**, 045431.

RENGER, J., QUIDANT, R., VAN HULST, N., PALOMBA, S. & NOVOTNY, L. (2009). Free-space excitation of propagating surface plasmon polaritons by nonlinear four-wave mixing. *Physical Review Letters*, **103**, 266802.

RIEDEL, D., DELATTRE, R., BORISOV, A.G. & TEPERIK, T.V. (2010). A scanning tunneling microscope as a tunable nanoantenna for atomic scale control of optical-field enhancement. *Nano Letters*, **10**, 3857-3862.

RIGHINI, M., VOLPE, G., GIRARD, C., PETROV, D. & QUIDANT, R. (2008). Surface plasmon optical tweezers: tunable optical manipulation in the femtonewton range. *Physical Review Letters*, **100**, 186804.

RIGHINI, M., ZELENINA, A.S., GIRARD, C. & QUIDANT, R. (2007). Parallel and selective trapping in a patterned plasmonic landscape. *Nature Physics*, **3**, 477-480.

RINGLER, M., SCHWEMER, A., WUNDERLICH, M., NICHTL, A., KÜRZINGER, K., KLAR, T.A. & FELDMANN, J. (2008). Shaping emission spectra of fluorescent molecules with single plasmonic nanoresonators. *Physical Review Letters*, **100**, 203002.

ROPP, C., CUMMINS, Z., PROBST, R., QIN, S., FOURKAS, J.T., SHAPIRO, B. & WAKS, E. (2010). Positioning and immobilization of individual quantum dots with nanoscale precision. *Nano Letters*, **10**, 4673-4679.

SÁMSON, Z.L., MACDONALD, K.F., DE ANGELIS, F., GHOLIPOUR, B., KNIGHT, K., HUANG, C.C., DI FABRIZIO, E., HEWAK, D.W. & ZHELUDEV, N.I. (2010). Metamaterial electro-optic switch of nanoscale thickness. *Applied Physics Letters*, **96**, 143104.

SCARANI, V. & THEW, R. (2006). *Quantum physics: a first encounter: interference, entanglement, and reality*. Oxford University Press, Oxford, England.

SCHNELL, M., ALONSO- GONZÁLEZ, P., ARZUBIAGA, L., CASANOVA, F., HUESO, L.E., CHUVILIN, A. & HILLENBRAND, R. (2011). Nanofocusing of mid-infrared energy with tapered transmission lines. *Nature Photonics*, **5**, 283-287.

SCHUCK, P.J., FROMM, D.P., SUNDARAMURTHY, A., KINO, G.S. & MOERNER, W.E. (2005). Improving the mismatch between light and nanoscale objects with gold bowtie nanoantennas. *Physical Review Letters*, **94**, 017402.

SHALAEV, V.M. & STOCKMAN, M.I. (1988). Fractals: optical susceptibility and giant Raman scattering. *Zeitschrift für Physik D*, **10**, 71-79.

SHALAEV, V.M. (2002). *Optical properties of nanostructured random media*. Springer, New York, USA.

SHEGAI, T., LI, Z., DADOSH, T., ZHANG, Z., XU, H. & HARAN, G. (2008). Managing light polarization via plasmon-molecule interactions within asymmetric metal nanoparticle trimer. *Proceedings of the National Academy of Science*, **105**, 16448-16453.

SHULLER, J.A., BARNARD, E.S., CAI, W., JUN, Y.C., WHITE, J.S. & BRONGERSMA, M.L. (2010). Plasmonics for extreme light concentration and manipulation. *Nature Materials*, **9**, 193-204.

SLAUGHTER, L.S., WU, Y., WILLINGHAM, B.A., NORLANDER, P. & LINK, S. (2010). Effects of symmetry breaking and conductive contact on the plasmon coupling in gold nanorod dimers. *ACS Nano*, **4**, 4657-4666.

SIEGMAN, A.E. (1986). *Lasers*. University Science Books, Mill Valley, California.

SIERPINSKI, W. (1916). Sur une cantorienne qui contient une image buinivoque et continue de toute courbe donnée. *Comptes Rendus Hebdomadaires des Seances de l'Academie des Sciences*, **162**, 629-632.

STOCKMAN, M.I. (2004). Nanofocusing of optical energy in tapered plasmonic waveguides. *Physical Review Letters*, **93**, 137404.

STOCKMAN, M.I., BERGMAN, D.J. & KOBAYASHI, T. (2004). Coherent control of nanoscale localization of ultrafast optical excitation in nanosystems. *Physical Review B*, **69**, 054202.

STOCKMAN, M.I., FALEEV, S.V. & BERGMAN, D.J. (2002). Coherent control of femtosecond energy localization in nanosystems. *Physical Review Letters*, **88**, 067402.

SU, K.H., ZHANG, X., MOCK, J.J., SMITH, D.R. & SCHULTZ, S. (2003). Interparticle coupling effects on plasmon resonances of nanogold particles. *Nano Letters*, **3**, 1087-1090.

SUN, Y. & XIA, Y. (2002). Shape-controlled synthesis of gold and silver nanoparticles. *Science*, **298**, 2176-2179.

TAKLA, N. & SHEN L.C. (1977). Bandwidth of a Yagi array with optimum directivity. *IEEE Transaction on Antennas and Propagation*, **25**, 913-914.

TAMINIAU, T.H., STEFANI, F.D., SEGERINK, F.B. & VAN HULST, N.F (2008). Optical antennas direct single-molecule emission. *Nature Photonics*, **2**, 234-237.

TAMINIAU, T.H., STEFANI, F.D. & VAN HULST, N.F (2008). Enhanced directional excitation and emission of single emitters by a nano-optical Yagi-Uda antenna. *Optics Express*, **16**, 16858-16866.

TAO, H., STRIKWERDA, A.C., FAN, K., PADILLA, W.J., ZHANG, X. & AVERITT, R.D. (2009). Reconfigurable terahertz metamamterials. *Physical Review Letters*, **103**, 147401.

TSAI, D.P., KOVACS, J., WANG, Z., MOSKOVITS, M., SHALAEV, V.M., SUH, J.S. & BOTET, R. (1994). Photon scanning tunneling microscopy images of optical excitations of fractal metal colloid clusters. *Physical Review Letters*, **72**, 4149.

VEDANTAM, S., LEE, H., TANG, J., CONWAY, J., STAFFARONI, M. & YABLONOVITCH, E. (2009). A plasmonic dimple lens for nanoscale focusing of light. *Nano Letters*, **9**, 3447-3452.

VIGOUREUX, J.M. & COURJON, D. (1992). Detection of nonradiative fields in light of the Heisenberg uncertainty principle and the Rayleigh criterion. *Applied Optics*, **31**, 3170-3177.

VOLPE, G., CHERUKULAPPURATH, S., JUANOLA-PARRAMON, R., MOLINA-TERRIZA, G. & QUIDANT, R. (2009). Controlling the optical near field of nanoantennas with spatial phase-shaped beams. *Nano Letters*, **9**, 3608-3611.

VOLPE, G., MOLINA-TERRIZA, G. & QUIDANT, R. (2010). Deterministic subwavelength control of light confinemt in nanostructures. *Physical Review Letters*, **105**, 216802.

VOLPE, G., VOLPE, G. & QUIDANT, R. (2011). Fractal plasmonics: subdiffraction focusing and broadband spectral response by a Sierpinski nanocarpet. *Optics Express*, **19**, 3612-3618.

VOLPE, G., QUIDANT, R., BADENES, G. & PETROV, D. (2006). Surface plasmon radiation forces. *Physical Review Letters*, **96**, 238101.

WEFERS, M.M. & NELSON, K.A. (1993). Programmable phase and amplitude femtosecond pulse shaping. *Optics Letters*, **18**, 2032-2034.

WEN, W., ZHOU, L., LI, J., GE, W., CHAN, C.T. & SHENG, P. (2003). Subwavelength photonic band gaps from planar fractals. *Physical Review Letters*, **82**, 223901.

WERNER, D.H. & GANGULY, S. (2003). An overview of fractal antenna engineering research. *IEEE Antenna and Propagation Magazine*, **45**, 38-57.

YAGHJIAN, A.D. (1980). Electric dyadic Green's functions in the source region. *Proceedings of the IEEE*, **68**, 248-263.

YAGI, H. (1928). Beam transmission of ultra short waves. *Proceedings of the IRE*, **16**, 715-740.

YANO, T., VERMA, P., SAITO, Y., ICHIMURA, T. & KAWATA, S. (2009). Pressure-assisted tip-enhanced Raman imaging at a resolution of a few nanometers. *Nature Photonics*, **3**, 473-477.

YU, N., FAN, J., WANG, Q.J., PFLÜGL, C., DIEHL, L., EDAMURA, T., YAMANISHI, M., KAN, H. & CAPASSO, F. (2008). Small-divergence semicnonductor lasers by plasmonic collimation. *Nature Photonics*, **2**, 564-570.

YU, N., GENEVET, P., KATS, M.A., AIETA, F., TETIENNE, J., CAPASSO, F. & GABURRO, Z. (2011). Light propagation with phase discontinuities: Generalized laws of reflection and refraction. *Science*, **334**, 333-337.

XIAO, S., CHETTIAR, U.K., KILDISHEV, A.V., DRACHEV, V., KHOO, I.V. & SHALAEV, V.M. (2009). Tunable magnetic response of metamaterials. *Applied Physics Letters*, **95**, 033115.

ZHENG, Y.B., YANG, Y.W., JENSEN, L., FANG, L., JULURI, B.K., FLOOD, A.H., WEISS, P.S., STODDART, J.F. & HUANG, T.J. (2009). Active molecular plasmonics: Controlling plasmon resonances with molecular switches. *Nano Letters*, **9**, 819-825.

ZHOU, L., WEN, W., CHAN, C.T. & SHENG, P. (2002). Reflectivity of planar metallic fractal patterns. *Applied Physics Letters*, **89**, 1012-1014.

ZIJLSTRA, P., CHON, J.W.M. & GU, M. (2009). Five-dimensional optical recording by surface plasmons in gold nanorods. *Nature*, **459**, 410-413.